Linking partial and quasi dynamical symmetries in rotational nuclei and shell evolution in ^{96}Zr

Der Zusammenhang partieller und quasi-dynamischer Symmetrien in Rotorkernen und Schalenentwicklung in ^{96}Zr

Zur Erlangung des Grades eines Doktors der Naturwissenschaften (Dr. rer. nat.)
genehmigte Dissertation von MASt. Christoph Kremer MBA aus Fulda
Tag der Einreichung: 15.12.2015, Tag der Prüfung: 27.01.2016
February 2016 — Darmstadt — D 17

1. Gutachten: Prof. Dr. Dr. h.c. Norbert Pietralla
2. Gutachten: Prof. Dr. Peter von Neumann-Cosel

TECHNISCHE UNIVERSITÄT DARMSTADT

Fachbereich Physik
AG Norbert Pietralla

Gefördert durch die DFG im Rahmen des SFB 634

Linking partial and quasi dynamical symmetries in rotational nuclei and shell evolution in ^{96}Zr
Der Zusammenhang partieller und quasi-dynamischer Symmetrien in Rotorkernen und Schalenentwicklung in ^{96}Zr

Genehmigte Dissertation von MASt. Christoph Kremer MBA aus Fulda

1. Gutachten: Prof. Dr. Dr. h.c. Norbert Pietralla
2. Gutachten: Prof. Dr. Peter von Neumann-Cosel

Tag der Einreichung: 15.12.2015
Tag der Prüfung: 27.01.2016

Darmstadt — D 17

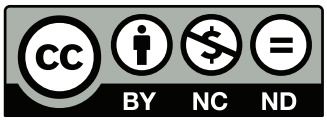

Meiner Mutter
in Liebe und Dankbarkeit gewidmet.

"Be at war with your vices, at peace with your neighbors, and let every new year find you a better man."

- Benjamin Franklin

Abstract

The first part of this thesis revolves around symmetries in the sd-IBA-1. A region of approximate $O(6)$ symmetry for the ground-state band, a partial dynamical symmetry (PDS) of type III, in the parameter space of the extended consistent-Q formalism is identified through quantum number fluctuations. The simultaneous occurrence of a $SU(3)$ quasi dynamical symmetry for nuclei in the region of $O(6)$ PDS is explained via the $\beta = 1$, $\gamma = 0$ intrinsic state underlying the ground-state band. The previously unrelated concepts of PDS and QDS are connected for the first time and many nuclei in the rare earth region that approximately satisfy both symmetry requirements are identified. Ground-state to ground-state (p, t) transfer reactions are presented as an experimental signature to identify pairs of nuclei that both exhibit $O(6)$ PDS.

In the second part of this thesis inelastic electron scattering off ^{96}Zr is studied. The experiment was performed at the high resolution Lintott spectrometer at the S-DALINAC and covered a momentum-transfer range of $0.28 - 0.59$ fm^{-1}. Through a relative analysis using Plane Wave Born Approximation (PWBA) the $B(\mathrm{E2}; 2_2^+ \rightarrow 0_1^+)$ value is extracted without incurring the additional model dependence of a Distorted Wave Born Approximation (DWBA). By combining this result with known multipole mixing ratios and branching ratios all decay strengths of the 2_2^+ state are determined. A mixing calculation establishes very weak mixing ($V_{\mathrm{mix}} = 76$ keV) between states of the ground-state band and those of the band build on top of the 0_2^+ state which includes the 2_2^+ state. The occurrence of these two isolated bands is interpreted within the shell model in terms of type II shell evolution.

Zusammenfassung

Der erste Teil dieser Arbeit beschäftigt sich mit Symmetrien im sd-IBA-1. Im Parameterraum des ECQF wird, mit Hilfe von Quantenzahlfluktuationen, ein Bereich näherungsweiser $O(6)$ Symmetrie für die Grundzustandsbande identifiziert. Dabei handelt es sich um eine PDS vom Typ III. Das gleichzeitige Auftreten einer $SU(3)$ QDS im Bereich der $O(6)$ PDS wird durch den intrinsischen Zustand mit $\beta = 1$ und $\gamma = 0$ erklärt, von welchem die Grundzustandsbande in diesem Parameterbereich näherungsweise projiziert wird. Auf diese Weise werden erstmals die zuvor unabhängigen Konzepte der PDS und QDS miteinander verknüpft. Es werden Kerne im Bereich der seltenen Erden identifiziert, die beide Symmetrien näherungsweise erfüllen. Mit dem Wirkungsquerschnitt für den Übergang vom Grundzustand zum Grundzustand in (p,t) Transferreaktionen wird eine experimentelle Signatur präsentiert, welche es erlaubt Paare von Atomkernen mit $O(6)$ PDS zu identifizieren.

Der zweite Teil dieser Arbeit befasst sich mit inelastischer Elektronenstreuung am Kern ^{96}Zr. Der Elektronenstrahl wurde vom S-DALINAC erzeugt und das Experiment wurde am hochauflösenden Lintott Spektrometer durchgeführt. Dabei wurden Impulsüberträge im Bereich von $0.28-0.59$ fm^{-1} abgedeckt. Mit Hilfe einer relativen PWBA Analyse konnte der $B(\mathrm{E2}; 2_2^+ \rightarrow 0_1^+)$ Wert extrahiert werden. Diese Methode zeichnet sich gegenüber der DWBA Analyse besonders durch eine reduzierte Modellabhängigkeit aus. Unter Berücksichtigung der bekannten Multipolmischungs- und Verzweigungsverhältnisse konnten die übrigen Zerfallsstärken des 2_2^+ Zustands bestimmt werden. Durch eine Mischungsrechnung wird gezeigt, dass die Grundzustandsbande nur sehr schwach mit der angeregten Bande des 0_2^+ Zustands, welche auch den 2_2^+ Zustand enthält, mischt ($V_{\mathrm{mix}} = 76$ keV). Das Auftreten dieser beiden isolierten Banden wird im Rahmen des Schalenmodells durch eine type II shell evolution interpretiert.

Contents

Introduction

"'*We have simply arrived too late in the history of the universe to see this primordial simplicity easily ... But although the symmetries are hidden from us, we can sense that they are latent in nature, governing everything about us.*"' - Steven Weinberg

Physics has always been concerned with the behavior of nature and more generally the world around us. In their search for knowledge physicists have learned to appreciate and exploit the presence of symmetries. Symmetry considerations were first explicitly used in crystallography [1] and have since considerably contributed to our understanding of nature. Symmetries were implicitly always present in the laws of physics, but were treated as a byproduct of these laws. It was not until the mathematical groundwork had been done [2–4] in the late nineteenth century that symmetries took center stage themselves. Soon thereafter, Noether proofed in her groundbreaking theorem [5] that if a system is invariant under a set of symmetry transformations there exist corresponding conserved quantities. Many of physics most basic principles could now be understood as consequences of the underlying symmetry, e.g. the conservation of angular momentum could be explained by rotational invariance.

At about the same time important experimental discoveries lead to a paradigm shift. For most of human history matter was thought to consist of indivisible small spheres, the so called atoms. The discovery of the first subatomic particle, the electron, in 1897 by Thomson [6] and the subsequent discovery of the atomic nucleus by Rutherford, Geiger, and Marsden [7] in 1911 opened up a wholly new world to explore. The atomic nucleus contains all the positive charge and almost all of the mass of the atom while occupying just a tiny fraction of its volume (cf. Fig. 0.1). The positively charged constituents of the nucleus, carrying one unit of elementary charge [8, 9], are called protons. Additionally, the existence of an electrically neutral particle inside the nucleus was postulated by Rutherford and the neutron was discovered by Chadwick in 1932 [10]. Despite the repulsive electromagnetic force between the positively charged protons atomic nuclei are not torn apart. A previously unknown force keeps the nucleons together. This force is named nuclear force and it is the aim of nuclear physics to describe it and the resulting phenomena that can be observed in atomic nuclei.

Starting in the 1940s many new particles, interacting similarly to nucleons, were discovered by studying cosmic rays (see, e.g., Lattes et al. [11]) and later by using particle accelerators (see, e.g., Alvarez et al. [12]). Symmetry played an important role in unifying these particles and their interactions in a single theory. Consider, for example, the third component of isospin I_3 and hypercharge $Y = S+B$, which is the sum of strangeness S and baryon number B, for the baryons. If the baryons are plotted in the I_3-Y plane the resulting plot (Fig. 0.2(a)) looks like a $(1,1)$ representation of $SU(3)$ [13]. This led Gell-Mann to predict the existence of underlying particles [14, 15], called quarks, which should behave as a $(1,0)$ representation of $SU(3)$ (see Fig. 0.2(b)). These underlying particles are bound together by the strong force, which acts on all particles with color charge and is mediated by gluons. The behavior of the strong force is described by the theory of quantum chromodynamics (QCD). Quarks and gluons only exist in hadrons, which are colorless bound systems. Recognizing the underlying $SU(3)$ symmetry allowed the construction of relations between the masses of hadrons within a multiplet via the Gell-Mann-Okubo formula [17–19]. This led to the prediction of the Ω^- baryon, which belongs

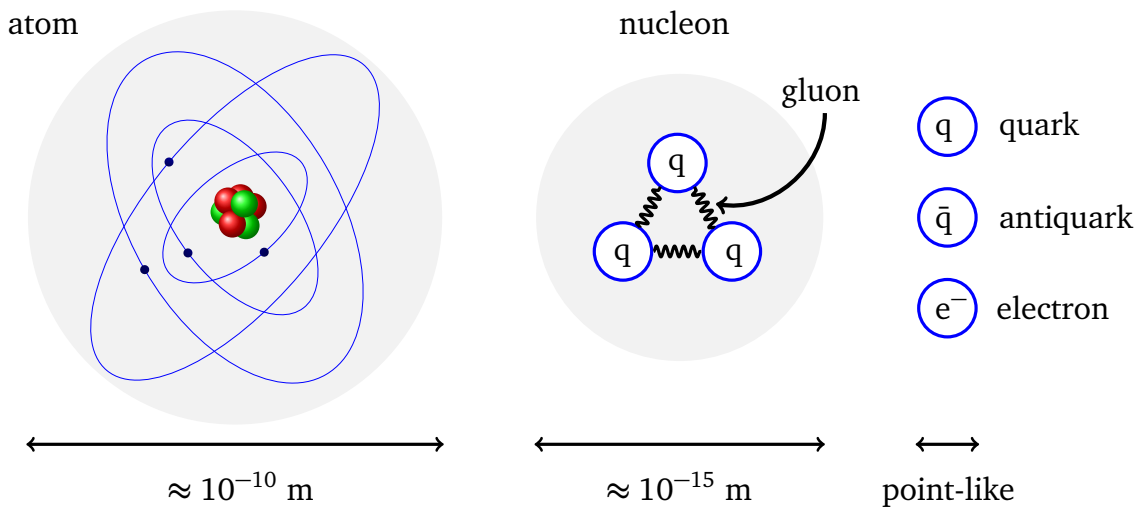

Figure 0.1.: Schematic sketch of an atom, a nucleon (only residual quarks shown), and some elementary particles. Note the difference in relative sizes. An estimate for radii of atomic nuclei is $R = 1.2\ \text{fm} \cdot A^{1/3}$ where A is the number of nucleons.

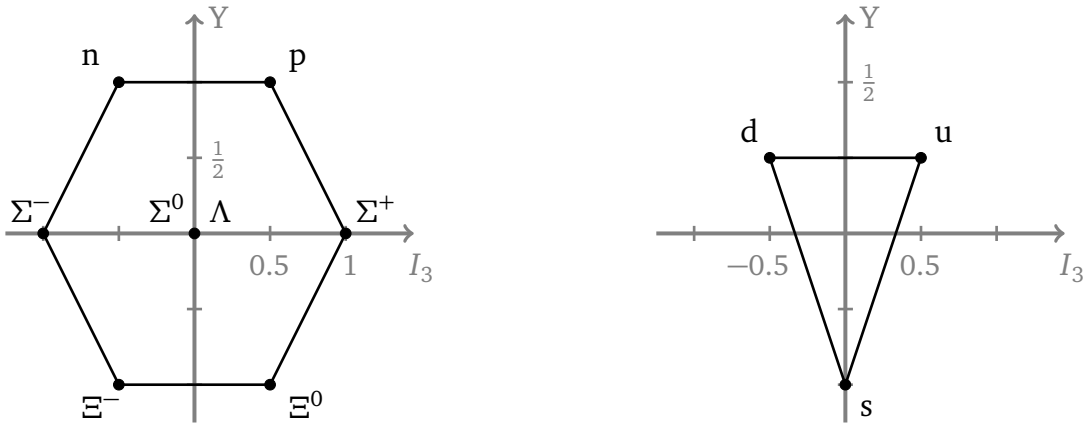

(a) Baryon octet containing neutrons (n) and protons (p) as an 8-dimensional representation of $SU(3)$.

(b) Down (d), up (u), and strange (s) quarks as a 3-dimensional representation of $SU(3)$.

Figure 0.2.: Relation of the strong interaction, as described by QCD, to the symmetry group $SU(3)$. Quarks are assumed to be elementary particles, whereas baryons are built of three quarks (qqq). Quantum numbers of the particles are taken from Olive [16].

to a baryon decuplet, and its mass and decay properties. The experimental confirmation of these predictions [20] strongly support the validity of $SU(3)$ as an approximate symmetry of the strong interaction. Later the idea of smaller constituent particles inside the nucleons was experimentally verified in inelastic electron scattering off protons [21, 22]. Thus, an additional layer of underlying structure has been established. The known constituents of the atom and the corresponding scales are summarized in Fig. 0.1.

Today the nuclear force is understood to be a residual color force arising from the underlying strong interaction of quarks and gluons similar to the way the van der Waals force in molecules arises from the underlying electromagnetic interaction. It can be constructed starting from QCD and its symmetries [23]. Unfortunately, the coupling constant of QCD is of order unity in the low-energy regime of nuclear physics, which hinders the applicability of perturbative approaches. However, nucleon-nucleon potentials can be extracted from QCD by the use of lattice QCD [24] or chiral effective field theories (χEFT) [25]. These methods are also capable of providing an error bar for their predictions. Alternatively, it is possible to construct phenomenological potentials from nucleon-nucleon scattering data [26–28] and incorporate the desired symmetries through a restriction of allowed terms. Once a nuclear potential has been constructed it can be used to tackle the many-body problem posed by atomic nuclei. For small numbers of nucleons ($A \leq 14$) this can be done without further approximation (ab-initio). Frequently used ab-initio methods include quantum Monte Carlo approaches [29] and the no core shell model [30]. For heavier nuclei the many-body problem can only be solved approximately. The methods of choice include the importance-truncated no core shell model [31], coupled cluster methods [32], and random-phase approximation schemes. In order to solve the many-body problem these methods truncate the original Hilbert space to a suitable, usually low-momentum, subspace. This restriction is critical, because the nucleon-nucleon potential induces strong mixing between high and low-momentum modes. However, it is possible to transform the potential, e.g. using the similarity renormalization group method [33, 34], such that these modes decouple and a restriction of the Hilbert space is possible.

A different way to describe nuclei are fully and partly phenomenological approaches, like the Quasiparticle Phonon Model (QPM) [35], the geometrical model of Bohr and Mottelson [36], or the algebraic Interacting Boson Model (IBM) [37]. These models are tailor-made to describe specific nuclear structure phenomena and are only applicable in their specific domain. For example the IBM in its basic form, which will be used extensively in this thesis, is built to reproduce the low energy collective behavior of even-even nuclei. Low-lying nuclear excitations are described as a totally symmetric $(N, 0, 0, 0, 0, 0)$ representation of an $U(6)$ group [38] where N denotes the number of valence bosons. Microscopically, these bosons can be interpreted as coupled pairs of valence nucleons or holes, which is a configuration energetically favored by the pairing interaction. This ansatz makes use of the full mathematical apparatus of group theory and produces analytical predictions for some special dynamical symmetry (DS) limits. While the IBM is an extremely successful tool for the description of some nuclei, e.g. in the rare-earth region (see, e.g., Fig. 2.2), it is not well-suited to describe non-collective phenomena.

All theoretical predictions need to be verified or falsified by comparison to experimental data. Currently, one of the most active fields of experimental nuclear structure physics are Radioactive Ion Beams (RIBs). RIBs enable the study of atomic nuclei at extreme conditions far away from stability and to probe the nuclear force under a different set of circumstances ($N/Z \not\approx 1$). There is a multitude of RIBs facilities currently in use (e.g. GSI, GANIL, REX-ISOLDE, RIKEN, ...) and more are in the process of being build (e.g. FAIR, HIE-ISOLDE, ...) [39]. However, the experimental study of stable and long-lived nuclei is still one of the cornerstones of nuclear structure physics. New experimental techniques, like relative self-absorption [40], and new detector developments allow experiments on these nuclei with ever increasing precision. As an example, the advent of LaBr detectors recently allowed the first observation of the competitive $(\gamma\gamma)$-decay in the long-lived nucleus ^{137}Ba [41]. With the increasing precision of theoretical predictions and

the advent of errors estimates for these predictions it becomes extremely important to perform high-precision experiments to test these theoretical predictions.

This thesis aims to improve the understanding of the nuclear force and the structures it produces in nuclei in two different ways. The first part of this thesis focusses on the concept of symmetries and the emergence of regularity and simplicity in the complex many-body systems of atomic nuclei. It is studied if and how symmetric behavior of atomic nuclei persists away from special, fully-symmetric Hamiltonians and how different approximate symmetries are interconnected. The ideal testing ground for this is the IBM, which is built purely on symmetry considerations, and will be used for this study. The outline of the first part of this thesis is as follows. First (Chap. 1), the search for approximate symmetries within the IBM is briefly motivated. Then, the Interacting Boson Model is introduced in Chap. 2 and the necessary theoretical formalism for the following chapters is described. Chap. 3 starts by discussing possible measures for the goodness of the realization of a given symmetry in a given state of a quantum system. One of these measures, fluctuations of the $O(6)$ quantum number σ, is then used to investigate the goodness of the $O(6)$ symmetry through large parts of the IBM parameter space. The results of this investigation are then interpreted theoretically and real nuclei showcasing the discussed features are identified. A connection to experiment, in terms of (p,t) ground state to ground state transition intensities, is discussed. Finally, Chap. 4 summarizes the obtained results and discusses several directions in which the research can be extended.

The second part of this thesis investigates the nucleus ^{96}Zr, which has proven to be particular challenging for nuclear structure models (see, e.g., Refs. [42, 43]) due to the combination of strong octupole collectivity and a double subshell closure. An electron scattering experiment at low-momentum transfer was conducted with the aim of observing the excitation from the ground-state to the 2_2^+ state. This measurement allows the determination of decay and excitation strengths of this state, which were previously not known with sufficient precision. The new observables allow a novel interpretation of the low-lying nuclear structure of ^{96}Zr in terms of type II shell evolution [44], which is discussed within the shell model. The outline of the second part of the thesis is as follows. Chap. 5 will briefly motivate why the study of ^{96}Zr is important. Then, the theoretical background necessary for the interpretation of the experimental results is discussed in Chap. 6 and the theoretical background of electron scattering follows in Chap. 7. The experiment and the necessary setup, consisting of the electron accelerator and the magnetic spectrometer, are described in Chap. 8. The collected experimental data is also included in this chapter. The analysis of this data, especially the extraction of the $B(\mathrm{E2})$ value, is presented together with the obtained results (Chap. 9). The implications of the new experimental data for the interpretation of the nuclear structure of ^{96}Zr are discussed in Chap. 10. Finally, in Chap. 11, the obtained results are summarized and an outlook on possible future research activities is given.

Parts of this thesis were already the subject of previous works. The ground-state σ fluctuations have already been discussed in the authors bachelor thesis [45] and a region of approximate ground-state $O(6)$ symmetry outside the $O(6)$ dynamical symmetry limit was identified. The original work suffered from numerical limitations. A subsequent bachelor thesis [46] investigated the question whether the symmetry is exact or approximate. This doctoral thesis materially extends the previous research by offering theoretical insight, extending the approximate $O(6)$ symmetry beyond the ground state and identifying an experimental signature. Furthermore, the connection of the previously unrelated symmetry concepts of quasi dynamical symmetries and partial dynamical symmetries is investigated. The main results of the first part

of this thesis are already published in Refs. [47, 48]. Some results of the second part of this thesis have been submitted for publication in the proceedings of the XXI International School on Nuclear Physics, Neutron Physics and Applications (Varna 2015).

Part I.

Linking partial and quasi dynamical symmetries in rotational nuclei

1 Motivation

Understanding the dynamics of many-body systems, especially the emergence of regular and chaotic behavior, is important for many branches of physics [49]. While analytical solutions are generally available for systems consisting of a very small number of interacting particles, e.g. two gravitationally bound bodies, or for systems composed of a very large number of interacting particles, e.g. the thermodynamic description of gases, systems with an intermediate number of interacting particles are difficult to describe. Symmetries are of paramount importance to understand regular behavior of these complex many-body systems.

In the low-energy regime nuclei can be described, to good approximation, as a system of A interacting nucleons, which can be distinguished in protons (π) and neutrons (ν). These nucleons form strongly interacting quantum many-body systems and, being almost isolate from outside influences, offer ideal conditions to study the emergence of simple behavior in complex systems. The experimentally accessible nuclei range from $A = 1$ to $A \approx 300$ and exhibit a rich variety of nuclear structure phenomena. Exploiting the presence of symmetries can lead to a better understanding of these phenomena. While symmetry concepts are used in many theories of nuclear structure, e.g. in the construction of nucleon-nucleon potentials [26–28], they are most prominently featured in algebraic models. The IBM is a widely-used model of this type. It describes nuclei as a set of N interacting valence boson, corresponding to pairs of valence particles or holes, coupled to either $L = 0$ (s-boson) or $L = 2$ (d-boson). Underlying this description of nuclei is the $U(6)$ symmetry group. This group structure can be exploited to construct basis states via the quantum numbers of physically sensible, i.e. containing the angular momentum algebra $O(3)$, chains of nested sub-algebras. The three possible chains, starting with the $U(5)$, $O(6)$, and $SU(3)$ algebras, are the three DS limits of the model. If a Hamiltonian corresponds exactly to one of these chains, the resulting wave functions, energies, and all observables of interest can be analytically calculated. In addition, it is possible to understand the underlying physics via the correspondence to geometrical models. The DS limits can be interpreted as describing vibrational ($U(5)$), γ-soft ($O(6)$), and rotational nuclei ($SU(3)$). This combination of properties make the DS limits important benchmarks for the interpretation of experimental data in terms of nuclear structure.

The IBM has been very successful in describing the low-energy structure of quadrupole collective nuclei [50]. A commonly used approach within the IBM is the extended consistent-Q formalism (ECQF) [51, 52]. In second quantization its Hamiltonian can be written as the sum of a vibrational term (proportional to the number of d-bosons $\hat{n}_d$) and a quadrupole-quadrupole interaction term (proportional to $\hat{Q}^\chi \cdot \hat{Q}^\chi$)

$$\hat{H}_{ECQF} = \omega \left[(1-\xi)\,\hat{n}_d - \frac{\xi}{4N}\,\hat{Q}^\chi \cdot \hat{Q}^\chi \right], \tag{1.1}$$

where the parameter ω sets the energy scale and the parameters ξ and χ describe the nuclear structure (see Sec. 2.2 for details). For different values of ξ and χ the Hamiltonian $\hat{H}_{ECQF}$ is able to describe the symmetry limits $O(6)$ ($\xi = 1$, $\chi = 0$), $U(5)$ ($\xi = 0$, χ), and $SU(3)$ ($\xi = 1$, $\chi = -\sqrt{7}/2$). The parameter space of the ECQF can be represented by a triangle with the three DS limits placed at the corners (Fig. 1.1).

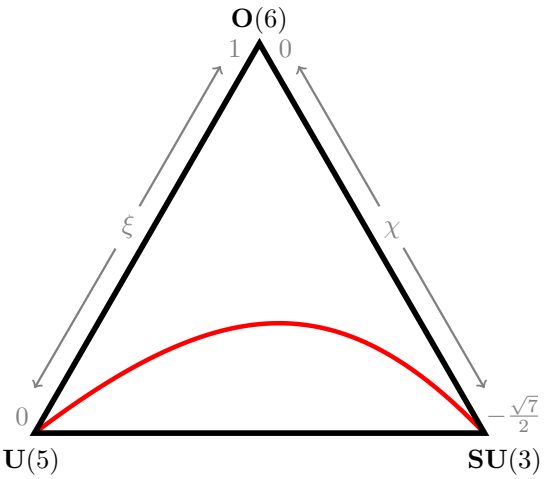

Figure 1.1.: Symmetry triangle of the IBM. The dynamical symmetry limits $O(6)$, $SU(3)$, and $U(5)$ correspond to the corners of the triangle, transitional nuclei are located in the interior. The location of an approximately regular region, known as the Alhassid-Whelan arc of regularity [53], is shown in red.

The best description of real nuclei is often achieved at intermediate values of ξ and χ. These nuclei are located in the transitional region inside the triangle and do not correspond to one of the symmetry limits. In these cases $\hat{H}_{ECQF}$ does include symmetry breaking terms. These terms induce mixing of basis states belonging to different DS limits and may lead to chaotic behavior. A study of the chaotic properties of the IBM [53], via statistical fluctuations of the spectrum and electromagnetic transitions using the Hamiltonian of Eq. (1.1), has confirmed the transitional region to be mostly chaotic. However, two approximately regular regions outside the symmetry limits were identified. The first one corresponds to the leg connecting the $U(5)$ and $O(6)$ symmetry limits. The regularity in this region is caused by the common $U(5) \supset O(3)$ substructure (cf. Sec. 2.3). Remarkably, another regular region connecting the $U(5)$ and $SU(3)$ vertices of the structure triangle was identified (see the red line in Fig. 1.1). This region is now known as the Alhassid-Whelan arc of regularity [53]. Approximate symmetries were believed to be the cause of regularity in this region and its discovery caused increased research interest in this area of physics. However, it took more than decade before an experimental signature, the near degeneracy of the 0_2^+ and 2_2^+ states, of nuclei corresponding to this regular region was identified [54]. In the meantime, the theoretical research of approximate symmetries introduced the notions of partial dynamical symmetries (PDS) [55] and quasi dynamical symmetries (QDS) [56]. This enabled a theoretical interpretation of the arc in terms of a $SU(3)$ quasi dynamical symmetry [57], almost twenty years after its initial discovery.

While the study of Alhassid and Whelan [53] maps the whole parameter space of the ECQF with respect to its degree of regularity, it is possible that a significant amount of regular behavior has not been discovered thus far. The quantal measures used to distinguish chaotic from regular behavior in the transitional region of the structure triangle were nearest-neighbor level-spacing distributions $P(s)$, distributions of $B(\mathrm{E2})$ intensities $P(y)$, and the Dyson-Mehta statistic $\Delta_3(L)$ [58]. These methods are based on extensive information about the whole system. For example, the $\Delta_3(L)$ statistic compares, via a least square fit, the deviation of the number of states in the energy interval $[0, L]$ to the best straight-line fit of these data. The value of $\Delta_3(L)$ is given by

the sum of least squares. If the average level distance has been renormalized to unity, $\Delta_3(L)$ should increase linearly with L for a regular system and logarithmically with L for a chaotic system. The measures $P(s)$ and $P(y)$ are both based on the idea of comparing distributions to their regular and chaotic limiting cases. For a selected value of spin and parity $P(s)$ considers the distribution of nearest-neighbor distances for all states. The resulting data is fitted by a Brody distribution [59]

$$P_\omega(s) = As^\omega \cdot \mathrm{e}^{-\alpha s^{1+\omega}}, \tag{1.2}$$

where A and α are normalization constants and s denotes the level distance in units of the average level distance. The Brody distribution is a phenomenological approach to describe chaotic ($\omega = 1$), regular ($\omega = 0$), and transitional dynamics ($0 < \omega < 1$). Thus, the degree of regularity of a system is deduced by the best fit value of ω. The general procedure for the distribution $P(y)$ of transition strengths $y = B(\mathrm{E2}; J_i^\pi \to J_f^\pi)$, which considers all E2 transitions between states of a given spin and parity, is similar. The role of the Brody distribution is taken by a χ^2 distribution in ν degrees of freedom [60], which interpolates between the chaotic (Porter-Thomas) distribution ($\nu = 1$) and the regular case ($\nu = 0$). The best fit value of ν again characterizes the degree of regularity in the system.

The described statistical measures are good at describing regular or chaotic behavior of the entirety of a quantum system. However, it is possible that subsets of a systems' states show a regular behavior (e.g. a PDS), which does not necessarily influence the dynamics of the whole system sufficiently to be detectable in any of the measures used by Alhassid and Whelan [53]. Thus, it is of considerable interest to investigate the ECQF parameter space with different methods that are capable of identifying a regular subset of states.

2 The Interacting Boson Approximation

This chapter introduces the Interacting Boson Approximation (IBA) which is an algebraic nuclear model. First, a short overview of the model is given in Sec. 2.1 with an emphasis on the consistent-Q Formalism, which is used extensively in this work. Then, the symmetry concepts underlying the IBA are discussed in Sec. 2.3 and the concepts of partial dynamical symmetries (PDS) and quasi dynamical symmetries (QDS) are presented. The notion of intrinsic states is introduced and their application to find equilibrium deformations is discussed (Sec. 2.4). Finally, the description of two-nucleon transfer reactions within the IBM-1 is discussed in Sec. 2.5. Unless indicated otherwise, notations and definitions in this chapter follow Iachello and Arima [37] to which the reader is referred to for an extensive review of the IBA.

2.1 Overview

The Interacting Boson Approximation, sometimes also called Interacting Boson Model (IBM), was introduced in the 1970s as a way to describe collective nuclear excitations [38]. Medium to heavy mass nuclei far from closed shells are often not accessible via the shell model, which describes nuclei as many nucleons moving independently (apart from residual interactions) in an average potential [61–63]. Configuration mixing and a large model space make shell model calculations quickly intractable for mid-shell nuclei. The IBM truncates the shell model space by only taking pairs of valence nucleons, coupled to valence bosons, into account. In the most basic version, the sd-IBM-1, only s- ($L = 0$) and d-bosons ($L = 2$) are considered. This is physically motivated by the effects of the short-range nucleon-nucleon interaction, which strongly favors the coupling of two nucleons within identical orbits to low-spin states and by the empirical fact that quadrupole excitations are the most important low-energy excitation mechanism for collective nuclei [64, 65]. Additionally, the effects of closed shells are neglected in the IBM and only valence nucleons (if the shell is less than half filled) or valence holes (if the shell is more than half filled) are taken into account. There is no distinction between proton and neutron bosons in the IBM-1, and hence no description of isovector excitations (e.g. mixed-symmetry states) is possible. This distinction is introduced in the IBM-2 [66, 67]. Even with these severe truncations the IBM-1 describes properties of many nuclei exceptionally well (see, e.g., Fig. 2.2 or McCutchan et al. [50]). What sets the IBM apart from most nuclear structure models is its underlying algebraic structure. In certain limiting cases the IBM-1 Hamiltonian leads to analytically computable wave functions and observables. Also quantum numbers for the classification of states and selection rules for electromagnetic transitions can be derived. These cases, called dynamical symmetry (DS) limits, correspond closely to analogues in the geometrical model of Bohr and Mottelson [36]. For the limiting case of small deformation ($\gamma \approx 0,\ \beta \ll 1$) it has been shown that a simple IBM Hamiltonian consisting of a d-boson energy term and a quadrupole interaction reduces to the Bohr Hamiltonian [68]. In this sense algebraic models, in general, and the IBM, in particular, are intermediate between microscopic and collective models. The connections of the IBM to the shell model and the collective model of Bohr and Mottelson are schematically illustrated in Fig. 2.1.

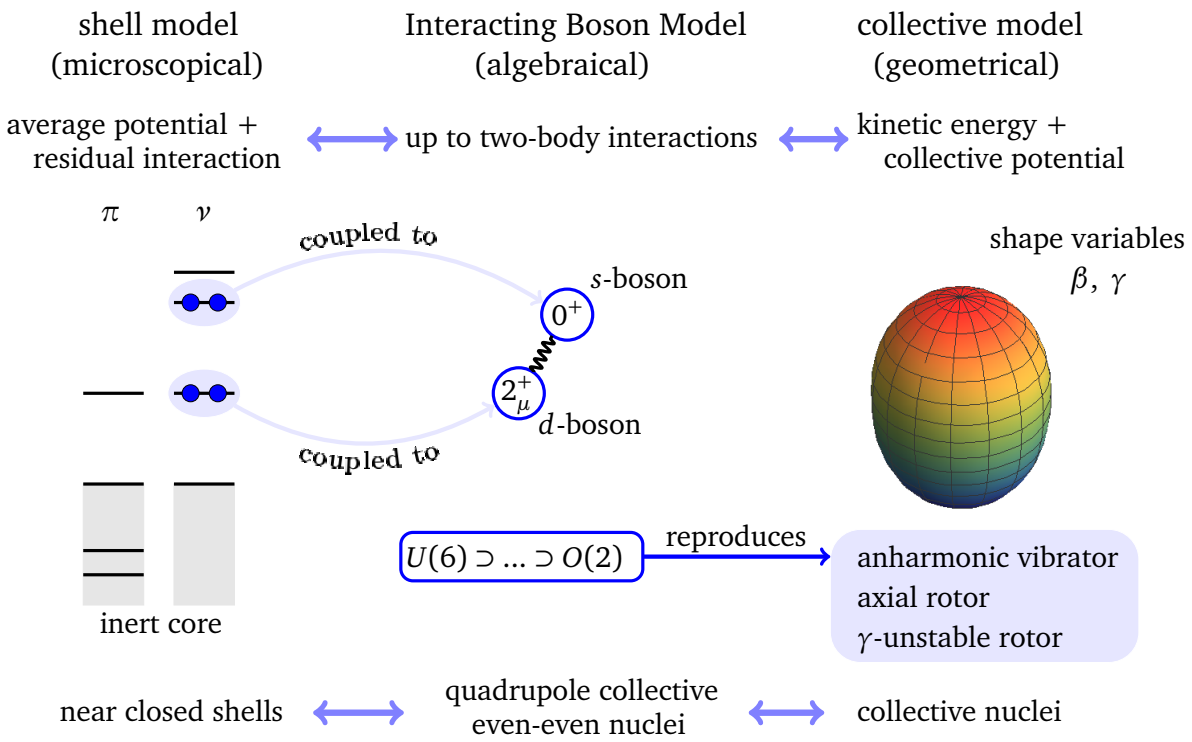

Figure 2.1.: Schematic illustration of the connections of the IBM to the shell model and the collective model.

The mathematical formalism of the IBM is second quantization. The physical picture of s- and d-bosons can be translated to appropriate creation and annihilation operators

$$\hat{s}^\dagger,\ \hat{d}^\dagger_\mu,\ \hat{s},\ \hat{d}_\mu \quad (\mu = 0,\ \pm 1,\ \pm 2) \tag{2.1}$$

where μ denotes the projection of the d-bosons spin on the quantization axis. Sometimes it is useful to use the alternative notation of $\hat{b}^\dagger_{l,m}$, $\hat{b}_{l,m}$ where $l = 0,\ 2$ denotes the spin of the boson and $m = -l,\ ...,\ l$ its projection. These operators obey typical Bose commutation relations

$$[\hat{s}, \hat{s}^\dagger] = 1, \tag{2.2}$$
$$[\hat{s}, \hat{s}] = [\hat{s}^\dagger, \hat{s}^\dagger] = 0, \tag{2.3}$$
$$[\hat{d}_\mu, \hat{d}^\dagger_{\mu'}] = \delta_{\mu\mu'}, \tag{2.4}$$
$$[\hat{d}_\mu, \hat{d}_{\mu'}] = [\hat{d}^\dagger_\mu, \hat{d}^\dagger_{\mu'}] = 0, \tag{2.5}$$
$$[\hat{s}, \hat{d}^\dagger_\mu] = [\hat{s}, \hat{d}_\mu] = [\hat{s}^\dagger, \hat{d}^\dagger_\mu] = [\hat{s}^\dagger, \hat{d}_\mu] = 0. \tag{2.6}$$

The creation operators can be used to build nuclear states starting from an initial state $|0\rangle$, which represents a doubly magic core (closed shells for both protons and neutrons). To create an N-boson state a total of N creation operators have to act on $|0\rangle$. Physical states have good angular momentum L and also a good projection of angular momentum M. To create model states with these characteristics the operators have to be coupled

$$|N, L, M\rangle = \left[\hat{b}^\dagger_{\alpha_1} \times \hat{b}^\dagger_{\alpha_2} \times ... \times b^\dagger_{\alpha_N}\right]^{(L)}_M |0\rangle = \sum_{m\,m'} C^{L\,M}_{l\,m\,l'\,m'}\, \hat{b}^\dagger_{\alpha_1}\, \hat{b}^\dagger_{\alpha_2} ... \hat{b}^\dagger_{\alpha_N} |0\rangle. \tag{2.7}$$

As the creation operators are spherical tensors the coupling constants $C^{LM}_{l\,m\,l'\,m'}$ are Clebsch-Gordan coefficients. In order to use these states to make predictions about nuclear structure one has to define appropriate physical operators in terms of boson operators. In general these operators are transformations of states. If one insists on the conservation of total boson number N, which is usually done in the IBM, the resulting operators are built from blocks of the form $\hat{b}^\dagger_\alpha \hat{b}_{\alpha'}$. In total there are 36 distinct generators $\hat{G}^k_\kappa(l,l')$ of these transformations. Again, ensuring good angular momentum via coupling of the operators results in

$$\hat{G}^k_\kappa(l,l') = \left[\hat{b}^\dagger_l \times \tilde{b}_{l'}\right]^{(k)}_\kappa, \tag{2.8}$$

where k and κ are the angular momentum and its projection, respectively. Additionally the spherical tensors $\tilde{b}_{l,\,m} = (-1)^{l+m}\,\hat{b}_{l,-m}$ are used instead of the usual annihilation operators in order to allow proper angular momentum coupling. The operators defined in Eq. (2.8) satisfy the commutation relations of $U(6)$, the unitary algebra in six dimensions. This is the basis for the algebraic properties of the IBM, which will be discussed in Sec. 2.3.

2.2 Hamiltonian operators and consistent-Q formalism

Keeping in mind that the Hamiltonian $\hat{H}$ should conserve total boson number N the most general form of H, keeping up to two body terms, can be written as

$$\hat{H} = E_0 + \sum_{\alpha\beta} \epsilon_{\alpha\beta}\,\hat{b}^\dagger_\alpha \hat{b}_\beta + \sum_{\alpha\beta\gamma\delta} u_{\alpha\beta\gamma\delta}\,\hat{b}^\dagger_\alpha \hat{b}^\dagger_\beta \hat{b}_\gamma \hat{b}_\delta \tag{2.9}$$

in terms of boson creation and annihilation operators. Here $\epsilon_{\alpha\beta}$ and $u_{\alpha\beta\gamma\delta}$ are parameters. This Hamiltonian covers the whole parameter space of the IBM, but is hard to handle in practice. The physical interpretation of single terms of the operator is not very intuitive. An equivalent way of writing $\hat{H}$ is the multipole form

$$\hat{H} = E_0 + E_0'\hat{N} + E_0''\hat{N}^2 + \epsilon\,\hat{n}_d + a_0\,\hat{P}^\dagger\cdot\hat{P} + a_1\,\hat{L}\cdot\hat{L} + a_2\,\hat{Q}^{-\frac{\sqrt{7}}{2}}\cdot\hat{Q}^{-\frac{\sqrt{7}}{2}} + a_3\,\hat{T}^{(3)}\cdot\hat{T}^{(3)} + a_4\,\hat{n}_d^2 \tag{2.10}$$

where the operators are defined as

$$\begin{aligned}
\hat{N} &= \hat{s}^\dagger\cdot\hat{s} + \hat{d}^\dagger\cdot\tilde{d}, && (2.11)\\
\hat{n}_d &= \hat{d}^\dagger\cdot\tilde{d}, && (2.12)\\
\hat{P} &= \frac{1}{2}\left(\hat{s}\cdot\hat{s} - \tilde{d}\cdot\tilde{d}\right), && (2.13)\\
\hat{L} &= \sqrt{10}\cdot\left[\hat{d}^\dagger\times\tilde{d}\right]^{(1)}, && (2.14)\\
\hat{Q}^\chi &= \left[\hat{s}^\dagger\times\tilde{d} + \hat{d}^\dagger\times\hat{s}\right]^{(2)} + \chi\cdot\left[\hat{d}^\dagger\times\tilde{d}\right]^{(2)}, \text{ and} && (2.15)\\
\hat{T}^{(3)} &= \left[\hat{d}^\dagger\times\tilde{d}\right]^{(3)} && (2.16)
\end{aligned}$$

while $a_0,\ a_1,\ a_2,\ a_3, a_4,\ E_0,\ E_0', E_0''$, and ϵ are parameters. The dot "$\cdot$" denotes a scalar product and is defined as

$$T^{(K)}\cdot U^{(K)} = (-1)^K\sqrt{2k+1}\left[T^{(K)}\times U^{(K)}\right]^{(0)}_0 = \sum_\mu (-1)^\mu\,U^{(K)}_\mu\,V^{(K)}_{-\mu} \tag{2.17}$$

where $T^{(K)}$ and $U^{(K)}$ are tensors of equal rank K. In the multipole expansion the Hamiltonian is explicitly a scalar with respect to angular momentum. Furthermore, the physical interpretation of the single terms is intuitive. E.g. the pairing force is represented by the term proportional to $\hat{P}^\dagger \cdot \hat{P}$ while quadrupole interactions are introduced by $\hat{Q} \cdot \hat{Q}$ and rotational energy is represented by $\hat{L} \cdot \hat{L}$. The Hamiltonians defined by Eq. (2.9) and Eq. (2.10) have many free parameters, which have to be determined by a fit to experimental data. A simpler parametrization, that is commonly used to describe nuclear data, is the consistent-Q formalism [51]. Its extended Hamiltonian [52] is given by

$$\hat{H}_{ECQF} = \omega \left[(1-\xi)\,\hat{n}_d - \frac{\xi}{4N}\,\hat{Q}^\chi \cdot \hat{Q}^\chi \right] \tag{2.18}$$

and contains only three parameters. In this parametrization the structure of the resulting wave functions is governed by the parameters ξ and χ while ω represents an overall scale [69]. The first term of $\hat{H}_{ECQF}$ is proportional to the number of d-bosons n_d whereas the second term introduces quadrupole interactions. By requiring the same value of the parameter χ in the Hamiltonian and the quadrupole transition operator $\hat{T}(E2) \propto \hat{Q}^\chi$, the number of free parameters is reduced by one. The parameter ξ moderates the relative strength between the d-boson and the quadrupole interaction terms. For $\xi = 0$ the resultant wave functions are purely vibrational. For $\xi = 1$ the Hamiltonian represents a rotational system. The parameter χ controls the amount of axial deformation. For $\xi = 1$ and $\chi = 0$ the Hamiltonian describes a γ-soft rotational nucleus, whereas for $\xi = 1$ and $\chi = -\sqrt{7}/2$ it describes an axially deformed rotor. Intermediate parameter values are used to describe transitional nuclei. Note that the Hamiltonian of the consistent-Q formalism does not describe the whole parameter space of the IBM. Several terms have been omitted from the Hamiltonian defined in Eq. (2.10) and only the quadrupole interactions and the harmonic oscillator term (proportional to the d-boson number) have been kept. The success of the consistent-Q formalism in describing the low-lying excited states and transition strengths for many nuclei indicates that this is a reasonable, physically justified truncation of the Hamiltonian. Consider, for example, the comparison of experimental and theoretical excitation energy spectra of ^{160}Gd shown in Fig. 2.2. The theoretical values are obtained from a fit of Eq. (2.18) to the experimental data. The resulting structure parameters of $\xi = 0.84$ and $\chi = -0.53$ have been determined by McCutchan et al. [50] using the technique of constant contours.

As $\hat{H}_{ECQF}$ depends on two variables, one experimental observable is not enough to determine the parameters. Using just one observable, e.g. $R_{4/2} = {}^{E(4_1^+)}/_{E(2_1^+)}$ or $R_{0,\gamma} = {}^{(E(0_2^+)-E(2_\gamma^+))}/_{E(2_1^+)}$ with the 2_γ^+ state being a member of the two-phononlike multiplet (rotational nuclei) or the bandhead of the quasi-γ band (rotational nuclei) [50], results in a function $\xi(\chi)$ which, in the parameter space of the extended consistent-Q formalism (ECQF), is a contour of constant $R_{4/2}$. In order to uniquely determine the structure parameters ξ and χ the intersection of at least two constant contours is needed. This method is schematically illustrated in Fig. 2.3. The graphical representation of the $\hat{H}_{ECQF}$ parameter space by a triangle will be discussed in Sec. 2.3.

2.3 Dynamical symmetries

What sets the IBM apart from other nuclear structure models is its group theoretical foundation. It was already noted, that the boson number conserving transformations defined in Eq. (2.8)

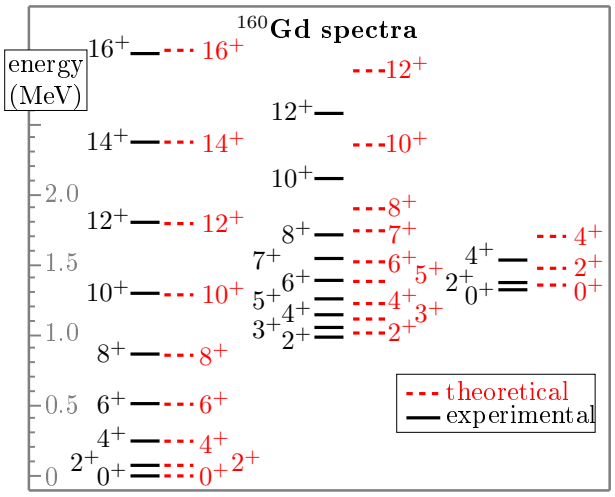

Figure 2.2.: Experimental (black) and theoretical (red) excitation energies of ^{160}Gd. Theoretical levels have been computed using Eq. (2.18). The fit parameters are taken from McCutchan et al. [50]. Figure taken and slightly modified from Kremer et al. [47].

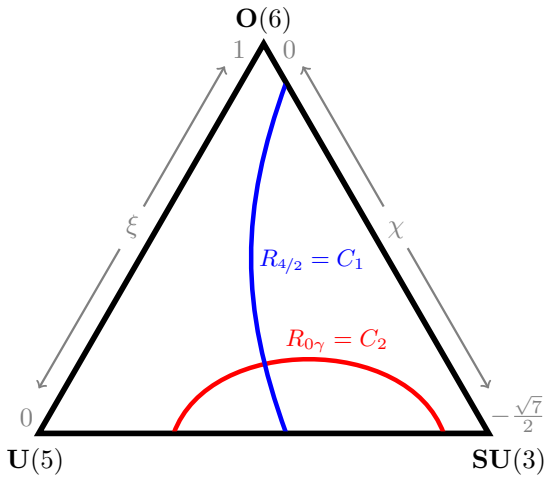

Figure 2.3.: Schematic illustration of the method of constant contours. Consider that experimentally the value $R_{4/2} = C_1$ and $R_{0\gamma} = C_2$ have been obtained for a given nucleus. Each of these results defines a contour within the parameter space of the ECQF (red and blue lines). The parameter values ξ and χ of the nucleus are then given by the point of intersection of the two contours.

are the generators of $U(6)$. In general, a set of n operators $\hat{O}_i$ $(i = 1, \ldots, n)$ forms a Lie algebra $\mathfrak{g}$, if they satisfy the Jacobi identity and close under commutation

$$\left[\hat{O}_i, \hat{O}_j\right] = \sum_{k=1}^{n} C_{ij}^{k} \hat{O}_k \quad \text{with } i, j \in \{1, \ldots, n\}\,. \tag{2.19}$$

The coefficients $C_{i,j}^{k}$ are called Lie structure constants. This set of operators is called generators of $\mathfrak{g}$, if there is no subalgebra $\mathfrak{g}'$ containing the generators that is smaller than $\mathfrak{g}$. For any Lie algebra there exists a set of operators $\hat{C}$ that satisfy

$$\left[\hat{C}, \hat{O}_i\right] = 0 \quad \forall\, i \in \{1, \ldots, n\}\,. \tag{2.20}$$

These operators are called Casimir operators and the number of independent Casimir operators is the rank of the algebra. If an irreducible matrix representation of the algebra exists, then, exploiting Schur's lemma [70], the Casimir operators are proportional to the identity in this representation. The constants of proportionality can be used to define quantum numbers. Consider, for example, the total boson number operator $\hat{N}$, which commutes with all the generators in Eq. (2.8), because these generators do not change the boson number N. Thus $\hat{N}$ is a Casimir operator of $U(6)$ and the corresponding quantum number is the total number of bosons N. In order to identify a complete set of quantum numbers, which uniquely characterizes all basis states, one has to find all possible chains of nested algebras starting from $U(6)$. Previously (Eq. (2.7)), the requirement of good angular momentum L and projection M was noted. These quantum numbers correspond to the algebras $O(3)$ and $O(2)$, respectively, which have to be included in any physically sensible subchain. This leaves just the three subchains starting with $U(5)$, $SU(3)$, and $O(6)$ as defined in Eqs. (2.21)-(2.23). Through its associated Casimir operators each algebra in a chain provides additional quantum numbers. In none of the chains the reduction to $O(3)$ is unique and additional quantum numbers (n_Δ, K, ν_Δ) are chosen to lift the resulting ambiguity [37]

$$\begin{array}{lllllll} U(6) \supset & U(5) \supset & O(5) \supset & O(3) \supset & O(2) & \text{anharmonic vibrator,} & (2.21) \\ N & n_d & \nu \quad n_\Delta & L & M & & \\ U(6) \supset & SU(3) \supset & & O(3) \supset & O(2) & \text{axial rotor,} & (2.22) \\ N & (\lambda,\mu) \quad K & & L & M & & \\ U(6) \supset & O(6) \supset & O(5) \supset & O(3) \supset & O(2) & \gamma\text{-unstable rotor.} & (2.23) \\ N & \sigma & \tau \quad \nu_\Delta & L & M & & \end{array}$$

A system is said to possess a dynamical symmetry (DS), if its Hamiltonian can be written in terms of the Casimir operators of one chain or, equivalently, if $\left[\hat{H}, \hat{C}(\mathbb{G})\right] = 0$ for the Casimir operators $C(\mathbb{G})$ of all groups $\mathbb{G}$ belonging to the respective chain. The states of the system are defined by the resulting quantum numbers and all the observables, e.g. excitation energies and transition strength, can be computed analytically.

If a wave function is known in a specific DS basis it can be transformed analytically into any other DS basis. This can be done by expanding the DS basis states as

$$|\,\alpha\,\rangle = \sum_\beta C_\beta^\alpha \;|\,\beta\,\rangle, \tag{2.24}$$

where C_β^α are transformation brackets, which depend on all quantum numbers α characterizing the given basis state of the initial DS limit and β denotes all quantum numbers corresponding to the target DS limit. The sum runs over all possible combinations of quantum numbers β. Consider, as an example, the transformation of a $\sigma = N$ $O(6)$ basis state to the $U(5)$ basis, which will be needed later. The $O(6)$ and $U(5)$ basis limits share the $O(5) \subset SU(3)$ substructure, which imposes the constraints $\nu = \tau$ and $n_\Delta = \nu_\Delta$ on the possible $U(5)$ basis states. The transformation brackets for this case are given by [37]

$$C^{\sigma=N}_{n_d,\,\nu=\tau} = \left(\frac{(N-\tau)!\,(N+3+\tau)!\,(n_d+1-\tau)!!}{2^{N+1}\,(N-n_d)!\,(N+1)!\,(n_d+1-\tau)!\,(n_d+3+\tau)!!} \right)^{1/2}. \tag{2.25}$$

The sum runs over all the possible values for the d-boson number, which are constrained by the condition $n_d = \tau, \tau+2, \tau+4, \ldots$ and by the total boson number $N \geq n_d$.

The DS limits find analogues in the geometrical model as anharmonic vibrator ($U(5)$ subchain), axial rotor ($SU(3)$ subchain), and γ-unstable rotor ($O(6)$ subchain). It is possible to rewrite the most general sd-IBM-1 Hamiltonian (Eq. (2.10)) in terms of Casimir operators as

$$\hat{H} = e_0 + e_1\,\hat{C}_1(U(6)) + e_2\,\hat{C}_2(U(6)) + \eta\,\hat{C}_2(O(6)) + \tilde{\epsilon}\,\hat{C}_1(U(5)) + \alpha\,\hat{C}_2(U(5)) + \beta\,\hat{C}_2(O(5)) + \delta\,\hat{C}_2(SU(3)) + \gamma\,\hat{C}_2(O(3)). \quad (2.26)$$

The subscripts of the Casimir operators show if they are a linear combination of the generators of the group $\mathbb{G}$ ($C_1(\mathbb{G})$) or if they are quadratic in the generators ($C_2(\mathbb{G})$). It is evident, that this Hamiltonian does not belong to any of the subchains of Eqs. (2.21)-(2.23), as it includes Casimir operators from all of the chains. Operators that do not belong to a specific chain cause mixing between basis states of this chain. The wave function created by the most general IBM Hamiltonian (Eq. (2.26)) can still be expressed in the basis states of any of the algebraic subchains, but they will be linear combinations of different basis states. A particular useful way of visualizing the symmetry structure of the IBM is the Casten triangle or symmetry triangle [71] shown in Fig. 2.4. The DS limits are represented by the corners of the triangle whereas all the points inside the triangle represent transitional regions without dynamical symmetries. Spherical nuclei are located near the $U(5)$ DS limit, whereas prolate deformed nuclei are located in the $SU(3)-O(6)$ region. In order to accommodate oblate deformed nuclei the triangle needs to be extended to include the $\overline{SU(3)}$ DS limit [72]. For different values of its parameters ξ and χ the Hamiltonian of the ECQF introduced in Eq. (2.18) is able to reproduce the DS limits as well as transitional nuclei.

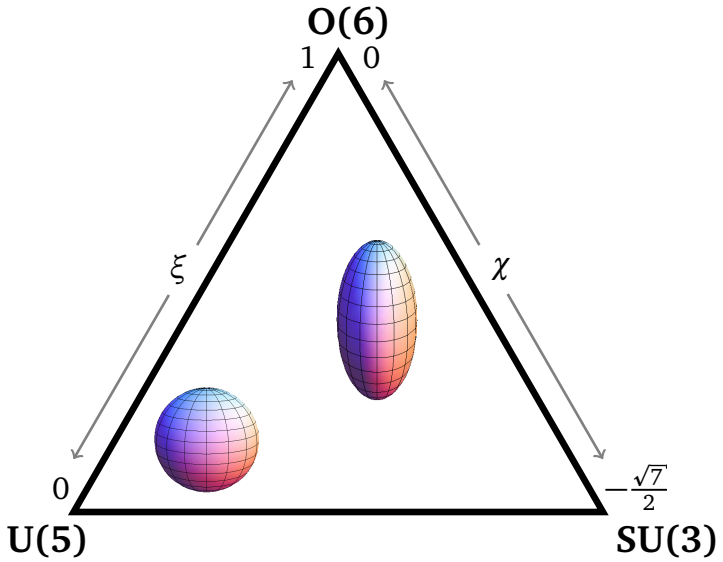

Figure 2.4.: Symmetry triangle of the IBA. The dynamical symmetry limits are in the corners of the triangle. The parameters ξ and χ cover the whole parameter space of the model. The location of a given nucleus inside the triangle can be inferred from a fit of Eq. (2.18) to the available experimental data.

This thesis focuses especially on the $O(6)$ DS limit, which will be discussed in greater detail below. Information about the other DS limits can be found in the book of Iachello and Arima

[37]. For $\tilde{\epsilon} = \alpha = \delta = 0$ the Hamiltonian introduced in Eq. (2.26) simplifies, as it contains Casimir operators of the $O(6)$ subchain only, and thus the excitation energies can be evaluated analytically

$$E(N, \sigma, \tau, L) = E_B + 2\,\eta\,\sigma\,(\sigma+4) + 2\,\beta\,\tau\,(\tau+3) + 2\,\gamma\,L\,(L+1). \tag{2.27}$$

Here $E_B = E_B(N)$ depends only on the total number of valence bosons N and absorbs the first three terms of $\hat{H}$ (Eq. (2.26)), which also depend on N only. The possible values of the quantum numbers can be found by starting with a representation of $U(6)$ characterized by the boson number N and then finding all the possible deconstructions in irreducible representations of the $O(6)$ chain. This leads to the following restrictions on the quantum numbers [37]

$$\begin{aligned}
\sigma &\in N, N-2, ..., N \bmod 2 && (2.28)\\
\tau &\in \sigma, \sigma-1, ..., 0 && (2.29)\\
\nu_\Delta &\in 0, 1, ..., x \quad \text{with } x \in \left\{ \left\{ \frac{\tau-2}{3}, \frac{\tau-1}{3}, \frac{\tau}{3} \right\} \cap \mathbb{N} \right\} && (2.30)\\
L &\in \lambda, \lambda+1, ..., 2\lambda-2, 2\lambda \quad \text{with } \lambda = \tau - 3\,\nu_\Delta && (2.31)\\
M &\in -L, ..., L. && (2.32)
\end{aligned}$$

The resulting excitation energy spectrum for $N = 4$ is displayed in Fig. 2.5. The states shown correspond to a complete and orthonormal basis for all sd-IBM-1 states with four valence bosons. Additionally, there are several selection rules applicable to electromagnetic transitions between states of a nucleus in the $O(6)$ DS limit, which can be used to test the $O(6)$ character of specific nuclei [73–75]. Most notably is the $\Delta\sigma = 0$ selection rule of E2 transitions that follows directly from the fact that the E2 transition operator $\hat{T}(\text{E2})$ is a generator of the $O(6)$ algebra and cannot connect different representations.

2.3.1 Partial dynamical symmetries

Most nuclei do not correspond to a dynamical symmetry and are located somewhere in the transitional region inside the symmetry triangle (Fig. 2.4). For these nuclei analytical solvability of wave functions and corresponding observables is, in general, lost. In these cases the Hamiltonian does not conform to a specific DS chain and cannot be expressed as a linear combination of Casimir operators, meaning that $\left[\hat{H}, \hat{C}_G\right] \neq 0$. In some situations, however, properties of the dynamical symmetries persist. These situations are known as PDS and can be categorized in three subtypes [76]. PDS of type I are cases in which part of the states keep all of the DS properties. This happens if there exists a subset of states $|\Psi^*\rangle$ for which $\left[\hat{H}, \hat{C}_G\right]|\Psi^*\rangle = 0$ holds for all Casimir operators of the dynamical symmetry chain. In this case the wave functions of these states can be analytically solved and corresponding observables can be calculated. The selection rules of the DS can be applied for transitions between states of this group. As a specific example see the $SU(3)$ PDS of type I, which is investigated in Refs. [77–79]. A different case occurs if $\left[\hat{H}, \hat{C}_G\right]|\Psi\rangle = 0$ holds for all states $|\Psi\rangle$ of the system, but only for select Casimir operators C_G^* of the DS chain. In this case the quantum number and selection rules associated with the operators C_G^* can be used for all states and transitions of the system - part of the symmetry persists for all of the states. For a practical example see the $O(5)$ PDS of type II discussed by Leviatan, Novoselsky, and Talmi [80]. Finally, the possibility exists that $\left[\hat{H}, \hat{C}_G\right]|\Psi^*\rangle = 0$ for a select set of

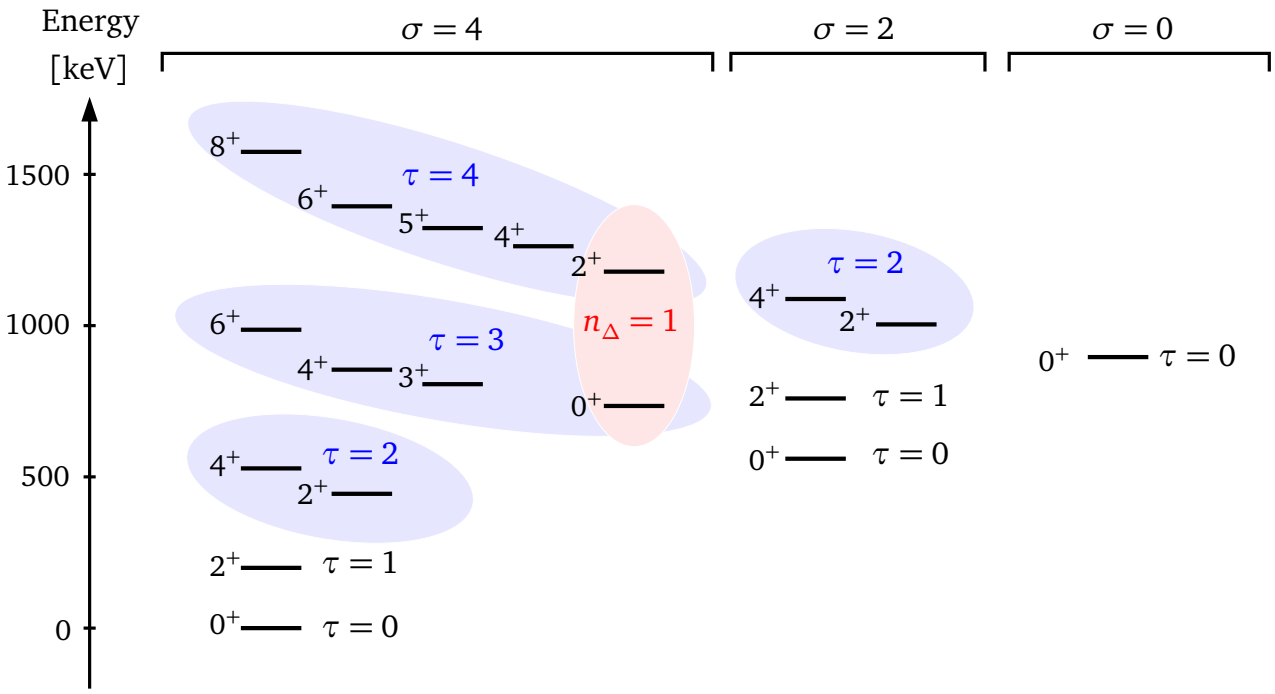

Figure 2.5.: Excitation energy spectrum for a Hamiltonian in the $O(6)$ DS limit with $N = 4$ valence bosons. The corresponding quantum numbers σ, τ, and L are displayed for each state. States belonging to the same τ multiplet are visually grouped via the blue shading. All states have $n_\Delta = 0$, unless indicated otherwise (red shading corresponds to $n_\Delta = 1$). Energies are calculated using Eq. (2.27) with typical parameter values ($E_B = 896$ keV, $\eta = -14$ keV, $\beta = 20.4$ keV, and $\gamma = 3$ keV).

states and for a select sets of Casimir operators. In this case some of the states keep some of the symmetry properties. A Hamiltonian with $O(6)$ PDS of type III is introduced and discussed by Leviatan and van Isacker [81] and is also used in this thesis (Eq. (3.7)). For a detailed review of PDS in the IBM-1 the reader is referred to Leviatan [76].

2.3.2 Quasi dynamical symmetries

QDS are another case of DS properties persisting in transitional regions. In a QDS the underlying symmetry is broken in the Hamiltonian and also for the individual states of the system. Nevertheless, it is possible that many observables, e.g. $R_{4/2} = {}^{E(4_1^+)}/_{E(2_1^+)}$ and $B(\mathrm{E2})$ values, resemble those of the closest DS. This can happen if linear combinations of states from different irreducible representations of one group form another irreducible representation, called an embedded representation, of the same group [82, 83]. Consider, for example, the $SU(3)$ DS chain and its analytical energy eigenvalues given by

$$E = E_0 + 2\gamma L(L+1) + \frac{2}{3}\delta\left(\lambda^2 + \mu^2 + \lambda\mu + 3\lambda + 3\mu\right) \tag{2.33}$$

where the parameters are those defined in Eq. (2.26). Now, assume that a Hamiltonian, e.g. one similar to that used by Rowe [56], is not $SU(3)$ symmetric, but produces yrast states that can be expanded in the $SU(3)$ basis states $|\lambda,\mu\rangle$ as follows:

$$|2_1^+\rangle = \alpha_A\,|\lambda_A,\mu_A\rangle + \alpha_B\,|\lambda_B,\mu_B\rangle + \dots\,, \tag{2.34}$$
$$|4_1^+\rangle = \alpha_A\,|\lambda_A,\mu_A\rangle + \alpha_B\,|\lambda_B,\mu_B\rangle + \dots\,, \tag{2.35}$$
$$|6_1^+\rangle = \alpha_A\,|\lambda_A,\mu_a\rangle + \alpha_B\,|\lambda_B,\mu_B\rangle + \dots \tag{2.36}$$

where the amplitudes α are independent of L and the subscripts denote different irreducible representation of $SU(3)$. Using Eq. (2.33) to determine the energies of these states yields a perfect rotational spacing with $R_{4/2} = 3.33$. Coherent (L-independent) mixing of basis states leads to the conservation of observables that correspond to the DS limit which is the definition of a QDS. Embedded representations play an important role in the separability of collective and intrinsic motion for many-body systems [83]. Furthermore, it was suggested by Bonatsos, McCutchan, and Casten [57] that a $SU(3)$-QDS underlies the Alhassid-Whelan arc of regularity [53], which is a region of enhanced regularity inside the parameter space of the ECQF.

2.4 Intrinsic state formalism and energy surface

So far the connection of the collective model of Bohr and Mottelson to the IBM has been introduced as the IBMs ability to reproduce the predictions of the geometrical collective model in the classical, $N \to \infty$, limit (see Fig. 2.1). However, it has been shown in Refs. [68, 84], that a more direct connection exists via the intrinsic states defined as

$$|N;\beta,\gamma\rangle = \frac{1}{\sqrt{N!}}\left[\frac{1}{\sqrt{1+\beta^2}}\left\{\hat{s}^\dagger + \beta\left(\cos\gamma\,\hat{d}_0^\dagger + \frac{1}{\sqrt{2}}\sin\gamma\left(\hat{d}_2^\dagger + \hat{d}_{-2}^\dagger\right)\right)\right\}\right]^N |0\rangle. \tag{2.37}$$

The variables β and γ are directly connected to the shape variables of the collective model. Using the intrinsic states it can be shown that the Hamiltonian of the ECQF (Eq. (2.18)) reduces to the Bohr-Hamiltonian in the limit of small deformations ($\gamma \approx 0,\ \beta \ll 1$) [68]. All the basis states of the IBM-1 can be obtained by projection from the intrinsic states given by Eq. (2.37). Thus one can find an upper bound of the ground-state energy by minimizing the quantity

$$E(\beta,\gamma) = \langle N;\beta,\gamma\,|\,\hat{H}\,|\,N;\beta,\gamma\rangle \tag{2.38}$$
$$= K\cdot\left(1+\beta^2\right)^{-2}\beta^2\left(a - b\,\beta\cos 3\gamma + c\,\beta^2\right), \tag{2.39}$$

where the second equality holds for the most general IBM Hamiltonian [85], K is a constant scale and the coefficients a, b, and c are those defined for the normal ordered Hamiltonian (Eq. (C.1)). The parameters β_0 and γ_0 obtained from minimization correspond to the equilibrium deformation of the system. Thus, the calculation of the energy surface, which is the set of energy values $E(\beta,\gamma)$ for all possible values of β and γ, allows a linkage of the parameters of any IBM Hamiltonian to the shape variables of Bohr and Mottelson. For the general IBM Hamiltonian three possible energy surfaces, corresponding loosely to the three DS limits of the model, are shown in Fig. 2.6. It is noteworthy that neither $O(6)$- nor $U(5)$-like energy surfaces show any dependence on γ. Prolate deformation $\beta > 0$ happens for both $O(6)$- and $SU(3)$-like systems. Historically, the correspondence of the DS limits to analogues in the collective model was largely based on calculations of the classical, $N \to \infty$, equilibrium deformations [36].

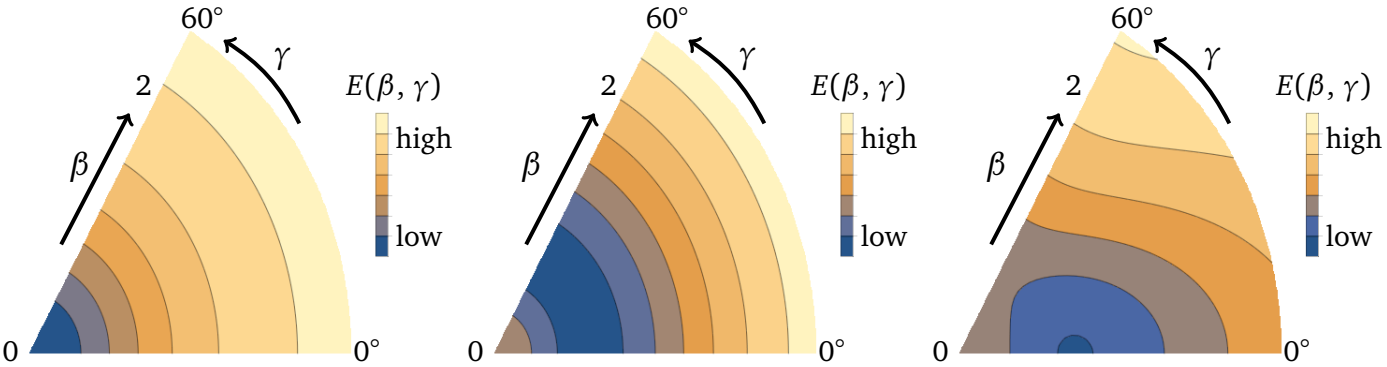

(a) $U(5)$-like energy surface for $b = 0$ and $a = c > 0$. The equilibrium deformation is $\beta_0 = 0$ and independent of γ.

(b) $O(6)$-like system for $b = 0$ and $a = -2c$ with γ independent equilibrium deformation $\beta_0 > 0$.

(c) $SU(3)$-like energy surface with $a = -2c$ and $b > 0$. The equilibrium deformation is $\gamma_0 = 0$ and $\beta_0 > 0$.

Figure 2.6.: Energy surface calculation for the general IBM Hamiltonian according to Eq. (2.39). The equilibrium deformation parameters β_0 and γ_0 correspond to the regions of low energy (blue). Note that the shown cases do not correspond to the DS limits exactly.

2.5 Two-nucleon transfer reactions

The IBM is capable to describe two-nucleon transfer reactions as the transfer of a single boson. In particular $L = 0$ transfer reactions are described by the transfer of a single s boson. For this case the transfer operators can be written as [37]

$$\hat{P}_{-}^{L=0} = p_0 \tilde{s} \qquad \text{and} \qquad \hat{P}_{+}^{L=0} = p_0 \hat{s}^{\dagger}, \tag{2.40}$$

where the plus sign means a boson is added to the nucleus, the minus sign means a boson is removed from the nucleus, and p_0 is a parameter. However, the transfer of nucleon pairs does depend on proton-neutron effects and shell structure. These effects can be explicitly introduced in the transfer operators via the proton (neutron) number N_π (N_ν) and the proton (neutron) pair degeneracy Ω_π (Ω_ν). The pair degeneracy is the maximum number of boson pairs possible in the particular major shell of interest. Take, for example, the rare-earth nucleus ^{160}Gd. It has 64 protons, which is within the 50-82 major shell and results in $\Omega_\pi = 16$, and 96 neutrons, which corresponds to the 82-126 major shell with $\Omega_\nu = 22$. With these considerations in mind the transfer operators can be written as [86]

$$\hat{P}_{+x}^{L=0} = \alpha_x \left(\frac{N_x + 1}{N + 1}\right)^{1/2} \hat{s}^{\dagger} \left(\Omega_x - N_x - \frac{N_x}{N}\hat{n}_d\right)^{1/2} \text{and} \tag{2.41}$$

$$\hat{P}_{-x}^{L=0} = \alpha_x \left(\Omega_x - N_x - \frac{N_x}{N}\hat{n}_d\right)^{1/2} \tilde{s} \left(\frac{N_x + 1}{N + 1}\right)^{1/2}, \tag{2.42}$$

where the subscript $x \in \{\pi, \nu\}$ has been introduced to indicate whether a pair of protons or neutrons is transferred and α_x are coupling amplitudes, which depend on the shell structure. If the d-boson number operator is approximated by its expectation value in the ground state

($\hat{n}_d \approx \langle 0_1^+ \mid \hat{n}_d \mid 0_1^+ \rangle$) the matrix elements of the transfer operators reduce to the calculation of matrix elements for $\tilde{s}$ or $\hat{s}^\dagger$, which can be determined analytically. The experimental data can then be compared to the transfer intensities which are given by

$$I_+ = |\langle N+1, \alpha' \mid \hat{P}^{L=0}_{+x} \mid N, \alpha \rangle|^2 \text{ and} \tag{2.43}$$

$$I_- = |\langle N-1, \alpha' \mid \hat{P}^{L=0}_{-x} \mid N, \alpha \rangle|^2 . \tag{2.44}$$

Here α and α' denote the additional quantum numbers necessary to describe the initial and final state, respectively. If the coupling amplitudes α_x are unknown it is still possible to compute relative transfer intensities within a major shell, which are independent of α_x. This method has been used successfully to interpret experimental data, e.g. for (t,p) and (p,t) experiments conducted in the Pt-Os region [87].

3 Symmetries inside the triangle

This section will show that PDS are abundant and that ground-state band $O(6)$ symmetry (PDS) may be realized in many rotational, $SU(3)$-like, nuclei. First, quantum number fluctuations are introduced as a method to measure the goodness of a given symmetry for a particular state. They are used to investigate the $O(6)$ symmetry of the ground state throughout the symmetry triangle of the IBA and a region of approximate ground-state $O(6)$ symmetry is identified. The intrinsic state formalism is used to derive an analytical expression for the region and to show that the $O(6)$ symmetry extends to the whole ground-state band (section 3.1). Then, the connection between $O(6)$ PDS and $SU(3)$ QDS is investigated and nuclei that possess both $O(6)$ PDS and $SU(3)$ QDS are identified (section 3.2). Finally, an experimental signature for nuclei exhibiting the $O(6)$ PDS is discussed in section 3.3.

3.1 $O(6)$ partial dynamical symmetry

The advantages of dynamical symmetries have already been motivated by the exact solvability of the eigenvalue problem, analytically computable observables, the existence of good quantum numbers and the applicability of selection rules (see Sec. 2.3). However, there are only few nuclei that resemble dynamical symmetries closely [88]. In most cases the Hamiltonian that reproduces a given nucleus best does not correspond to one of the dynamical symmetries. In these cases symmetry remnants, which manifest as PDS and/or QDS, can still exist and greatly simplify parts of the quantum mechanical problem. In order to study the whole parameter space of the IBM in search for such symmetry remnants a reliable measure is needed that quantifies how good a given symmetry is realized in the states of a given Hamiltonian. In this context the wave function entropy W_Ψ^B of a state Ψ has been introduced [89]

$$W_\Psi^B = -\sum_{i=1}^{n} |\alpha_{\Psi i}^B|^2 \ln |\alpha_{\Psi i}^B|^2 \tag{3.1}$$

with $\alpha_{\Psi i}^B = \langle i^B \mid \Psi \rangle$ and $\mid i^B \rangle$ a basis vector of a reference basis of dimension n. The wave function entropy is zero if Ψ corresponds exactly to one of the basis vectors and is maximized if Ψ is fully mixed with respect to the reference basis. The increase in wave function entropy is continuous between these two limiting cases. Thus, it is a method to measure the goodness of a particular symmetry realization in a specific state Ψ if the reference basis is chosen appropriately. The choice of reference basis is crucial and it has to be tailored to specific goal of the investigation. If one wants to study a DS then the DS basis is a good reference basis. For the study of PDS, e.g. for the study of an $O(6)$ PDS, choosing the reference basis as a DS basis does not work. To study a PDS one has to construct a reference basis in such a way that W_Ψ^B vanishes if, and only if, Ψ possesses the specific PDS. Thus, to study $O(6)$ PDS the reference basis can only contain one basis state for every possible value of the $O(6)$ quantum number σ. Such a reference basis $\mid i^B \rangle$ can be constructed as a sum over $O(6)$ basis states

$$\mid i^B \rangle = \sum_{\alpha_i} \mid \sigma_i, \alpha_i \rangle, \tag{3.2}$$

where α_i denotes all additional quantum numbers of the $O(6)$ basis and the sum runs over all possible α_i. The wave function entropy has been used to study quantum phase transition [72, 90, 91], regularity and chaos in quantum systems [92], and the structure of the Alhassid-Whelan arc of regularity [93].

A different method, which is also capable of measuring the symmetry content of a specific state, are quantum number fluctuations. This method depends on the fact that any given symmetry leads to a conserved quantity which is represented by a quantum number q. If this quantum number is a good characterization of a given state, then this state is a manifestation of the corresponding symmetry. The quantum number fluctuation Δq is defined as

$$\Delta q = \sqrt{\langle \Psi \mid q^2 \mid \Psi \rangle - \langle \Psi \mid q \mid \Psi \rangle^2} \tag{3.3}$$

and has first been introduced by Rainovski et al. [75]. Similarly to the wave function entropy the quantum number fluctuation vanishes exactly if the state Ψ possesses the symmetry represented by the quantum number q. Once the symmetry is perturbed and the quantum number is no longer exact for the state Ψ the quantum number fluctuations increase. In this sense Δq is also a measure of the goodness of a particular symmetry for a state Ψ.

With these measures in place it is possible to systematically study the parameter space of the IBM and classify the closeness of selected states to specific symmetries. The most general IBM-1 Hamiltonian using up to two-body terms (Eq. (2.10)) depends on nine parameters, which can be reduced to six for the description of excitation energies in a system with fixed number of bosons N [66]. In order to gain a better insight into the structure of the Hamiltonian and its wave functions it is useful to restrict the number of parameters further. The extended consistent-Q formalism has been successfully used for the description of many nuclei (see Sec. 2.2). Its Hamiltonian $\hat{H}_{ECQF}$ (Eq. (2.18)) depends on an overall scale ω and the structure parameters ξ and χ. The structure of the resulting wave functions $\Psi = \Psi(\xi, \chi)$ depend only on the structure parameters and is independent of the scale ω. By varying ξ and χ a systematic study of the full parameter space of $\hat{H}_{ECQF}$ is possible. Using $\hat{H}_{ECQF}$ it is possible to study the manifestation of $O(6)$ symmetry, characterized by the fluctuations of the $O(6)$ quantum number σ, in states inside the symmetry triangle. To evaluate the σ fluctuations of a particular state its wave function can be expanded in the $O(6)$ DS basis as

$$|\Psi(\xi,\chi)\rangle = \sum_i \langle N, \sigma_i, \tau_i, L \mid \Psi \rangle \, |N, \sigma_i, \tau_i, L\rangle \tag{3.4}$$

$$= \sum_i \alpha_i(\xi,\chi) \, |N, \sigma_i, \tau_i, L\rangle. \tag{3.5}$$

The sum runs over all possible states of the $O(6)$ DS basis. This relation makes it possible to rewrite Eq. (3.3) for the calculation of σ fluctuations

$$\Delta\sigma_\Psi = \sqrt{\sum_i \alpha_i^2 \, \sigma_i^2 - \left(\sum_i \alpha_i^2 \, \sigma_i \right)^2} \tag{3.6}$$

where the dependence of α_i on the structure parameters ξ and χ has been omitted for brevity. For the 0_1^+ ground state the σ fluctuations have been computed for the whole parameter space

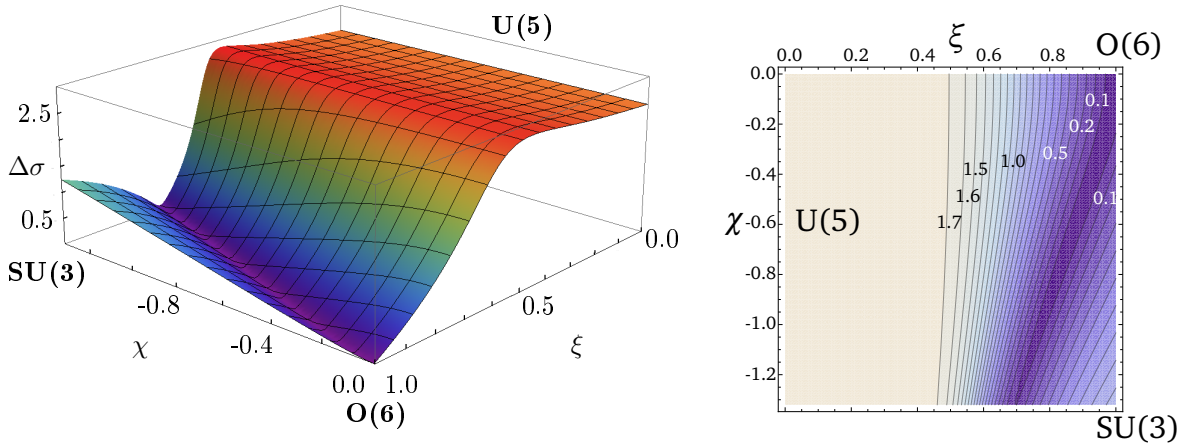

(a) Three dimensional plot of the σ fluctuations. Figure taken from Kremer et al. [47].

(b) Contour plot showing the magnitude of $\Delta\sigma$.

Figure 3.1.: Ground-state σ fluctuations for the full parameter space of the ECQF Hamiltonian (2.18) with $N = 14$ valence bosons (left) and $N = 8$ (right). The fluctuations vanish at the $O(6)$ dynamical symmetry limit, saturate towards the $U(5)$ dynamical symmetry limit, and are orders of magnitude lower in the valley.

of $\hat{H}_{ECQF}$ using the program ArbModel [94]. Details of the calculation are given in appendix A. The results for $N = 8$ valence bosons are visualized in Fig. 3.1 and have already been published in Refs. [45–47]. While the magnitude of $\Delta\sigma$ depends on the number of valence bosons N the behavior stays qualitatively the same for different N. At the $O(6)$ limit $\Delta\sigma$ vanishes by construction. Towards the $U(5)$ limit the fluctuations reach their maximum forming a broad plateau. In this region the wave function is maximally mixed with respect to the $O(6)$ basis states. The quantity σ is not a good quantum number in this part of the parameter space and the $O(6)$ symmetry is completely dissolved.

There is a pronounced region with low $\Delta\sigma$ connecting the $O(6)$ DS with the $SU(3) - U(5)$ edge of the structure triangle. In this valley the σ fluctuations are numerically approaching zero and, thus, indicate the preservation of σ as a good quantum number and $O(6)$ as a symmetry for the ground state outside of the $O(6)$ DS limit. The ground-state wave functions inside this region all behave similarly. Figure 3.2(a) shows the $O(6)$ basis state decomposition of the 0_1^+ wave function of ^{160}Gd, a nucleus located inside the valley of low sigma fluctuations according to the $\hat{H}_{ECQF}$ fit by McCutchan et al. [50]. The wave function is almost completely ($> 99\%$) composed of $O(6)$ basis states with $\sigma = N = 14$, which causes $\Delta\sigma$ to vanish. At the same time it is evident that the $O(5)$ symmetry, one of the subgroups of the $O(6)$ DS chain, is broken. The wave function is significantly mixed with respect to the quantum number τ. This is an example of a PDS of type III. In contrast consider the 0_1^+ wave function shown in Fig. 3.2(b). It is located in the plateau of high $\Delta\sigma$ ($\xi = 0.2$, $\chi = -0.6$) near the $U(5)$ DS limit. This wave function contains almost exclusively components with $\tau = 0$ (> 99.9 %). However, it is considerably mixed with respect to σ and its $\sigma = N$ component makes up less than 1 % of the total wave function. The fraction of $\sigma = N$ basis states contained in a wave function, denoted $f_{\sigma=N}$, is a

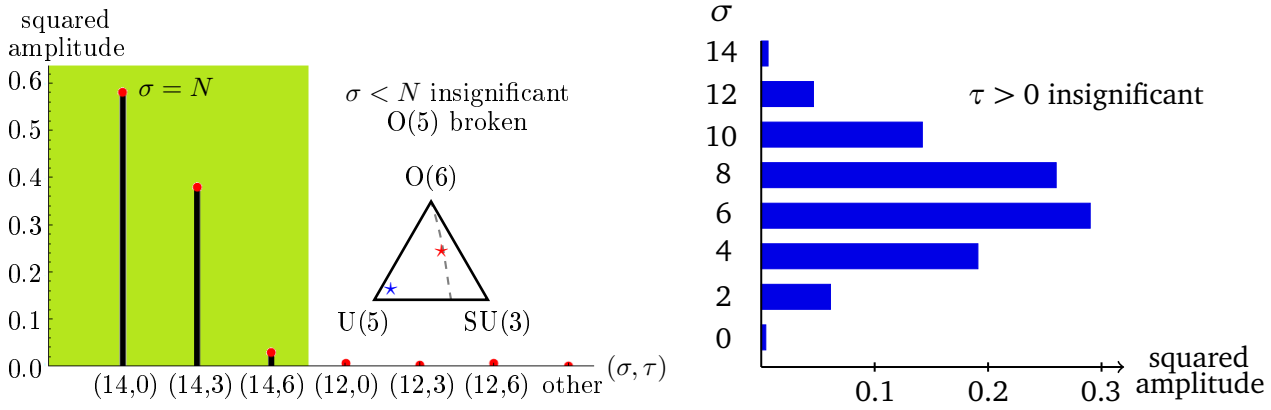

(a) The shown wave function has structure parameters $\xi = 0.84$ and $\chi = -0.53$, which is appropriate for the nucleus ^{160}Gd [50]. It is almost purely $\sigma = N$ (> 99 %), while it is mixed with respect to τ. The position in the symmetry triangle is shown by a red star in the inlet. Figure taken and slightly modified from Kremer et al. [47].

(b) The structure parameters for the wave function shown are $\xi = 0.2$ and $\chi = -0.6$. The position in the symmetry triangle is indicated by a blue star in the inlet of Fig. 3.2(a). The wave function is significantly mixed with respect to σ and almost pure with respect to $\tau = 0$ (> 99.9 %).

Figure 3.2.: Comparison of the $O(6)$ basis state decompositions for 0^+_{gs} wave functions of the ECQF Hamiltonian (Eq. (2.18)) inside (left) and outside (right) of the region of low σ fluctuations for $N = 14$ valence bosons.

measure of $O(6)$ symmetry content, for one specific representation with $\sigma = N$, complementary to $\Delta\sigma$. It has been shown by Leviatan and van Isacker [81] that the Hamiltonian

$$\begin{aligned}\hat{H}_M(\alpha) &= -\hat{C}_{O(6)} + \hat{N}(\hat{N}+4) + 2\alpha\hat{C}_{O(5)} - \alpha\hat{C}_{O(3)} \\ &\quad + 2\alpha\hat{n}_d(\hat{N}-2) + \sqrt{14}\,\alpha(d^\dagger\tilde{s} + s^\dagger\tilde{d})\cdot(d^\dagger\tilde{d})^{(2)}\end{aligned} \tag{3.7}$$

produces a $O(6)$ PDS of type III for certain values of its parameter α, which is similar to that described for 0^+_1 states in the region of low $\Delta\sigma$. For $\alpha = 0$ the Hamiltonian $\hat{H}_M$ is exactly $O(6)$ symmetric, because the Casimir operators $\hat{C}_{O(6)}$, $\hat{C}_{O(5)}$, $\hat{C}_{O(3)}$, and the operator $\hat{N}(\hat{N}+4)$ are diagonal in the $O(6)$ basis. For $\alpha > 0$ the operator $\hat{n}_d(\hat{N}-2)$ introduces mixing with respect to the quantum number τ, whereas the operator $(d^\dagger\tilde{s} + s^\dagger\tilde{d})\cdot(d^\dagger\tilde{d})^{(2)}$ causes mixing with respect to σ and τ. Remarkably the ground-state band of $\hat{H}_M$ stays $O(6)$ symmetric even for parameter values $\alpha > 0$. However, it has broken $O(5)$ symmetry and does not conserve τ as a good quantum number. This behavior is exactly like that of $\hat{H}_{ECQF}$ ground-state wave functions inside the valley of low $\Delta\sigma$. This raises the question how the two Hamiltonians are connected.

A way of exploring this connection is the overlap $O(\xi, \chi, \alpha)$ of the resulting ground-state wave functions. It is defined as

$$O(\xi, \chi, \alpha) = \langle \Psi(\xi, \chi) \,|\, \tilde{\Psi}(\alpha) \rangle, \tag{3.8}$$

where $\Psi(\xi, \chi)$ is the ground-state wave function of $\hat{H}_{ECQF}$ and $\tilde{\Psi}(\alpha)$ is the ground-state wave function of $\hat{H}_M$. For different values of α and N the overlap has been calculated for the whole

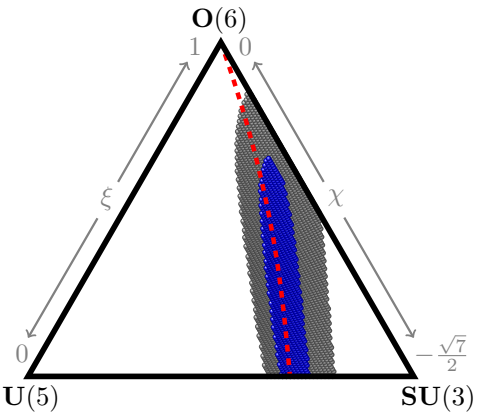

Figure 3.3.: This figure illustrates the overlap of the ground-state (0_1^+) wave function of $\hat{H}_{ECQF}$ with the ground-state wave function of $\hat{H}_M(\alpha)$ for $N = 16$ and $\alpha = 10$. The blue region indicates an overlap greater than 99 % and the gray region an overlap greater than 95 %. The ground-state wave functions of the two Hamiltonians are remarkably similar in the region of low σ fluctuations, which is indicated by the red dashed line.

parameter space of $\hat{H}_{ECQF}$ using ArbModel. Details of the calculation are given in appendix A. The result for $N = 16$ valence bosons and $\alpha = 10$ is shown in Fig. 3.3. The overlap of the ground-state wave functions is maximal for values of the structure parameters χ and ξ that correspond to the region of low $\Delta\sigma$. The colored areas in Fig. 3.3 indicate the regions where the maximum overlap reaches at least 99 % (blue) and at least 95 % (gray).

This similarity of ground-state wave functions for the differing Hamiltonians $\hat{H}_M$ and $\hat{H}_{ECQF}$ leads to several conclusions. First of all, as the ground-state band of $\hat{H}_M$ is exactly $O(6)$ symmetric for any value of α it follows that the ground-state wave function of $\hat{H}_{ECQF}$ is approximately $O(6)$ symmetric within any region of the ECQF parameter space where its overlap with the ground-state wave function of $\hat{H}_M$ approaches unity. Furthermore, it is shown Leviatan and van Isacker [81], that the ground-state band of $\hat{H}_M$ is projected from the intrinsic state

$$| c, N \rangle = (N!)^{-1/2} \left(\hat{b}_c^\dagger\right)^N \; | 0 \rangle \quad \text{with the condensate boson} \quad \hat{b}_c^\dagger = \frac{1}{\sqrt{2}} \left(\hat{d}_0^\dagger + \hat{s}^\dagger\right). \tag{3.9}$$

This intrinsic state corresponds to $\beta = 1$ and $\gamma = 0$ (cf. Eq. (2.37)). The large ground-state overlap suggests that the same intrinsic state is also a good approximation to the ground-state band of $\hat{H}_{ECQF}$ along the valley of low $\Delta\sigma$ in a variational sense. This can be exploited to generate an analytical description (to order $1/N$) of the location of the valley in terms of the structure parameters.

The energy surface $E(\beta, \gamma)$ can be used to find the equilibrium deformation of any given IBM Hamiltonian [36, 68]. It is defined as the expectation value of the Hamiltonian in an intrinsic state. For the most general IBM Hamiltonian it can be written as

$$E(\beta,\gamma) = \frac{\langle \Psi(\beta,\gamma) \mid H \mid \Psi(\beta,\gamma) \rangle}{\langle \Psi(\beta,\gamma) \mid \Psi(\beta,\gamma) \rangle} \tag{3.10}$$

$$= K \cdot \left(1+\beta^2\right)^{-2} \beta^2 \left(a - b\,\beta \cos 3\gamma + c\,\beta^2\right) \tag{3.11}$$

where K is a constant and a, b, and c are coefficients that depend on the parameters of the Hamiltonian. The equilibrium deformation is found by minimizing $E(\beta,\gamma)$. In order to find the minimal energy the extremum equations

$$\frac{\partial E(\beta,\gamma)}{\partial \beta} = 0 \text{ and} \tag{3.12}$$

$$\frac{\partial E(\beta,\gamma)}{\partial \gamma} = 0 \tag{3.13}$$

have to be satisfied simultaneously. Together with the requirement that the solution should have $\beta = 1$ and $\gamma = 0$ this leads to the constraint $b = 2c$. For the limiting case of a large number of valence bosons N the coefficients a, b, and c of the general IBM Hamiltonian have been computed by Leviatan [95]. Simplifying this general solution to the one appropriate for $\hat{H}_{ECQF}$, as detailed in appendix C, yields

$$b = -\frac{\omega}{N}\xi\chi\sqrt{\frac{2}{7}} \text{ and} \tag{3.14}$$

$$c = \frac{\omega}{N}\left(1-\xi-\frac{\xi\chi^2}{14}\right). \tag{3.15}$$

The constraint $b = 2c$ defines a parametrization for the valley of low σ fluctuations for large numbers of valence bosons N

$$\xi(\chi) = \frac{1}{1-\sqrt{\frac{1}{14}}\chi+\frac{1}{14}\chi^2}. \tag{3.16}$$

A comparison of this parameterization to numerical results for different numbers of valence bosons N is shown in Figure 3.4. For large numbers of valence bosons this description of the region of low $\Delta\sigma$ is very good (Fig. 3.4(a)). For small numbers of valence bosons the numerically calculated region of approximate ground-state $O(6)$ symmetry shows a curvature towards the $SU(3)-O(6)$ edge of the symmetry triangle, which is not reproduced by the large N limit (Fig. 3.4(b)). With increasing N the numerical results converge toward the theoretical large N limit. This convergence is reasonably fast, such that for $N = 16$, a valence boson number typical for the description of rare earth nuclei, the parametrization of Eq. (3.16) gives a very good description of the region of low $\Delta\sigma$.

The existence of the region of low σ fluctuations for the ground state has recently been confirmed by calculations of the wave function entropy [96]. It was already suggested in the authors BSc. thesis [45] that the region of low $\Delta\sigma$ persists throughout the ground-state band. This was based on numerical results and can now be understood theoretically. If the intrinsic state with $\beta = 1$ and $\gamma = 0$ is a good approximation to the ground-state band of $\hat{H}_{ECQF}$ in the valley of low σ fluctuations (as shown above), then the whole ground band retains the symmetry properties of the ground state. This intrinsic state has good $O(6)$ quantum number σ and, thus, this also holds for the whole ground-state band of $\hat{H}_{ECQF}$ in the valley of low $\Delta\sigma$, which, approximately, can be assumed to be a projection from this intrinsic state. Numerical calculations of $\Delta\sigma$ for $L > 0$ confirm this conclusion and are shown for the case of ^{160}Gd on the left hand side of Fig. 3.6 (showing the complementary measure $f_{\sigma=N}$), for some rare earth nuclei in Tab. 3.1, and for the whole parameter space of the ECQF Hamiltonian in appendix B.

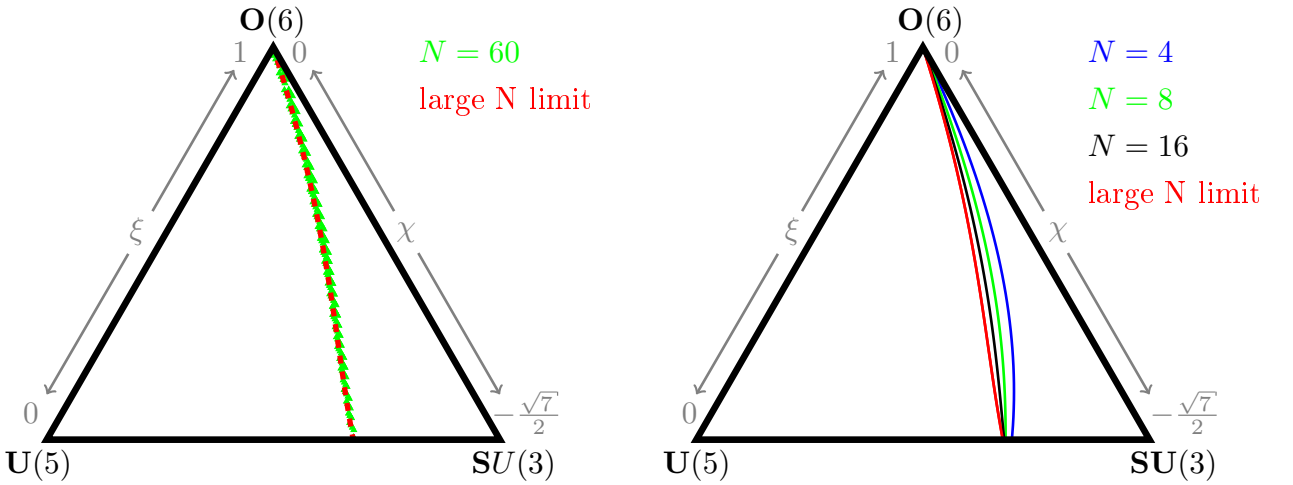

(a) The green area in the ECQF symmetry triangle shows the numerically calculated region of low $\Delta\sigma$ for $N = 60$ valence bosons. The red dashed line shows the theoretical prediction for the large N limit. Figure taken and slightly modified from Kremer et al. [47].

(b) For small N the numerically calculated region of low $\Delta\sigma$ converges to the large N solution (red) with increasing N. The numerical results shown correspond to $N = 4$ (blue), $N = 8$ (green), and $N = 16$ (black).

Figure 3.4.: Comparison of the large N theoretical prediction of the valley of low $\Delta\sigma$ as defined in Eq. (3.16) with numerical results for different boson numbers N calculated by Eq. (3.6).

With increasing L the σ fluctuations throughout the whole structure triangle, including the plateau of large $\Delta\sigma$ towards the $U(5)$ DS limit, decrease. This is due to the fact that states with spin L can only be composed of states with $\tau \geq L/2$ and consequently also $\sigma \geq L/2$. This significantly reduces the available components of the $O(6)$ basis for construction of states with high L and, thus, reduces $\Delta\sigma$ for these states. In the limiting case of $L \geq 2N-2$ only $O(6)$ basis states with $\sigma = N$ can be used to construct this state and $\Delta\sigma$ vanishes in the whole symmetry triangle. Consider, for example, the system with $N = 4$ valence bosons. The corresponding $O(6)$ basis states are shown in Fig. 2.5. For $L \geq 5$ only $O(6)$ basis states with $\sigma = 4$ can contribute to the construction of these states and $\Delta\sigma$ vanishes. Furthermore, it is evident by inspection of Fig. 2.5 that the σ fluctuations also vanish for $L = 3$, as there is only one possible $O(6)$ basis state with $L = 3$.

3.2 Relation to $SU(3)$ quasi dynamical symmetry

In order to identify real nuclei that exhibit the $O(6)$ PDS introduced in Sec. 3.1, one has to rely on fits of Eq. (2.18) to experimental data. Such a fit, taking excitation energies and electromagnetic transitions into account, has been performed by McCutchan et al. [50] for nuclei in the rare earth region. Using these values for the structure parameters χ and ξ nuclei close to the region of ground-band $O(6)$ symmetry can be identified (see Fig. 3.5). These nuclei are usually interpreted as rotational, $SU(3)$-like, nuclei. Consider for example the excitation energy spectrum of ^{160}Gd as shown in Fig. 2.2. The ground-state band shows almost perfectly

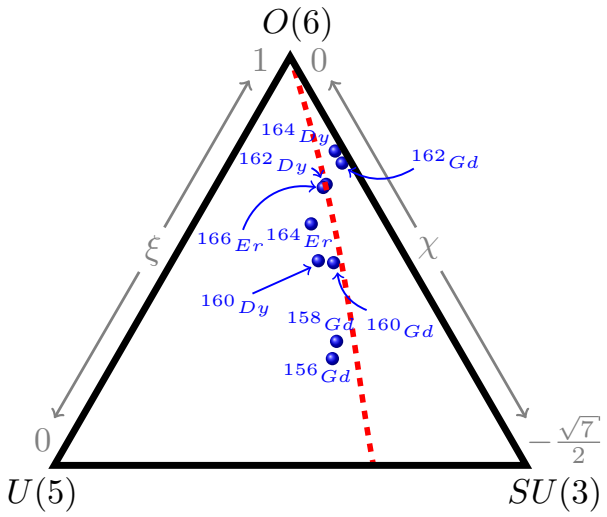

Figure 3.5.: Position of selected rare earth nuclei (blue dots) in the parameter space of the extended consistent-Q formalism (Eq. (2.18)) according to McCutchan et al. [50]. The region of low $\Delta\sigma$ (Eq. (3.16)) is indicated by a red dashed line.

rotational level spacing. For the other nuclei of Fig. 3.5 the situation is similar. Their $R_{4/2} = {}^{E(4_1^+)}/_{E(2_1^+)}$ values, shown in the last column of Tab. 3.1, correspond closely to 3.33, which is the theoretical value for a rigid rotor. For an $O(6)$-like nucleus the 4_1^+ state and the 2_1^+ state correspond to $\tau = 2$ and $\tau = 1$ states respectively (see Fig. 2.5). According to Eq. (2.27) this leads to an expectation of $R_{4/2} = 2.5$, which is far from the observed values.

In order to investigate how the $SU(3)$-like spectra and the possible ground-state band $O(6)$ symmetry are connected to each other it is instructive to take a look at the wave functions of these nuclei. For ^{160}Gd the decomposition of ground-state band wave function with $L = 0, 2, 4$ into $O(6)$ basis states and $SU(3)$ basis states is shown in Figure 3.6.

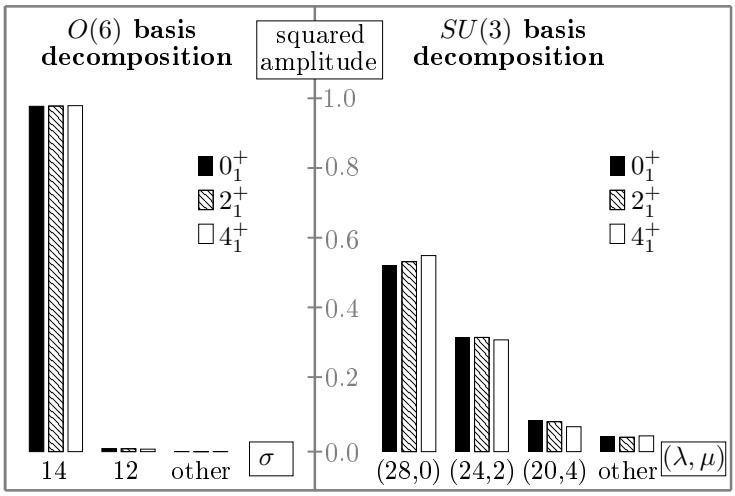

Figure 3.6.: $O(6)$ (left) and $SU(3)$ (right) basis decomposition of the yrast states with $L = 0, 2, 4$ of ^{160}Gd. Parameter values ($\xi = 0.84$, $\chi = -0.53$) taken from McCutchan et al. [50]. Figure taken and slightly modified from Kremer et al. [47].

The ground-state band wave functions show a very high purity of $\sigma = N = 14$ and correspondingly low σ fluctuations. Thus, ^{160}Gd is an example of an $O(6)$ PDS. At the same time the wave functions are admixtures of different $SU(3)$ basis states and are neither pure with respect to λ nor μ, and the $SU(3)$ symmetry is broken. However, the mixing amplitudes of $SU(3)$ basis states stay almost constant for the complete ground-state band. This coherent, L-independent mixing leads to an $SU(3)$-like excitation energy spectrum, even though the $SU(3)$ symmetry is broken. The nucleus ^{160}Gd exhibits a $SU(3)$ QDS. The situation is similar for the other rare earth nuclei of Fig. 3.5. They show a rotational spectrum brought about by an $SU(3)$ QDS while also having an almost exactly $O(6)$ symmetric ground-state band, exhibiting an $O(6)$ PDS.

Table 3.1 summarizes the calculated σ fluctuations for the yrast state with $L = 0, 2, 4$ for these nuclei, which are extremely low. It also lists the fractions of $\sigma = N$ contained in the respective wave functions, which is extremely high (> 95 %). The coincidence of a PDS and a QDS of different, incompatible, symmetries is a direct consequence of the fact that the ground-state band of $\hat{H}_{ECQF}$ inside the valley of low $\Delta\sigma$ can be approximated by projection from one intrinsic state. The existence of this underlying structure explains the coherent mixing and the emergence of the $SU(3)$ QDS. If the intrinsic state also has $\beta = 1$ and $\gamma = 0$ this will result in an $O(6)$ PDS. Thus, for the first time, a link between the previously unrelated concepts of PDS and QDS is established.

Table 3.1.: Calculated $\Delta\sigma_L$ and $f^{(L)}_{\sigma=N}$ for rare-earth nuclei in the vicinity of the identified region of approximate ground-band $O(6)$ symmetry. The rotational character of these nuclei is exemplified by the ratio $E(4^+_1)/E(2^+_1)$, which is close to 3.33, the theoretical value for a rigid rotor, for all the listed nuclei. Table taken from Kremer et al. [47,48] and slightly extended. Excitation energy data taken from Ref. [97].

Nucleus	N	ξ	χ	$\Delta\sigma_0$	$f^{(0)}_{\sigma=N}$	$\Delta\sigma_2$	$f^{(2)}_{\sigma=N}$	$\Delta\sigma_4$	$f^{(4)}_{\sigma=N}$	$R_{4/2}$
^{156}Gd	12	0.72	-0.86	0.46	95.3 %	0.43	95.8 %	0.38	96.6 %	3.24
^{158}Gd	13	0.75	-0.80	0.35	97.2 %	0.33	97.5 %	0.30	97.9 %	3.29
^{160}Gd	14	0.84	-0.53	0.19	99.1 %	0.19	99.2 %	0.17	99.3 %	3.30
^{162}Gd	15	0.98	-0.30	0.17	99.3 %	0.17	99.3 %	0.16	99.3 %	3.30
^{160}Dy	14	0.81	-0.49	0.44	96.2 %	0.39	96.4 %	0.36	96.8 %	3.27
^{162}Dy	15	0.92	-0.31	0.07	99.9 %	0.07	99.9 %	0.06	99.9 %	3.29
^{164}Dy	16	0.98	-0.26	0.13	99.6 %	0.13	99.6 %	0.13	99.6 %	3.30
^{164}Er	14	0.84	-0.37	0.39	96.5 %	0.37	96.7 %	0.35	97.1 %	3.28
^{166}Er	15	0.91	-0.31	0.12	99.7 %	0.11	99.7 %	0.10	99.7 %	3.29

3.3 Two-nucleon transfer as experimental signature of $O(6)$ PDS in nuclei

While the $SU(3)$ QDS is easy to observe experimentally, e.g. via the $R_{4/2}$ values displayed in Tab. 3.1, there is as yet no experimental signature for nuclei exhibiting $O(6)$ PDS. Two-nucleon transfer reactions are a promising way of investigating the $O(6)$ PDS. For two-nucleon transfer

without transfer of angular momentum ($L = 0$) and states belonging to the $O(6)$ DS limit $|\, N, \sigma, \tau, \nu_\Delta, L, M_L \,\rangle$ these reactions obey the selection rules

$$\Delta\sigma = \pm 1 \qquad \text{and} \qquad \Delta\tau = 0. \tag{3.17}$$

For the $|\, \sigma = \sigma_{max}, \tau = 0 \,\rangle$ ground states of three successive nuclei with $N-1$, N, and $N+1$ valence bosons these selection rules are illustrated in Fig. 3.7.

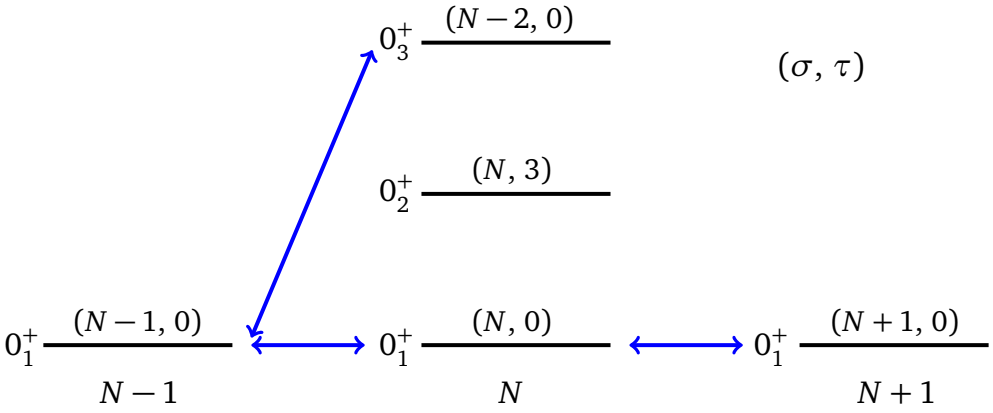

Figure 3.7.: Two-nucleon $L = 0$ transfer selection rules for the $O(6)$ DS chain. All allowed transitions to and from the nucleus with N valence bosons are shown.

While the nuclei in the valley of low $\Delta\sigma$ do not belong to the $O(6)$ DS limit, two-nucleon transfer reactions can still be used to investigate whether the sd-IBM-1 description of these nuclei is consistent with the experimentally observed transition intensities. The ground-state wave functions $|\, N, 0_1^+ \rangle$ in the region of low sigma fluctuations can be written as a sum of $O(6)$ basis states $|\, \sigma, \tau \,\rangle$:

$$|\, N, 0_1^+ \rangle = \alpha_1 \,|\, N, 0 \,\rangle + \alpha_2 \,|\, N, 3 \,\rangle + \alpha_3 \,|\, N, 6 \,\rangle + \beta \,|\, \text{remainder} \,\rangle \tag{3.18}$$

where α_1, α_2, α_3, and β are amplitudes and the remainder contains all $O(6)$ basis states with $\sigma \neq N$ as well as those with $\sigma = N$ and $\tau > 6$. It was already shown that the $L = 0$ projection of the intrinsic state given by Eq. (3.9) is a good approximation to the ground-state wave function in the valley of low $\Delta\sigma$. This implies that the coefficients α_1, α_2, and α_3 should be roughly constant for nuclei inside the valley (up to finite N effects), because the structure of the intrinsic state does not depend on the parameters ξ and χ. For the identified nuclei with low σ fluctuations these coefficients are shown in the lower part of Tab. 3.2 and the coefficients α_1, α_2, and α_3 do not vary much from nucleus to nucleus. This pattern leads to constructive interference of the dominant terms for the matrix elements of ground state to ground state transfer reactions between these nuclei ($\alpha_i \, \alpha_i' \approx \alpha_i^2 > 0 \, \forall \, i \in \{1, 2, 3\}$) and correspondingly large two-nucleon transfer intensities.

Inside the region of low $\Delta\sigma$ the IBM yields $\beta^2 \ll 1$ and the ground-state wave functions are characterized by the first three terms in Eq. (3.18). If this is a good description of real nuclei, e.g. the ones identified in Tab. 3.1, then two-nucleon transfer reaction intensities between ground states of these nuclei should be reproducible quantitatively within the IBM even if only the dominant parts of the wave functions with $\sigma = N$ and $\tau = 0, 3, 6$ are considered.

Outside the region of low σ fluctuations the remainder of the ground-state wave functions becomes important and the theoretical description of two-nucleon transfer intensities should only be possible by explicitly taking the remainder into account. The dominant component of the remainder (near the region of low $\Delta\sigma$) is $|\, \sigma = \sigma_{max} - 2,\, \tau = 0 \rangle$. Thus, the remainder of the nucleus with $N+1$ valence bosons can connect to the dominant $|\, \sigma = \sigma_{max},\, \tau = 0 \rangle$ component of the ground-state wave function of the nucleus with N bosons (see the selection rules in Fig. 3.7) in, e.g., a (p,t) reaction. This introduces terms of order $\alpha_1 \beta'$ (where primed indices stand for the nucleus with $N+1$ valence bosons and unprimed for the nucleus with N valence bosons) into the matrix element, which are larger than the $\beta\,\beta'$ terms stemming from the matrix elements of the remainders and are the limiting factor for the accuracy of this description of two-nucleon transfer intensities. For many nuclei inside the region of low $\Delta\sigma$ absolute cross section data for the ground state to ground state (p,t) reaction are available [98, 99] and will be used to compare to the IBM predictions.

In order to calculate the two-nucleon transfer intensities (Eqs. (2.43) and (2.44)) for ground state to ground state transitions one has to calculate the corresponding matrix elements of the transfer operators of Eqs. (2.41) and (2.42). From this point forward only matrix elements of $\hat{P}^{L=0}_{-x}$ ($x \in \{\nu, \pi\}$), needed for the comparison to experimental (p,t) reaction data, will be considered. The matrix elements of $\hat{P}^{L=0}_{+x}$ can be calculated similarly (see appendix D). Using the selection rules (Eq. (3.17)) and neglecting terms of order $\beta'\,\alpha_i$ and $\beta\,\beta'$ (as discussed above) the matrix element simplifies to:

$$\begin{aligned}
\langle N, 0_1^+ \,|\, \hat{P}^{L=0}_{-x} \,|\, N+1, 0_1^+ \rangle = \quad & \alpha_1\,\alpha_1' \,\langle N, 0 \,|\, \hat{P}^{L=0}_{-x} \,|\, N+1, 0 \rangle \\
& + \alpha_2\,\alpha_2' \,\langle N, 3 \,|\, \hat{P}^{L=0}_{-x} \,|\, N+1, 3 \rangle \qquad (3.19) \\
& + \alpha_3\,\alpha_3' \,\langle N, 6 \,|\, \hat{P}^{L=0}_{-x} \,|\, N+1, 6 \rangle \\
= C \cdot \big(& \alpha_1\,\alpha_1' \,\langle N, 0 \,|\, \tilde{s} \,|\, N+1, 0 \rangle \\
& + \alpha_2\,\alpha_2' \,\langle N, 3 \,|\, \tilde{s} \,|\, N+1, 3 \rangle \qquad (3.20) \\
& + \alpha_3\,\alpha_3' \,\langle N, 6 \,|\, \tilde{s} \,|\, N+1, 6 \rangle \big)
\end{aligned}$$

$$\text{with} \quad C = \alpha_x \left(\frac{N_x + 1}{N+1} \right)^{1/2} \left(\Omega_x - N_x - \frac{N_x}{N} \langle n_d \rangle \right)^{1/2} \qquad (3.21)$$

$$\text{and} \quad \langle n_d \rangle = \langle N, 0_1^+ \,|\, \hat{n}_d \,|\, N, 0_1^+ \rangle. \qquad (3.22)$$

In the following this approach to calculate the matrix element via truncated wave functions will be called IBM-1 (PDS) in order to distinguish it from the full IBM-1 calculation using the complete wave functions. The calculation of the matrix elements of $\tilde{s}$ for $O(6)$ DS limit basis states can be simplified by expanding the $O(6)$ basis states in the $U(5)$ DS basis according to Eq. (2.24) using the transformation brackets (Eq. (2.25)). The basis states of the $U(5)$ DS limit can be written as

$$\begin{aligned}
|\, N,\, n_d,\, \nu,\, n_\Delta,\, L,\, M_L \,\rangle \;&=\; \frac{1}{\sqrt{n_s!}} \frac{1}{N_d} \hat{s}^{\dagger\, n_s} \left[\hat{d}^{\dagger\, n_d} \right]_{\nu, n_\Delta, L, M_L} |\, 0 \,\rangle \qquad (3.23) \\
&=\; |\, n_s \,\rangle \,|\, n_d,\, \nu,\, n_\Delta,\, L,\, M_L \,\rangle, \qquad (3.24)
\end{aligned}$$

where N_d is chosen such that $\langle N, n_d, \nu, n_\Delta, L, M_L \,|\, N, n_d, \nu, n_\Delta, L, M_L \rangle = 1$. The $U(5)$ basis states separate into normalized s-boson and d-boson wave functions. As $\tilde{s}$ cannot change the d-

boson part it only connects $U(5)$ basis states with identical d-boson wave functions. The matrix elements of $\tilde{s}$ for the s-boson wave function can be evaluated as:

$$\langle n_s' \mid \tilde{s} \mid n_s \rangle = \sqrt{n_s}\, \delta_{n_s', n_s - 1}. \tag{3.25}$$

The matrix elements computed in this work can be found in appendix D. In addition to the matrix elements, the expectation value of the d-boson number operator in the ground state $\langle n_d \rangle$ and the expansion coefficients α_1, α_2, α_3, and β have been computed numerically for the nuclei of interest (see Tab. 3.2). These nuclei are all in the $N = 82 - 126$ major shell, with $\Omega_\nu = 22$ (cf. Eqs. (2.41) and (2.42)).

Table 3.2.: Data needed to calculate the two-nucleon transfer intensities for some nuclei outside of the valley of low $\Delta\sigma$ (upper part of the table, down to the separation) and for nuclei inside the valley (lower part of the table, starting with ^{156}Gd). Note that the expansion coefficient α_1, α_2, and α_3, corresponding to the $O(6)$ DS limit basis states with $\sigma = N$ and $\tau = 0, 3, 6$ (cf. Eq. (3.18)), do not vary much for ground-state wave functions of nuclei in the valley of low $\Delta\sigma$. This highlights their common underlying structure. Expansion coefficients and the expectation value of $\hat{n}_d$ in the ground state ($\langle n_d \rangle$) have been calculated using ArbModel [94]. The ECQF structure parameters ξ and χ are taken from McCutchan et al. [50].

Nucleus	N	ξ	χ	N_ν	$\langle n_d \rangle$	0_1^+			
						α_1	α_2	α_3	β
^{150}Gd	9	0.30	-1.32	2	0.08	0.325	0.016	0.000	0.946
^{152}Gd	10	0.41	-1.32	3	2.97	0.382	0.060	0.003	0.922
^{154}Gd	11	0.59	-1.10	4	2.66	0.732	0.400	0.062	0.548
^{156}Gd	12	0.72	-0.86	5	4.58	0.776	0.576	0.137	0.217
^{158}Gd	13	0.75	-0.80	6	5.26	0.757	0.609	0.168	0.167
^{160}Gd	14	0.84	-0.53	7	5.99	0.762	0.616	0.174	0.098
^{162}Gd	15	0.98	-0.30	8	7.15	0.767	0.611	0.172	0.094
^{160}Dy	14	0.81	-0.49	6	5.55	0.779	0.578	0.142	0.197
^{162}Dy	15	0.92	-0.31	7	6.66	0.790	0.592	0.151	0.051
^{164}Dy	16	0.98	-0.26	8	7.58	0.772	0.608	0.171	0.071
^{164}Er	14	0.84	-0.37	7	5.55	0.808	0.546	0.117	0.188
^{166}Er	15	0.91	-0.31	8	6.57	0.794	0.587	0.147	0.058

A comparison of the calculated (p,t) ground state to ground state transfer intensities using the IBM-1 (PDS) approach to a full IBM-1 calculation and to experimental data is shown in Fig. 3.8. The data sets are normalized to the $0_1^+ \rightarrow 0_1^+$ transition intensity of ^{166}Er$(p,t)^{164}$Er, which is indicated by a black arrow. Note that this relative way to compare transfer intensities cancels the systematic underestimation of transfer intensities of the IBM (PDS) calculation, which is caused by neglecting the remainder (cf. Eq. (3.18)). If the relative IBM (PDS) prediction underestimates the experimental data for a specific relative transfer intensity, then the underestimation for this particular intensity is larger than for the transition that is used for the normalization. The experimental data consists of absolute cross section measurements and are

taken from Fleming et al. [99] for the Gd isotopes and from Maher, Kolata, and Miller [98] for Er and Dy isotopes. Outgoing tritons have been detected at different angles θ. In order to ensure meaningful comparisons the cross sections considered for this work are those that have been measured at $\theta = 25°$ (for Er and Dy isotopes) and $\theta = 30°$ (for Gd isotopes), both of which are close to the first maximum of the angular distribution.

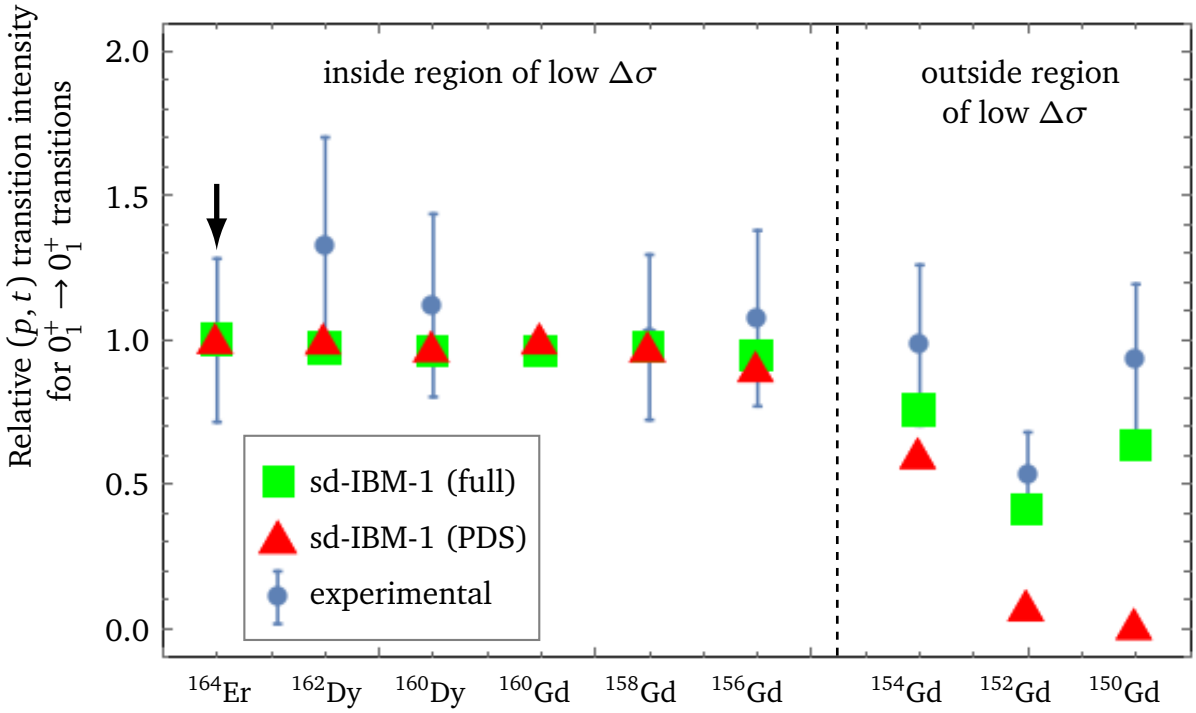

Figure 3.8.: Relative transition intensities of ground state to ground state transitions in (p,t) reactions between different nuclei inside and outside of the region of low $\Delta\sigma$. The predictions of the sd-IBM-1 (PDS) consider only the $\sigma = N$ components of the wave functions with $\tau = 0, 3, 6$ and are shown as red triangles, whereas the results for a full sd-IBM-1 calculation are shown as green squares, and the experimental data are shown as blue circles. The intensities have been normalized to the ^{166}Er$(p,t)^{164}$Er reaction (black arrow). The label on the x-axis indicates the final nucleus. Thus, a label ^{A}X has to be understood as $^{A+2}$X$(p,t)^{A}$X. Inside the valley of low $\Delta\sigma$ the sd-IBM-1 (PDS) approach can describe the experimental data, but outside this region it cannot. Experimental data are taken from Refs. [98, 99].

Inside the region of low σ fluctuations the IBM (PDS) and IBM (full) calculations are almost identical and reproduce the measured transfer intensities within experimental uncertainties. Considering that the IBM (PDS) description is achieved by only taking the $\sigma = \sigma_{max}$ components with $\tau = 0, 3, 6$ into account, this is a strong indication that those components are the dominant ones in the ground-state wave functions of the nuclei of Tab. 3.1. If this is the case, then the ground-state σ fluctuations have to be small for these nuclei. This is the first experimental indication that the ground-state band $O(6)$ PDS exists in real nuclei. Outside the region of low $\Delta\sigma$ the IBM (PDS) prediction of the transfer intensity drops rapidly as the $|\,\sigma = N, \tau = 0, 3, 6\rangle$ basis states become less important and the importance of the remainder ($\propto \beta$) increases for the wave function of the ground state. Consider, e.g., the Gd isotopic chain from ^{150}Gd to ^{162}Gd.

Inside the valley of low $\Delta\sigma$ the amplitude of the remainder term in the ground-state wave functions is relatively small ($\beta < 5\,\%$) and can be neglected to good approximation. This leads to a satisfactory description of the $0_1^+ \rightarrow 0_1^+$ intensities for the reactions ^{160}Gd$(p,t)^{158}$Gd and ^{158}Gd$(p,t)^{156}$Gd. For ^{162}Gd$(p,t)^{160}$Gd the prediction should also be reasonably accurate, as both nuclei are inside the valley of low $\Delta\sigma$, but no experimental data are available. Thus, the IBM (PDS) cross section for this case is a prediction ($\sigma(25°) \approx 0.58\,{}^{mb}/_{sr}$). Once the remainder becomes more important, even for just one of the nuclei involved, the prediction of the IBM (PDS) drops off compared to the experimental data (cf. ^{156}Gd$(p,t)^{154}$Gd in Fig. 3.8). Once the remainder starts to dominate the ground-state wave functions the theoretical IBM (PDS) predictions do drop off towards zero (e.g. for ^{152}Gd$(p,t)^{150}$Gd). This drop is not seen in the cross section data, which experimentally confirms the importance of the remainder for these nuclei. Note that this drop off does not happen if the remainder is explicitly taken into account, as shown by the results of the sd-IBM-1 (full) calculation.

The correspondence of experimental (p,t) data to theoretical IBM (PDS) predictions is largely based on numerical calculation of the expansion coefficients α_1, α_2, α_3, and β (cf. Eq. (3.20)). It is worth noting that, if both the initial and final nucleus are located exactly in the valley of low $\Delta\sigma$ (Eq. (3.16)), then two-nucleon transfer intensities can be evaluated analytically up to the coupling amplitudes α_x (cf. Eqs. (2.41) and (2.42)). This can be done by exploiting the close resemblance of the ground-state wave functions of these nuclei to the $L = 0$ projection of the intrinsic state of Eq. (3.9). For this state the expansion coefficients in the $O(6)$ DS limit basis are known analytically [81]. Using the $L = 0$ projection of this intrinsic state as an approximation to the ground-state wave function inside the region of low $\Delta\sigma$ yields

$$| N, 0_1^+ \rangle = K \sum_n \alpha_n \mid \sigma = N,\, \tau = 3n \rangle \tag{3.26}$$

$$\text{with} \quad \alpha_n = (-1)^n \sqrt{\frac{2n+1}{(N-3n)!(N+3n+3)!}}, \tag{3.27}$$

where K is a normalization constant. Employing this expansion for both ground states, the desired matrix elements $\langle N+1, 0_1^+ \mid \hat{s}^\dagger \mid N, 0_1^+ \rangle$ and $\langle N, 0_1^+ \mid \tilde{s} \mid N+1, 0_1^+ \rangle$ can be calculated using Eqs. (D.1) and (D.3). Additionally, the expectation value of the d-boson number operator in the ground state needs to be evaluated in order to calculate two-nucleon transfer intensities. This can be done analytically for the $O(6)$ basis states by exploiting $\hat{n}_d = \hat{N} - \hat{n}_s$. The operator $\hat{N}$ does not change the structure of the wave functions and connects only identical $O(6)$ basis states:

$$\langle \sigma, \tau \mid \hat{N} \mid \sigma' \tau' \rangle = N\, \delta_{\tau,\tau'}\, \delta_{\sigma,\sigma'}. \tag{3.28}$$

In order to calculate matrix elements of $\hat{n}_s$ one can use the reduction formula for tensor operators [100] to reduce the matrix element to those of $\hat{s}^\dagger$ and $\tilde{s}$:

$$\begin{aligned}
\langle \sigma = N, \tau \mid \hat{n}_s \mid \sigma = N, \tau \rangle &= \langle N, \tau \mid \hat{s}^\dagger \cdot \tilde{s} \mid N, \tau \rangle && (3.29)\\
&= \langle N, \tau \mid \hat{s}^\dagger \mid N-1, \tau \rangle \langle N-1, \tau \mid \tilde{s} \mid N, \tau \rangle \begin{Bmatrix} 0 & 0 & 0 \\ 0 & 0 & 0 \end{Bmatrix} && (3.30)\\
&= \frac{(N-\tau)(N+\tau+3)}{2(N+1)}, && (3.31)
\end{aligned}$$

where the curly brackets denote a Wigner 6-j symbol, which is identical to one in Eq. (3.30), and Eqs. (D.1) and (D.3) have been used. This yields

$$\langle \sigma = N,\, \tau \mid \hat{n}_d \mid \sigma = N,\, \tau \rangle = N - \frac{(N-\tau)(N+\tau+3)}{2\,(N+1)}, \tag{3.32}$$

which can be used in conjunction with Eq. (3.26) to calculate $\langle N,\, 0_1^+ \mid \hat{n}_d \mid N, 0_1^+ \rangle$. Together with Eqs. (3.26), (D.1), and (D.3) this allows an analytical calculation of the two-nucleon transfer intensities for ground state to ground state transitions from one nucleus inside the valley of low $\Delta\sigma$ to another nucleus in the valley up to the coupling amplitudes α_x. Writing this out explicitly for I_- yields

$$I_- = \mid \langle N,\, 0_1^+ \mid \hat{P}^{L=0}_{-x} \mid N+1, 0_1^+ \rangle \mid^2 \tag{3.33}$$

$$= \left| \sum_{n,m} C\, \alpha_n\, \alpha'_m \, \langle \sigma = N, \tau = 3\,n \mid \tilde{s} \mid \sigma = N+1,\, \tau = 3m \rangle \right|^2 \tag{3.34}$$

$$= \left| \sum_{n} C\, \alpha_n\, \alpha'_n \, \langle N,\, 3\,n \mid \tilde{s} \mid N+1,\, 3n \rangle \right|^2 \tag{3.35}$$

$$\begin{aligned} &= \alpha_x^2 \cdot \left| \sum_n \left[\left(\frac{N_x+1}{N+1} \right) \left(\Omega_x - 2N_x + \frac{N_x\,(N-3\,n)\,(N+3\,n+3)}{N\,(2N+1)} \right) \right.\right. \\ &\left. \left(\frac{2\,n+1}{(N-3\,n)!\,(N+3\,n+3)!} \right) \left(\frac{2\,n+1}{(N+1-3\,n)!\,(N+3\,n+4)!} \right) \right. \\ &\left.\left. \left(\frac{(N-3\,n+1)\,(N+3\,n+4)}{2\,(N+2)} \right) \right]^{1/2} \right|^2, \end{aligned} \tag{3.36}$$

where the selection rule $\Delta\tau = 0$ has been used (cf. Eq. (3.17)). The sum runs over all possible values n such that $3\,n \leq N$, which is a result of the requirement $\tau \leq \sigma$ (cf. Eq. (2.29)). This expression of the transfer intensity (Eq. (3.36)) depends only on the coupling amplitude α_x, the boson number N, the number of nucleons taking part in the transfer process N_x, and the pair degeneracy Ω_x. A similar expression for I_+ can be derived in the same manner. Relative transfer intensities can be calculated without any experimental input, if the nuclei of interest are all located within the same major shells. This requirement leads to a cancelation of the coupling amplitudes α_x in a relative analysis.

4 Summary and outlook

In this work quantum number fluctuations are used to show the existence of a region of approximate $O(6)$ symmetry for the ground-state band outside the $O(6)$ DS limit in the parameter space of the ECQF. Thus, an entire region of $O(6)$ PDS of type III has been identified. After the arc of regularity, which emerges through an underlying $SU(3)$ QDS, this is the second region inside the structure triangle of the ECQF showing an approximate symmetry. Using the overlap of ground-state wave functions, the wave functions in the region of low $\Delta\sigma$ are related to those of a Hamiltonian $\hat{H}_M$, which is tailor-made to produce an exactly $O(6)$ symmetric ground-state band. Through the similarity to $\hat{H}_M$ it is shown that the intrinsic state with $\beta \approx 1$ and $\gamma = 0$, from which the ground-state band of $\hat{H}_M$ is projected, represents a good approximation to the wave functions of the ground-state band of $\hat{H}_{ECQF}$ inside the region of low σ fluctuations. This constrains the energy surface $E(\beta, \gamma)$ and leads to an analytical parametrization

$$\xi(\chi) = \frac{1}{1 - \sqrt{\frac{1}{14}}\chi + \frac{1}{14}\chi^2} \tag{4.1}$$

of the $\Delta\sigma$ valley in the parameter space of $\hat{H}_{ECQF}$ for the limiting case of a large number of valence bosons ($N \to \infty$). This solution is already reasonably accurate for $N \geq 10$ and converges quickly with larger N.

Using the structure parameters determined by McCutchan et al. [50], nine nuclei in the rare earth region with approximate $O(6)$ PDS for the ground-state band are identified. These nuclei were previously considered to be $SU(3)$-like and their excitation energy spectra show almost perfect rotational spacing. It is shown that the rotational character of the ground-state band results from coherent mixing of different $SU(3)$ basis states (QDS). This is explained by the fact that the ground-state band corresponds to a single intrinsic state ($\beta \approx 1, \gamma = 0$). Thus, the $O(6)$ PDS leads to coherent mixing of basis states from the incompatible $SU(3)$ symmetry and results in an $SU(3)$ QDS. For the first time a link is established between the previously unrelated concepts of PDS and QDS. Even though this result is derived for the special case of the sd-IBM-1, this connection can also be exploited in other algebraic models and advance the understanding of dynamical systems in general.

Finally, the structure of the sd-IBM-1 wave functions inside the valley of low $\Delta\sigma$ is tested against experimental cross section data of (p, t) reactions. Taking into account only the dominant components of the ground-state wave functions, which correspond to the $O(6)$ basis states with $\sigma = N$ and $\tau = 0, 3, 6$, leads to a reasonable description of experimental data if both, the initial and final nucleus, are located inside the region of low $\Delta\sigma$. This strongly suggests that the $O(6)$ PDS does manifest in real nuclei and represents the first experimental evidence for the existence of this PDS. If one or both nuclei are located outside the valley of low $\Delta\sigma$ the IBM (PDS) predictions deviate significantly from the experimental data. Thus, two-nucleon transfer intensities provide a sensitive experimental signature to identify pairs of nuclei that both have approximate $O(6)$ symmetry for the ground state.

There are three main directions in which one can continue the theoretical research on the linkage of PDS and QDS. First, it is possible to focus on the particular $O(6)$ PDS to $SU(3)$ QDS connection established in this work. It would be of great interest to study it in the IBM-2, where

a distinction is made between proton and neutron bosons [37, 67]. The group structure of the IBM-2 arises from the $U(6)_\pi \bigotimes U(6)_\nu$ algebra and the corresponding chains of nested subalgebras and is much richer than that of the IBM-1. The Hamiltonian is also more complex. A good starting point could be a Hamiltonian containing d-boson energies, quadrupole-quadrupole interactions and a Majorana term. The projection formulas of Frank et al. [101] could be used to relate the IBM-2 Hamiltonian to $\hat{H}_{ECQF}$. Thus, one could identify parameters for the IBM-2 Hamiltonian that, projected onto its IBM-1 counterpart, correspond to the region of approximate $O(6)$ PDS. It can then be studied whether something similar to the IBM-1 $O(6)$ PDS manifests in $O(6)_\pi \bigotimes O(6)_\nu$ with its quantum numbers σ_π and σ_ν or in $O_{\pi+\nu}(6)$ with its quantum numbers (σ_1, σ_2).

Another possible avenue to explore is the investigation of already known PDS and QDS in the IBM-1. For example, the Alhassid-Whelan arc of regularity is caused by an underlying $SU(3)$ QDS. The question arises whether this QDS also gives rise to an associated PDS. From this work it is clear that, if there indeed is a PDS associated with the arc of regularity, then it cannot be an $O(6)$ ground-state band PDS, as the whole parameter space of the ECQF has been investigated in this thesis and no such PDS was found in the region of the arc of regularity. Finally, there is a possibility to apply the symmetry connection established in this work outside of the IBM and even outside of nuclear physics. The possibilities in this area are endless, but exploring them can only be done by the experts of the respective fields or at least in cooperation with them. A first possibility would be the vibron model [102], which is an algebraic model of molecular vibrations. This model is similar to the IBM, but the spectrum generating algebra is $U(4)$ instead of the $U(6)$ algebra used to describe nuclei in the IBM.

Apart from the discussed theoretical possibilities, there are things that could be done on the experimental side. First of all, the nuclei ^{160,162}Gd were identified as lying in the valley of low $\Delta\sigma$. This led to a prediction of the ^{162}Gd$(p,t)^{160}$Gd cross section for the ground state to ground state, which can be tested experimentally. Furthermore, it is possible to extend the analysis of Sec. 3.3 to additional two-nucleon transfer reaction, e.g. (t,p). At the same time it would be of interest to develop an experimental technique that allows the identification of a single nucleus inside the valley of low $\Delta\sigma$ independent from the neighboring nuclei. The current approach, using two-nucleon transfer reactions, can only be used to identify pairs of nuclei that are both likely to be located inside the region of low $\Delta\sigma$. This requires the identification of an observable that can be determined by measurements on a single nucleus and is sensitive to σ.

Part II.

High resolution electron scattering off ^{96}Zr

5 Motivation

The nucleus ^{96}Zr is located in the $A \approx 100$ mass region (see Fig. 5.1), which shows a variety of different nuclear structure phenomena. A well-known feature of this mass region is the shell closure at $N = 50$. In addition, there are two subshell closure at $Z = 40$ and $N = 56$. These subshell closures have profound effects on nuclear structure and attract considerable theoretical (see, e.g., Sieja et al. [42]) and experimental interest. For an overview of experimental investigations see Kanungo [103]. Experimental signatures of subshell closures are similar to those of regular shell closures, e.g. high-lying first excited 2^+_1 states and a drop in two neutron separation energies (see, e.g., Fig. 1 of Tondeur [104]). For the Zr isotopic chain the low-lying energy levels are shown in Fig. 5.2. The high excitation energies of the 2^+_1 state, in comparison to the excitation energy of the 2^+_1 state in neighboring isotopes, is evident for both ^{90}Zr and ^{96}Zr.

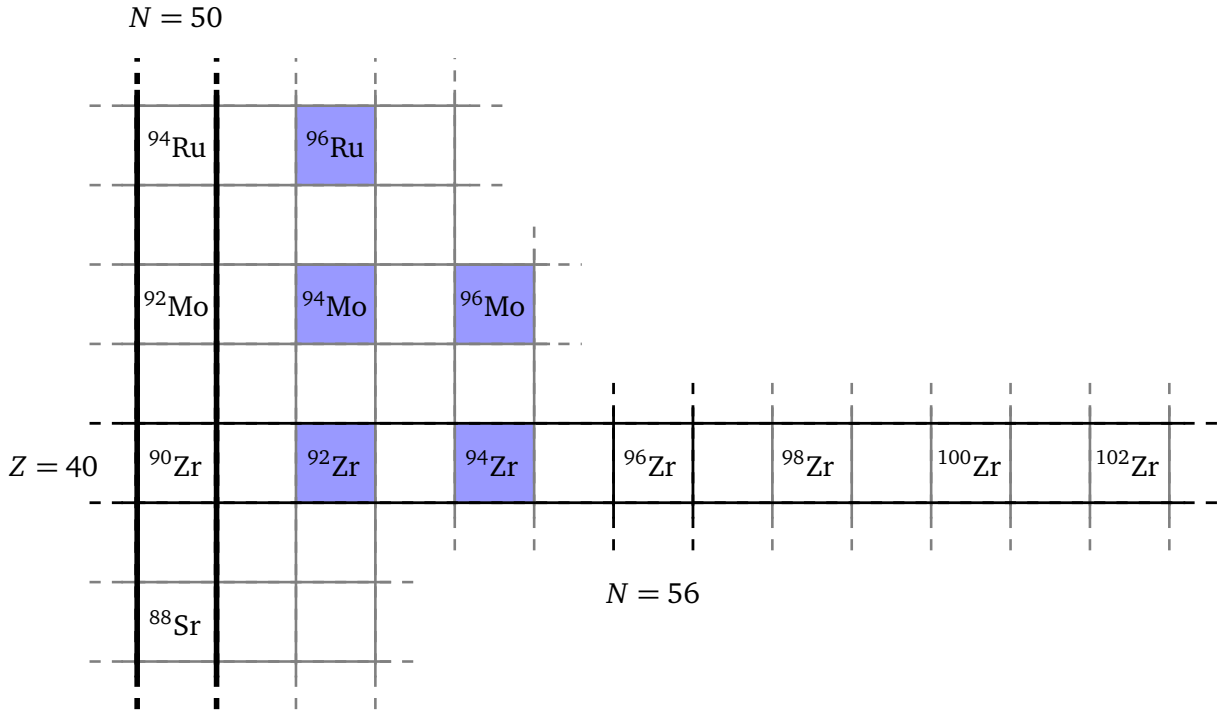

Figure 5.1.: Part of the $A \approx 100$ mass region with a focus on the Zr isotopes. Nuclei with known 2^+_{ms} states are shown with blue shading. The shell closure at $N = 50$ and the subshell closures at $Z = 40$ and $N = 56$ are indicated.

One of the hallmarks of the $A \approx 100$ mass region is a quick onset of deformation for neutron rich isotopes. First experimental evidence of deformed nuclei in this region was obtained by studying fission products of ^{252}Cf [105]. The nuclear structure theory interpretation of this region is a shape phase transition from spherical to deformed rotational structures (see, e.g., Refs. [43, 104, 106]). In the Zr isotopic chain this shape phase transition happens very quickly. For $^{90-98}$Zr the ground state is spherical, whereas it is rotational deformed in ^{100}Zr and for Zr isotopes with higher neutron numbers towards the middle of the $N = 50 - 82$ shell (see,

e.g., Mach et al. [107]). The typical evolution from spherical shapes at shell closure to more deformed rotational nuclei at midshell is interrupted by the subshell closure at $N = 56$ for ^{96}Zr. This subshell closure leads to an increase in the excitation energy of the 0^+_2 state in ^{96}Zr compared to ^{94}Zr. Adding neutrons above $N = 56$ leads to a rapid decrease in the excitation energy of the 0^+_2 state for ^{98}Zr (see Fig. 5.2). For ^{100}Zr the ground-state band shows almost exact rotational level spacing, which is an indication that the ground state is deformed. This implies a crossing of spherical and deformed 0^+ states around the ^{98}Zr-^{100}Zr region. In the stable even-even nuclei ^{90,92,94}Zr there is no evidence of low-lying deformed states.

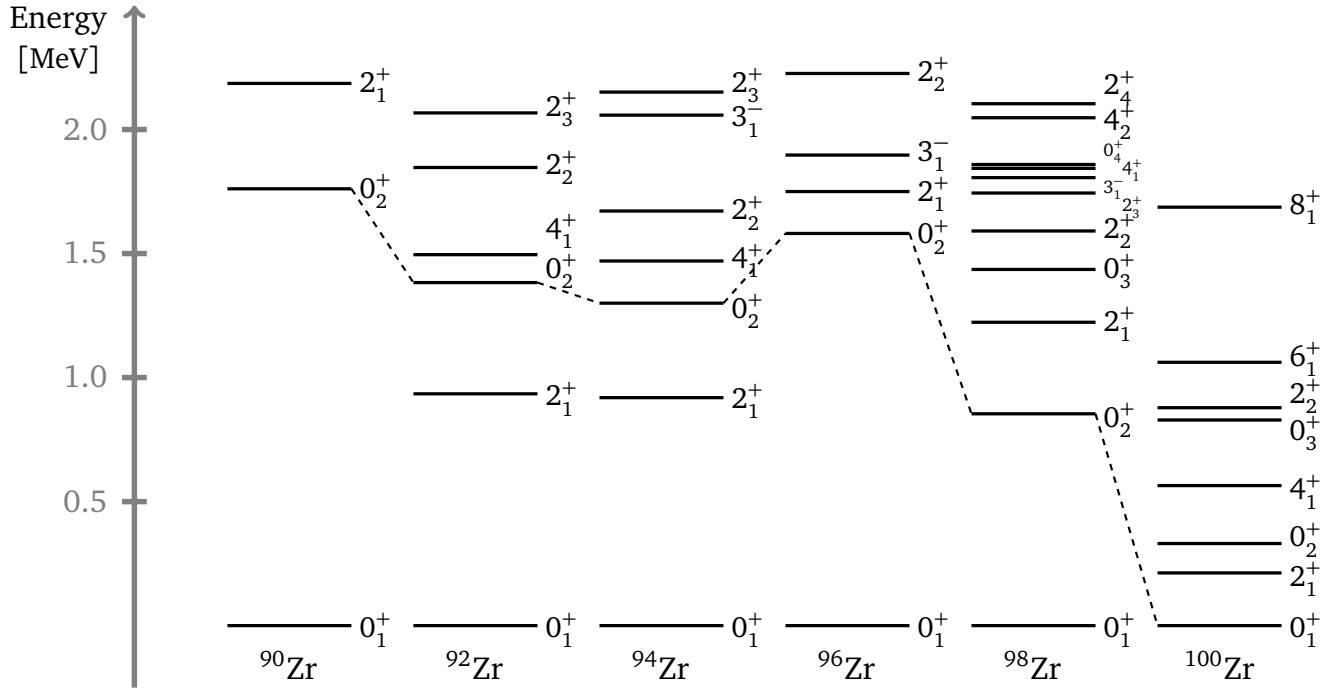

Figure 5.2.: Low-lying excited states of even-even Zr isotopes starting from the shell closure at $N = 50$ and extending into the neutron rich region ($N = 60$). The high-lying first excited state in ^{96}Zr, which is comparable in energy to that of ^{90}Zr, hints at the subshell closure at $N = 56$. Data taken from Ref. [97].

Another structural feature, which can be studied in the $A \approx 100$ mass region, are mixed-symmetry states. The defining characteristic of these states is their antisymmetry with respect to the proton-neutron degree of freedom [108]. This antisymmetry can be understood to arise via a mixture (cf. Sec. 6.1) of unperturbed proton and neutron excited states caused by the residual proton-neutron interaction. For the lowest-lying mixed-symmetry state, a one-quadrupole phonon 2^+ state [109], the situation can generally be written as:

$$|\,2^+_1\rangle = \alpha\,|\,2^+_\pi\rangle + \beta\,|\,2^+_\nu\rangle \qquad |\,2^+_{\mathrm{ms}}\rangle = \beta\,|\,2^+_\pi\rangle - \alpha\,|\,2^+_\nu\rangle, \tag{5.1}$$

where $|\,2^+_\pi\rangle$ $\left(|\,2^+_\nu\rangle\right)$ denotes the unperturbed proton (neutron) state and α and β are amplitudes with $\alpha^2 + \beta^2 = 1$. The symmetric admixture of proton and neutron components is the first excited 2^+ state, whereas the mixed-symmetric state 2^+_{ms} is located at higher excitation energies. The structure of both states, given by the amplitudes α and β, depends on the strength of the proton-neutron interaction and on the difference of the excitation energies of the unperturbed states. This makes mixed-symmetric states a valuable tool to study the proton-neutron

interaction. Experimentally, the 2^+_{ms} state can be identified by its decay properties. It shows a strong M1 decay to the fully-symmetric 2^+_1 state ($\approx 1\mu_N^2$) and weakly collective E2 transition (few W.u.) to the ground state [109]. Alternatively, an identification of 2^+_{ms} based on the difference of neutron and proton transition densities is possible in special cases [110]. Historically, the first examples of quadrupole mixed-symmetry states have been found in the $A \approx 140$ mass region [111], but the nucleus ^{94}Mo soon emerged as the textbook example for this mode of excitation [112]. From this point onward, the $A \approx 100$ mass region has been systematically investigated with different experimental techniques in search of mixed-symmetric states. This led to the identification of quadrupole mixed-symmetry states in ^{96}Ru [113], ^{96}Mo [114], and also in ^{92}Zr [115] and ^{94}Zr [116] (see also Fig. 5.1). The effects of the double subshell closure in ^{96}Zr on the formation of mixed-symmetry states have not yet been investigated. No candidate for the 2^+_{ms} has been identified in this nucleus.

The available experimental data on ^{96}Zr is sparse. Its low-lying excitation energy spectrum is shown in Fig. 5.3. The large $B(\mathrm{E3}; 3^-_1 \rightarrow 0^+_1) = 57(4)$ W.u. value for the excitation of the 3^-_1 state has led to increased experimental and theoretical interest (see, e.g., Refs. [117, 118]) in this state. Apart from the $B(\mathrm{E3}; 3^-_1 \rightarrow 0^+_1)$ and $B(\mathrm{E2}; 2^+_1 \rightarrow 0^+_1)$ values the only transition strength known with meaningful errors is the E0 transition strength to the first excited state (0^+_2). In order to clarify the low-lying nuclear structure additional data on the decays of the 2^+_2 state are of utmost importance. The branching ratios and multipole mixing ratios for its various decay possibilities were determined by a mix of $(n, n'\gamma)$ [119] and β-decay experiments [120]. The experimental data resulted in the interpretation of the 0^+_2 state as a 4-particle-4-hole (4p-4h) deformed intruder configuration, akin to the established deformed structures in the neutron-rich Zr isotopes ^{98,100,102}Zr, by the authors of Refs. [119, 120]. Based on measured $\log(ft)$ values a deformation of $\beta_2 \approx 0.2$ for the deformed structure and a weak mixing with the spherical structure of the ground state is deduced [120]. The 2^+_2 state is interpreted as an excitation of the deformed 0^+_2 state. This implies a large $B(\mathrm{E2}; 2^+_2 \rightarrow 0^+_2)$ value, which has not yet been confirmed experimentally. At this point, an electron scattering experiment can considerably contribute to further elucidate the nuclear structure of ^{96}Zr. By making use of the known multipole mixing ratios and branching ratios for the decays of the 2^+_2 state it is possible to determine the transition strengths of these decays by measuring the $B(\mathrm{E2}; 0^+_1 \rightarrow 2^+_2)$ value. This value has already been measured in low-energy $^{96}\mathrm{Zr}(p, p')$ and low- and medium-energy $^{96}\mathrm{Zr}(d, d')$ experiments by Hofer et al. [121]. The deduced $B(\mathrm{E2}; 0^+_1 \rightarrow 2^+_2)$ values range from 0.05 W.u. to 0.23 W.u.. However, the extraction of transition strengths from the proton and deuteron scattering data was done in a modified coupled channel analysis, which depends strongly on input parameters and model assumptions. By measuring the $B(\mathrm{E2}; 0^+_1 \rightarrow 2^+_2)$ value in electron scattering (cf. Fig. 5.3) it will be possible to determine the decay strengths of the 2^+_2 state in a robust way. The subsequent determination of the decay strengths of the 2^+_2 state will allow a verification (or falsification) of the 4p-4h interpretation by Mach et al. [120]. In addition, knowledge of the absolute transition strengths will help investigating the question whether or not the 2^+_2 state could be a suitable candidate for, or at least could carry some strength of, the lowest quadrupole collective mixed-symmetric state. Note that an interpretation in terms of a mixed-symmetric excitation and in terms of a 4p-4h intruder configuration is mutually incompatible.

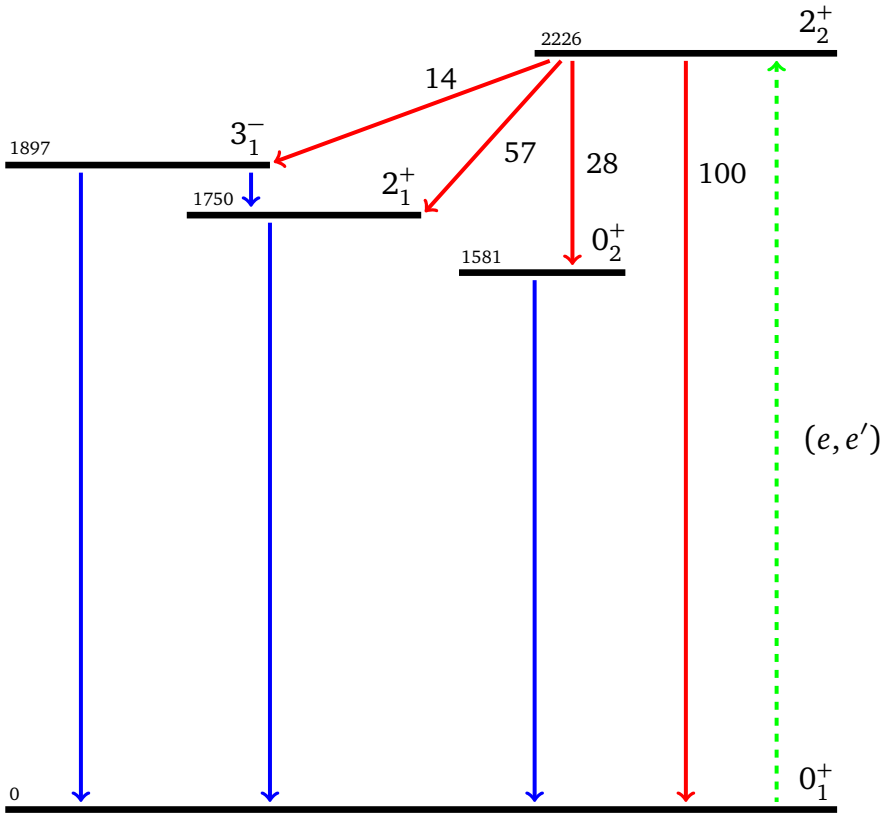

Figure 5.3.: Low energy part of the ^{96}Zr level scheme, where the energy (in keV), spin and parity for each state is shown. Blue arrows indicate transitions with known strength (cf. Ref. [97]). The red arrows represent transitions with unknown (or unreliably known) strength and the known branching ratios are displayed next to each arrow. Determination of these unknown transition strengths is the goal of the electron scattering experiment (green dashed arrow) conducted in this work.

6 Theoretical background

This chapter describes the theoretical background necessary for the interpretation of the ^{96}Zr(e,e') experiment. In section 6.1 the mixing of quantum states by a residual interaction is considered in very general terms. The evolution of nuclear shells, especially the configuration-dependent (type II) shell evolution within a nucleus, is discussed in section 6.2.

6.1 Mixing of quantum states

The description of quantum systems is tedious and mathematically complex. It can be simplified by choosing a basis that consists of eigenfunctions of the full Hamilton operator of the problem. If this is possible the Hamiltonian is diagonal in this basis and computations are simple. In practice it is often necessary to separate the Hamilton operator $\hat{H}$ in a part $\hat{H}_0$ that possesses some favorable characteristics (e.g. a certain symmetry) and a residual part $\hat{H}_1$ that is treated as a perturbation to $\hat{H}_0$. It is particularly convenient to choose $\hat{H}_0$ in such a way that a basis consisting of its eigenfunctions can be constructed. Then $\hat{H}_0$ is diagonal in the basis but $\hat{H} = \hat{H}_0 + \hat{H}_1$ is not. The eigenstates of $\hat{H}$ are a linear combination of the basis states. The following discussion of the special case of two-state mixing is based on the presentation in Casten [122].

The simplest example of quantum mechanical mixing is a two-state system as shown in Figure 6.1. The eigenfunctions of $\hat{H}_0$ are ϕ_1 and ϕ_2 and are chosen as basis. These functions satisfy $\hat{H}_0\,\phi_i = E_i\,\phi_i$ with $i \in \{1,2\}$ which defines the energies E_1 and E_2 in the absence of any perturbation. Once the full hamiltonian $\hat{H} = \hat{H}_0 + \hat{H}_1$ is considered, the off diagonal matrix elements $V = |\langle\phi_1 \mid \hat{H} \mid \phi_2\rangle| = |\langle\phi_2 \mid \hat{H} \mid \phi_1\rangle|$ do not vanish. This causes the eigenfunctions $\Psi_{1,2}$ of $\hat{H}$ to be a mixture of the basis states $\phi_{1,2}$ and the energies $\tilde{E}_{1,2}$ to be shifted from the energies $E_{1,2}$ of the unperturbed case. Solving for the eigenvalues of $\hat{H}$ results in the energies of the mixed states

$$\tilde{E}_{1,2}(R,E_1,E_2) = \frac{1}{2}(E_1+E_2) \pm \frac{E_2-E_1}{2}\sqrt{1+\frac{4}{R^2}} = \frac{1}{2}(E_1+E_2) \pm \Delta E, \tag{6.1}$$

with $R = {}^{(E_2-E_1)}/_{V}$. The mixing leads to a coherent wave function $\Psi_1 = \alpha\phi_1 + \beta\phi_2$ with energy $\tilde{E}_1 = E_1 - \Delta E$ whereas the non-coherent wave function $\Psi_2 = -\beta\phi_1 + \alpha\phi_2$ is shifted upward in energy by ΔE. This general feature of two-state mixing persists in multi-state mixing. The wave function of the lowest-lying state is coherent.

The perturbed wave functions $\Psi_{1,2}$ can be calculated as the eigenvectors of $\hat{H}$. This leads to an equation for the smaller amplitude in terms of R

$$\beta(R) = \frac{1}{\sqrt{1+\left(\frac{R}{2}+\sqrt{1+\frac{R^2}{4}}\right)^2}}. \tag{6.2}$$

The larger amplitude can be calculated using the normalization condition $\alpha^2 + \beta^2 = 1$. The described mixing of quantum states is experimentally accessible via transition rates. Consider two low-lying, pure states ϕ_a and ϕ_b with known transition matrix elements $M_a = \langle 0_1^+ \mid \hat{O} \mid \phi_a\rangle$

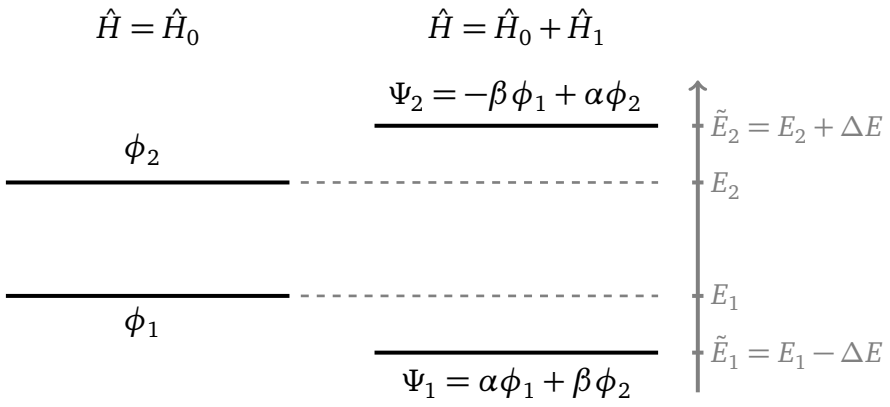

Figure 6.1.: Effect of two-state mixing on excitation energies and wavefunctions. If the hamilton operator $\hat{H}$ of a two-state quantum system is diagonal in the chosen basis the eigenfunctions of $\hat{H}$ are the pure basis states $\{\phi_1, \phi_2\}$ (left hand side). If there is a perturbation $\hat{H}_1$ to the unperturbed hamiltonian $\hat{H}_0$ the eigenfunctions are a linear combination of the basis states. One state will be coherent and lower in energy by an amount ΔE while the wave function of the second state will be higher in energy by ΔE and its wave function is not coherent (right hand side).

and $M_b = \langle 0_1^+ \mid \hat{O} \mid \phi_b \rangle$ to the 0_1^+ ground state through an arbitrary operator $\hat{O}$ as shown on the left hand side of Figure 6.2. If these states are mixed by a residual interaction the situation illustrated on the right hand side of Figure 6.2 occurs. The new transition matrix elements for the mixed states Ψ_a and Ψ_b to the ground state are then given by

$$\tilde{M}_a = \langle 0_1^+ \mid \hat{O} \mid \Psi_a \rangle = \alpha M_a + \beta M_b, \text{ and} \tag{6.3}$$

$$\tilde{M}_b = \langle 0_1^+ \mid \hat{O} \mid \Psi_b \rangle = -\beta M_a + \alpha M_b. \tag{6.4}$$

The matrix elements of the transition of the mixed states to the ground state are a linear combination of the matrix elements of the unmixed states to the ground state. This case is particularly interesting if one of the matrix elements vanishes exactly in the unperturbed case. A measurement of such a forbidden transition will prove the existence of symmetry-violating terms in the hamiltonian, which lead to mixing of the states and consequently finite matrix elements for the forbidden transitions. For example consider the $O(6)$ dynamical symmetry of the Interacting Boson Model. If a nucleus conforms exactly to this symmetry its $E0$ transitions should obey the $\Delta\sigma = 2$, and $\Delta\tau = 0$ selection rules and its $E2$ transitions should obey the $\Delta\sigma = 0$, and $\Delta\tau = \pm 1$ selection rules. Transitions that violate these selection rules should vanish exactly. If the symmetry is not exact then the hamiltonian has a part that is not diagonal in the $O(6)$ basis. The experimentally observed states will be mixtures of $O(6)$ basis states and finite transition matrix elements for the forbidden transitions arise according to Eq. (6.4). The nucleus ^{196}Pt has been identified as close to the $O(6)$ dynamical symmetry [88]. Excitation energies suggest that the 0_3^+ state of ^{196}Pt corresponds closely to the lowest lying $\sigma = N - 2$ state of the $O(6)$ symmetry. Its decay should obey the selection rules mentioned above if the $O(6)$ symmetry is exact for ^{196}Pt. If, however, the $O(6)$ symmetry is not exact in ^{196}Pt the forbidden transitions should be finite. Measuring the forbidden transitions allows the extraction of a mixing matrix element V_{mix} and a quantification of the goodness of $O(6)$ symmetry in this nucleus. The decay of the 0_3^+ state of ^{196}Pt has recently been investigated [73, 74].

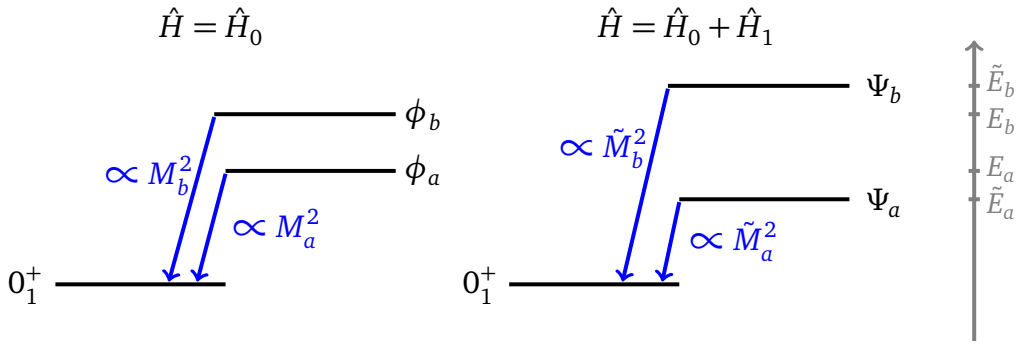

Figure 6.2.: Influence of two-state mixing on transition rates. The left hand side shows two basis states ϕ_a and ϕ_b that are also eigenfunctions of the hamiltonian $\hat{H}_0$. The ground-state transitions are proportional to the squared matrix elements. If a hamilton operator $\hat{H}_1$ is added the eigenfunctions of the resulting hamiltonian $\hat{H}$ will be linear combinations of ϕ_a and ϕ_b in general (right hand side). The ground-state transition matrix elements $\tilde{M}_b$ and $\tilde{M}_a$ of the mixed states Ψ_a and Ψ_b depend on both of the initial matrix elements as shown by Eq. (6.3) and (6.4).

6.2 Type II shell evolution

Since its development the shell model [61, 62] has played a major role in the interpretation of nuclear structure. Its most notable success is the correct description of the conventional magic numbers for protons and neutrons $(2, 8, 20, 28, 50, 82, 126)$, which results from the underlying shell structure. A shell-model calculation starts from a closed inert core of fully occupied shells and a set of orbitals (the model space) outside this core. The core is chosen such that the nuclei outside the core can be considered, approximately, to move independently in a one-body average potential created by the inert core. The results of a shell-model calculation, as far as excitation energies are concerned, are single particle energies (SPE) ϵ_j for all orbitals j of the model space and a set of occupation numbers $\{n_j\}$ for a given configuration (e.g. for the 0_1^+ state). The occupation number n_j is the average number of nucleons occupying the orbital j for the considered configuration. The excitation energy of such a configuration is then given by

$$E(\{n_j\}) = \sum_j \epsilon_j n_j. \tag{6.5}$$

The experimental study of nuclei far away from stability ($Z \not\approx N$) has revealed new phenomena, among them the appearance of new magic numbers (see, e.g., Steppenbeck et al. [123, 124]) and the parity inversion of the ^{11}Be ground-state [125, 126], which cannot be explained by the conventional shell model with a central potential and a one-body spin-orbit term. A change of the shell structure, that is to say a change of the underlying single particle energies of the shell model, is required to explain these phenomena. This change can only be brought about by residual forces between particles outside of the inert core. The shell evolution due to nuclear forces is briefly discussed in this chapter following the pioneering works by Otsuka and coworkers [127–129].

In order to obtain an improved description of nuclear structure beyond the independent particle model residual interactions of nucleons outside the inert core of the shell-model calculation

have to be taken into account. For any two-body interaction V this can be accomplished by taking its $j-j$ coupled two-body matrix elements $\langle jj'J \mid V \mid jj'J\rangle$ into account. Provided the interaction is central, it can be written as a sum over multipole orders. In the following the effects of the monopole part of the interaction will be considered.

The average monopole matrix element $v^m_{j,j'}$ is given by

$$v^m_{j,j'} = \frac{\sum_J (2J+1)\cdot\langle jj'J \mid V \mid jj'J\rangle}{\sum_J 2J+1}, \tag{6.6}$$

where J runs over all possible values for the angular momentum coupling of a nucleon in orbit j and a nucleon in orbit j'. Each matrix element is weighted by the number of possible ways to couple j and j' to J. The denominator is the total number of possible two-particle states. Taking the monopole interaction into account the energy of a given nuclear configuration with occupation numbers $\{n_j\}$ can be written as

$$E\left(\{n_j\}\right) = \sum_j \epsilon_j\, n_j + \sum_j \frac{1}{2}\, n_j\left(n_j - 1\right) v^m_{j,j} + \sum_{j\neq j'} n_j\, n_{j'}\, v^m_{j,j'}, \tag{6.7}$$

where the second term represents the monopole interaction of nucleons in identical orbitals, whereas the third term represents the monopole interaction of nucleons in different orbits. From the last term of this equation it can be deduced (by differentiation) that the SPE of orbit j changes with the number of particles present in orbital j'. The magnitude of this shift is

$$\Delta\epsilon_j = v^m_{j,j'}\, n_{j'}, \tag{6.8}$$

which is proportional to the number of nucleons in orbital $n_{j'}$. It is possible that shell gaps between two orbital j_1 and j_2 are modified by the filling of orbital j'. As the orbital j' is filled the orbitals j_1 and j_2 are, in general, shifted by unequal amounts. The relative shift depends on the difference of the respective monopole matrix elements $v^m_{j_1,j'}$ and $v^m_{j_2,j'}$.

Up to this point the interaction V has not been specified and the above formalism is valid for a general two-body interaction. However, it was shown that the tensor force, originating mainly from one-pion exchange, plays an important role for the evolution of nuclear shells [129]. It can be written as

$$V_T = (\vec{\tau}_1\cdot\vec{\tau}_2)\left([\vec{s}_1\,\vec{s}_2]^{(2)}\cdot Y^{(2)}\right) f(r), \tag{6.9}$$

where $\tau_{1,2}$ denotes the isospin of the respective nucleon, Y is a spherical harmonic, and $f(r)$ is a function of the relative distance. With this parametrization the monopole matrix elements (Eq. (6.6)) can be evaluated. The resulting energy shifts depend on the coupling of the angular momentum and spin in the respective orbitals and can also be understood intuitively (by comparison with the deuteron) [129]. Let $j_> = l+s$ and $j_< = l-s$, then one finds in general an attraction for $j_>$-$j'_<$ interactions and repulsion for $j_>$-$j'_>$ and $j_<$-$j'_<$ interactions (see Fig. 6.3(a)). Thus, as the number of nucleons changes, the tensor monopole interaction changes the ESPEs (type I shell evolution), as displayed in Fig. 6.3(b) for proton ESPEs of Sb isotopes. Note that the filling of a $j'_>$ ($j'_<$) orbital for protons (neutrons) leads to a decrease (an increase) in spin-orbit splitting for neutrons (protons).

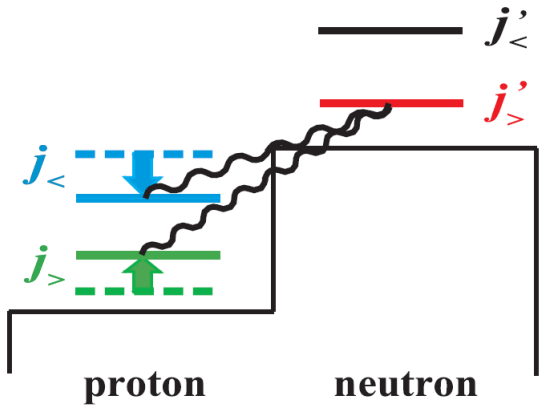

(a) Schematic illustration of the change in proton ESPEs by neutrons in an $j'_>$ orbital caused by the monopole tensor force. Reprinted figure with permission from Otsuka et al. [129]. Copyright 2005 by the American Physical Society.

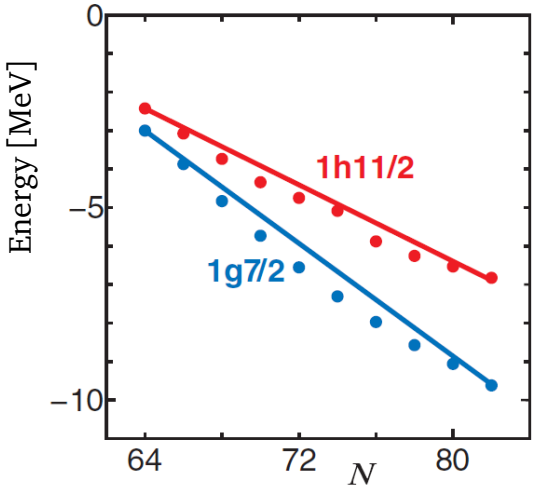

(b) Change in proton ESPEs for the Sb isotopic chain as a function of neutron number N. The solid lines represent a shell-model calculation with monopole interaction [129] whereas the dots represent experimental data [130]. Reprinted figure with permission from Otsuka et al. [129]. Copyright 2005 by the American Physical Society.

Figure 6.3.: General effect of the monopole tensor force on SPEs. The general mechanism changing proton SPEs is shown on the left and an example of the evolution of proton ESPE with changing number of neutrons is shown on the right. The effect is similar for protons and neutrons exchanged.

The shell evolution is not constrained to the cases of changing nucleon numbers discussed above. Excited nuclear states often feature occupation numbers different from those of the ground state. The nucleons in the excited state occupy different orbitals which leads to corresponding changes of the residual interactions. Consider, e.g., the excitation of protons from a $j_<$ to a $j_>$ orbital, as illustrated in Fig. 6.4. More protons in $j_>$ reduces the spin-orbit splitting for neutrons by lowering ESPEs of $j_<$ orbitals and increasing ESPEs of $j_>$ orbitals. Additionally, the holes left behind in the $j_<$ proton shell enhance this effect further. Protons in a $j_<$ orbital have the effect of increasing the spin-orbit splitting for neutrons. By removing protons from $j_<$ this effect is weakened, thus, proton holes in a $j_<$ orbital reduce the spin-orbit splitting for neutrons. If neutron occupation numbers change as a result of the changed proton occupation numbers, then the neutrons are now more likely to occupy the lowered $j_<$ orbitals. Additional neutrons occupying $j_<$, in turn, favor protons in $j_>$ orbitals. Thus, a self-enhancing effect is produced, which can help stabilize the excitation. This configuration-dependent shell evolution has been discussed for Ni isotopes in [44] and is called type II shell evolution.

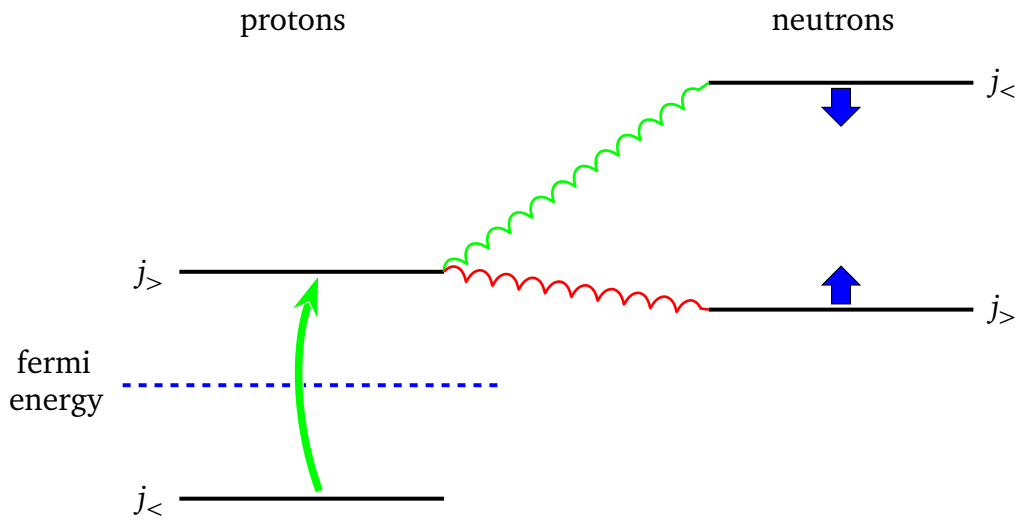

Figure 6.4.: Configuration-dependent (type II) shell evolution. Protons are excited from a $j_<$ orbital below the fermi surface to a $j_>$ orbital above the fermi surface. This reduces the spin-orbit splitting for the neutrons via the attractive (green line) and repulsive (red line) tensor monopole interaction. The effect is enhanced by the holes left behind in the proton $j_<$ orbital.

7 Electron scattering formalism

In this chapter the underlying theory of electron scattering experiments at low-momentum transfer is introduced. First, the general approach to obtain transition strengths from electron scattering data, including commonly used approximations, are discussed in section 7.1. Then, in section 7.2, the relative analysis of transition strengths, which is the method used in this work, is described.

7.1 Inelastic electron scattering

Electron scattering is a widely used technique to study properties of the nucleus and its constituents. The electron is an especially good probe to investigate the nuclear force, because the interaction between the electron and the nucleus is purely electromagnetic and is well described by quantum electrodynamics (see, e.g., Peskin and Schroeder [131] for an introduction). This means that, unlike for hadronic probes, the interaction does not contribute additional uncertainties to the analysis of scattering processes. There exists a great variety of introductions to this topic. For the purpose of compiling this overview Refs. [132–136] have been used. The relevant formulas are taken from Refs. [134, 135], but a different notation is used.

The process of inelastic scattering is schematically illustrated in Fig. 7.1, which also shows the notation used. An incoming electron with initial energy E_0 and initial momentum $\vec{p}_0$ scatters

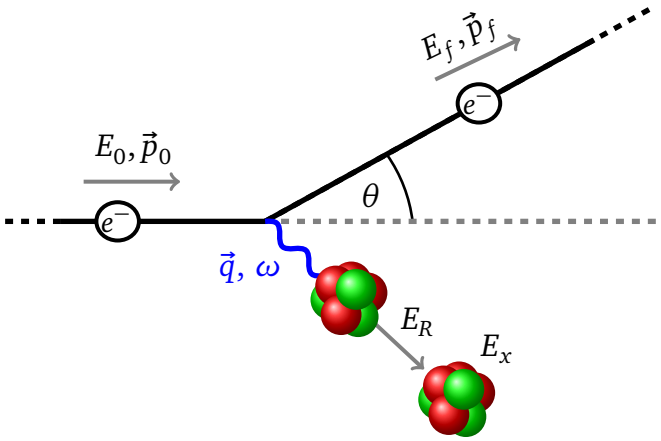

Figure 7.1.: This figure shows a schematic illustration of the process of inelastic electron scattering at low-momentum transfer. Only the first order of the process, one-photon exchange, is shown.

off a nucleus which has nuclear charge Z and is initially at rest. For light nuclei ($Z\,\alpha \ll 1$ with α being the fine structure constant) the scattering process is, to good approximation, described by the exchange of a single virtual photon. The photon transfers momentum $\vec{q}$ and energy ω from the electron to the nucleus. The electron is scattered at an angle θ and its final energy E_f is measured in a spectrometer. After the scattering process the nucleus has the recoil energy

E_R and may be at an excited state of energy E_X. From energy and momentum conservation it follows that

$$E_0 = E_f + E_X + E_R, \tag{7.1}$$

$$\vec{q} = \vec{p}_0 - \vec{p}_f, \text{ and} \tag{7.2}$$

$$q = |\vec{q}| = \frac{1}{\hbar c}\sqrt{\frac{4E_0\,(E_0 - E_X)\sin^2\frac{\theta}{2} + E_X}{1 + \frac{2E_0}{Mc^2}\sin^2\frac{\theta}{2}}}. \tag{7.3}$$

In order to deduce the excitation energy from the measured final energy of the electron the initial beam energy and the recoil energy have to be known. For the experimental conditions in the ^{96}Zr(e,e') experiment ($q \leq 0.6$ fm^{-1}, $E_X \leq 2.5$ MeV) the recoil energy can be calculated to

$$E_R = \sqrt{(Mc^2 + E_X)^2} - \left(Mc^2 + E_X\right) \approx 4 \cdot 10^{-8}\ \text{MeV} \tag{7.4}$$

where M is the mass of ^{96}Zr [137]. Thus, the recoil energy can be neglected. Assuming the beam energy is known, a measurement of E_f is sufficient to deduce E_X. The cross section for elastic scattering of electrons off a point charge is given by the Mott cross section:

$$\left(\frac{d\sigma}{d\Omega}\right)_{Mott} = \frac{Ze^2}{2E_0}\frac{\cos^2(\theta/2)}{\sin^4(\theta/2)} \tag{7.5}$$

with the elementary charge e. Atomic nuclei are not point-like, but have a spatially extended charge distribution. Its effects on the scattering are incorporated in the form factor $F(q)$ connecting the experimental cross section to the Mott cross section

$$\left(\frac{d\sigma}{d\Omega}\right)_{exp} = |F(q)|^2 \cdot \left(\frac{d\sigma}{d\Omega}\right)_{Mott}. \tag{7.6}$$

If the elastic form factor has been experimentally determined over an extended range of momentum transfers, information about the charge distribution of the nucleus can be obtained via the Fourier transform of $F(q)$. Eq. (7.6) is also used to investigate inelastic scattering. In general the cross section for inelastic scattering depends on the wave functions $\Psi_{i,f}$ of the initial and final states of the nucleus. The cross section can be written as

$$\left(\frac{d\sigma}{d\Omega}\right) = \frac{E_0 E_f}{4\pi^2(\hbar c)^2}\left(\frac{|\vec{p}_f|}{|\vec{p}_0|}\right)\left(\frac{2J_f + 1}{2J_i + 1}\right) f_{rec}\,|\langle\Psi_f|\hat{H}_{int}|\Psi_i\rangle|^2 \tag{7.7}$$

where $J_{i,f}$ denote initial and final spin of the nucleus, respectively, $\hat{H}_{int}$ describes the interaction of the electron with the nucleus, and the recoil factor is given by

$$f_{rec} = \left(1 + \frac{2E_0}{Mc^2}\sin^2\theta\right)^{-1}. \tag{7.8}$$

It is useful to remember that, apart from energy and momentum, the electromagnetic interaction also conserves angular momentum and parity π, which leads to a set of conditions for

electromagnetic transitions. The multipolarity λ of the transition is constrained by the spins $J_{i,f}$ of the initial and final states

$$|J_i - J_f| \leq \lambda \leq |J_i + J_f|, \tag{7.9}$$

and the parity π of the transition is determined by the parities $\pi_{i,f}$ of initial and final states

$$\pi = \pi_i \cdot \pi_f = (-1)^{\lambda+1} \quad \text{for magnetic transitions,} \tag{7.10}$$

$$\pi = \pi_i \cdot \pi_f = (-1)^{\lambda} \quad \text{for electric transitions.} \tag{7.11}$$

It immediately follows that for excitations from the 0_1^+ ground state of ^{96}Zr there is always just a single possible transition type, e.g. the excitation of 2^+ states is pure $E2$ whereas the excitation of the prominent 3_1^- state is pure $E3$. There are different ways how experimental data can be related to the cross section and the matrix element of Eq. (7.7). These methods revolve around assumptions about the wave functions of the nuclear states and around a multipole expansion of the interaction. A widely used method to solve the scattering problem is the Plane Wave Born Approximation (PWBA). It makes three critical assumptions in order to achieve the desired simplification. First, as already discussed above, the interaction is assumed to be one-photon exchange only. Furthermore, the incoming and outgoing electron is described by a plane wave solution of the Dirac equation. This assumption is valid for nuclei satisfying $Z\,\alpha \ll 1$, such that the electric field of the nucleus does not distort the electron wave function significantly. Finally, relativistic effects of the recoiling nucleus are neglected. This is a valid assumption if the energy of the incident electron is small compared to the rest mass of a nucleon, which holds for the experimental conditions of the ^{96}Zr(e,e') experiment analysed in this thesis. With these assumptions the cross section can be decomposed into a sum of electric and magnetic multipole components

$$\left(\frac{d\sigma}{d\Omega}\right)_{PWBA} = \sum_{\lambda}\left(\frac{d\sigma}{d\Omega}\right)_{E\,\lambda} + \sum_{\lambda}\left(\frac{d\sigma}{d\Omega}\right)_{M\,\lambda} \tag{7.12}$$

where the electric and magnetic cross sections can be written explicitly as:

$$\left(\frac{d\sigma}{d\Omega}\right)_{E\,\lambda} = \left(\frac{Z\,\mathrm{e}^2}{E_0}\right)^2 f_{rec}\left[V_L \cdot |F(C\,\lambda, q)|^2 + V_T \cdot |F(E\,\lambda, q)|^2\right], \tag{7.13}$$

$$\left(\frac{d\sigma}{d\Omega}\right)_{M\,\lambda} = \left(\frac{Z\,\mathrm{e}^2}{E_0}\right)^2 f_{rec}\left[V_T \cdot |F(M\,\lambda, q)|^2\right]. \tag{7.14}$$

The kinematical factors V_L and V_T are functions of the beam energy, the excitation energy, and the scattering angle and can be computed as

$$V_L = V_L(E_0, E_X, \theta) = \frac{1+\cos\theta}{2(x-\cos\theta)^2} \quad \text{and} \tag{7.15}$$

$$V_T = V_T(E_0, E_X, \theta) = \frac{2x+1-\cos\theta}{4(x-\cos\theta)(1-\cos\theta)} \tag{7.16}$$

$$\text{with } x = 1 + \frac{E_X^2}{2E_0(E_0 - E_X)}. \tag{7.17}$$

The form factors $F(X\,\lambda, q)$ with $X \in \{\mathrm{C}, \mathrm{E}, \mathrm{M}\}$ are connected to the matrix elements of the corresponding transition operators $\hat{T}^{X\,\lambda}$ by

$$F(E\,\lambda, q) = \frac{q^{\lambda}}{\sqrt{2J_i+1}\cdot(2\lambda+1)!!}\sqrt{\frac{\lambda+1}{\lambda}}\,\langle\Psi_f \mid \hat{T}^{E\,\lambda} \mid \Psi_i\rangle, \tag{7.18}$$

$$F(M\,\lambda, q) = \frac{q^{\lambda}}{\sqrt{2J_i+1}\cdot(2\lambda+1)!!}\sqrt{\frac{\lambda+1}{\lambda}}\,\langle\Psi_f \mid \hat{T}^{M\,\lambda} \mid \Psi_i\rangle, \text{ and} \tag{7.19}$$

$$F(C\,\lambda, q) = \frac{q^{\lambda}}{\sqrt{2J_i+1}\cdot(2\lambda+1)!!}\,\langle\Psi_f \mid \hat{T}^{C\,\lambda} \mid \Psi_i\rangle. \tag{7.20}$$

Thus, in PWBA an analytical relation between measured cross section and the magnitude of the matrix element of the transition operator exists. The reduced transition probabilities, which are commonly used to compare experimental data, can be written as

$$B(X\,\lambda, q) = \frac{1}{2J_i+1}\,|\langle\Psi_f \mid \hat{T}^{X\,\lambda} \mid \Psi_i\rangle|^2. \tag{7.21}$$

In order to compare these data to experiments using real photons it is necessary to measure at different values of the momentum transfer q and extrapolate to the photon point $k = {}^{E_X}/_{\hbar c}$. For heavy nuclei the PWBA is not a good approximation, because the electric field of the nucleus and the atomic electrons influence the electron wave functions. When the electron approaches the nucleus it is accelerated towards it, while it will be decelerated once it passed the nucleus. The resulting wave functions are no longer plane waves, but distorted ones. They can still be calculated as solutions to the Dirac equation by explicitly using the ground-state charge distribution of the nucleus as an input parameter. This method is called Distorted Wave Born Approximation (DWBA).

7.2 Relative analysis of transition strengths

Extraction of transition strengths from electron scattering data is usually model-dependent, as described in the section above. For heavy nuclei the DWBA formalism requires theoretical transition densities as additional input data. Recently a new method to extract transition strengths from scattering data for heavy nuclei, which is independent of the explicit input of transition densities, has been developed [138, 139] and is used in this work. The main idea is to extract transition strength of one excited state to the ground state relative to that of another excited state to the ground state using PWBA. In general PWBA is not valid for heavy nuclei and DWBA has to be used. The difference in theoretical cross sections using PWBA and DWBA is given by the Coulomb correction factors

$$f_c = f_c(E_0, E_X, \theta) = \left[\frac{({}^{d\sigma}/_{d\Omega})_{DWBA}}{({}^{d\sigma}/_{d\Omega})_{PWBA}}\right]_{\text{theo}}. \tag{7.22}$$

Writing the DWBA cross section for electric transitions in terms of the PWBA cross section of Eq. (7.13) yields

$$\left(\frac{d\sigma}{d\Omega}\right)_{E\,\lambda} = f_c\left(\frac{d\sigma}{d\Omega}\right)_{E\,\lambda,\,\mathrm{PWBA}} \tag{7.23}$$

$$= \left(\frac{Z\,\mathrm{e}^2}{E_0}\right)^2 f_{rec}\,f_c\left[V_L\cdot|F(C\,\lambda, q)|^2 + V_T\cdot|F(E\,\lambda, q)|^2\right]. \tag{7.24}$$

A similar relation for the magnetic cross section is omitted here, because it has no relevance to the electron scattering experiment conducted in this thesis. For the 2_1^+ and 2_2^+ states of ^{96}Zr the correction factors have been calculated in QRPA [140] and are shown in Fig. 7.2(a). The large deviation of the absolute Coulomb correction factors from unity validates the notion that, in general, Coulomb effects are important in heavy nuclei and PWBA is not a valid way to analyze these nuclei. However, for the whole momentum transfer range of interest the ratio of Coulomb correction factors of the 2_1^+ and 2_2^+ states of ^{96}Zr is unity to better than 1 % (see Fig. 7.2(b)). By using Eq. (7.22) it follows that the ratio of DWBA cross sections, which is experimentally accessible, equals approximately the ratio of PWBA cross sections. Thus, the formalism of the PWBA (cf. Sec. 7.1) can be used for relative analysis of experimental data in heavy nuclei.

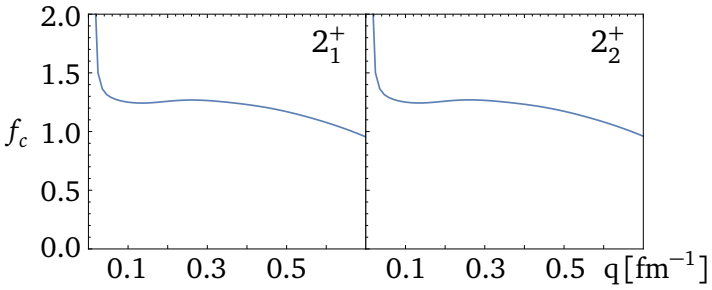

(a) Absolute Coulomb correction factors show a large deviation from unity, especially at low momentum transfer.

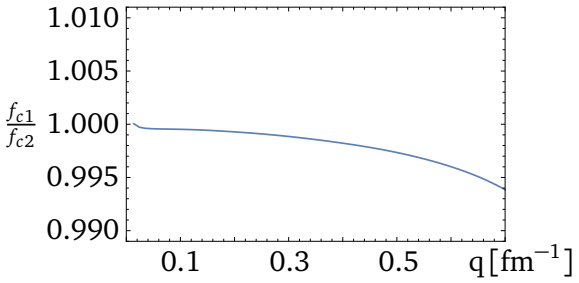

(b) The ratio of Coulomb correction factors is approximately unity (to better than 1 %).

Figure 7.2.: This figure shows the Coulomb correction factors f_{c1} and f_{c2}, as defined in Eq. (7.22), for the 2_1^+- and 2_2^+-states of ^{96}Zr respectively. Calculations were performed using QRPA [140]. The momentum transfer range shown contains the momentum transfers at which the ^{96}Zr(e,e') experiment was conducted.

Using Siegert's theorem [136, 141]

$$B(E\,\lambda,q) = \frac{k^2}{q^2}\,B(C\,\lambda,q) \tag{7.25}$$

and Eqs. (7.18) to (7.21) the electric cross section, as given by Eq. (7.13), can be rewritten as

$$\left(\frac{d\sigma}{d\Omega}\right)_{E\,\lambda} = \left[\left(\frac{Z\,e^2}{E_0}\right)^2 \frac{f_{rec}\cdot q^{2\,\lambda}}{(2\,\lambda+1)!!}\cdot V_L\left(\frac{\lambda}{\lambda+1}+\frac{k^2\,V_T}{q^2\,V_L}\right)\right]\cdot B(C\,\lambda,q) \tag{7.26}$$

$$= f_{kin}\cdot B(C\,\lambda,q) \tag{7.27}$$

which is a form better suited to extract the transition strength from experimental data. In the limit of low momentum transfer the transition strength can be expanded in powers of q [133, 136] as

$$\sqrt{B(C\,\lambda,q)} = \sqrt{B(C\,\lambda,0)}\cdot\left(1-\frac{q^2\,R_{tr}^2}{2\,(2\,\lambda+3)}+\frac{q^4\,R_{tr}^4}{8\,(2\,\lambda+3)\,(2\,\lambda+5)}-\ldots\right) \tag{7.28}$$

where the transition radius R_{tr} is given by

$$R_{tr}^{n} = \frac{\left\langle r^{\lambda+n} \right\rangle_{tr}}{\langle r^{\lambda} \rangle} = \frac{\int \rho_{tr}^{\lambda}\, r^{\lambda+n}\, d^3r}{\int \rho_{tr}^{\lambda}\, r^{n}\, d^3r} \tag{7.29}$$

using the transition densities ρ_{tr}. For the excitation energy range studied in this thesis it holds that $k = {}^{E_X}/_{\hbar c} \ll 1$ and thus $\sqrt{B(C\,\lambda, 0)} \approx \sqrt{B(C\,\lambda, k)}$. Finally, the cross section of an excitation i is proportional to the number of electrons A_i experimentally counted at the appropriate energy in a scattering experiment:

$$\left(\frac{d\,\sigma}{d\,\Omega}\right) = \frac{1}{N_e \cdot \Delta\Omega \cdot \rho_t} \cdot A_i \propto A_i. \tag{7.30}$$

The constant of proportionality depends on the solid angle of the detector $\Delta\Omega$, the total number of electrons N_e that bombarded the target during the measurement, and the areal density ρ_t of the target in nuclei per cm^2. Because excitations of 2^+ states from a 0^+ ground state, as is the case in the experiment in this thesis, have pure E2 character, this relation (Eq. (7.30)) can be combined with Eq. (7.27) and Eq. (7.28) for the 2_2^+ and 2_1^+ states of ^{96}Zr. Taking the ratio of the resulting equations yields the desired relation of experimental peak areas to transition strengths:

$$R_F(q)\sqrt{\frac{A_2}{A_1}} \approx \sqrt{\frac{B(\mathrm{E2}; 2_2^+ \to 0_1^+, k_2)}{B(\mathrm{E2}; 2_1^+ \to 0_1^+, k_1)}} \cdot \left(\frac{1 - \frac{q_2^2}{14}(R_{tr,1} + \Delta R)^2 + \frac{q_2^4}{504}(R_{tr,1} + \Delta R)^4}{1 - \frac{q_1^2}{14}(R_{tr,1})^2 + \frac{q_1^4}{504}(R_{tr,1})^4} \right). \tag{7.31}$$

In the derivation of this equation the ratio of Coulomb correction factors has been neglected (cf. Fig. 7.2(b)) and the ratio of kinematical factors is contained in the factor

$$R_F(q) = \sqrt{\frac{f_{kin,2}}{f_{kin,1}}}. \tag{7.32}$$

The difference in transition radii ΔR is defined by $R_{tr,2} = R_{tr,1} + \Delta R$, and in the expansion of $\sqrt{B(C\,\lambda, q)}$ (Eq. (7.28)) only terms up to order q^4 have been kept.

8 ^{96}Zr(e,e') experiment at the S-DALINAC

This chapter outlines the experimental setup at the Institut für Kernphysik at the TU Darmstadt. The accelerator and the available experimental facilities are briefly discussed in section 8.1. In section 8.2 the Lintott spectrometer, which has been used for this work, and its modes of operation are described in detail. Details of the ^{96}Zr(e,e') experiment and collected experimental data are presented in section 8.3.

8.1 S-DALINAC and experimental facilities

The electron beam for this experiment was provided by the **S**uperconducting-**DA**rmstadt-Electron-**LIN**ear-**AC**celerator (S-DALINAC) [142] which replaced the previously used **DA**rmstadt-**LI**near-**AC**celerator (DALINAC) [143] in 1991. Figure 8.1 shows the layout of the S-DALINAC and the experimental facilities. For the production of the electron beam a thermionic gun and a polarized source [144] exist. For the ^{96}Zr(e,e') experiment the thermionic gun was used. The necessary time structure for acceleration is imprinted on the beam by a chopper and by prebunchers, which are placed in the normal conducting part of the accelerator. Then, the electrons enter the superconducting part and are accelerated up to 10 MeV in the injector module. After the injector photon scattering and photodissociation experiments with bremsstrahlung can be done using the **D**armstadt **H**igh-**I**ntensity **P**hoton **S**etup (DHIPS) [145]. Alternatively, the beam can be injected into the main accelerator where it can be recirculated up to two times. Thus the beam can pass the 40 MeV acceleration structure up to three times. This allows final electron energies of up to 130 MeV at a current of 20 μA and a relative energy resolution $^{\Delta E}/_{E} \approx 6 \cdot 10^{-4}$ in isochronous operation. Utilizing a non-isochronous recirculation scheme the energy resolution can be improved to $^{\Delta E}/_{E} \approx 1.2 \cdot 10^{-4}$ [146]. A third recirculation beamline is planned [147] and will enable operation of the S-DALINAC as an energy recovery linear accelerator. After the main accelerator the beam can be extracted to the different experimental setups in the experimental hall. One of these setups is the low-energy photon tagger NEPTUN which is used for experiments with energy-tagged photons [148, 149]. Another setup is the QCLAM magnetic spectrometer [150–153]. It has large solid angle coverage ($\Delta\Omega \approx 35$ msr) and can be used for (e,e') as well as $(e,e'x)$ experiments. A silicon detector ball [154] enables experiments with charged particles, e.g. $(e,e'p)$ or $(e,e'\alpha)$, whereas a LaBr detector ball [155] is presently setup to detect photons in $(e,e'\gamma)$ experiments. Additionally, 180° scattering experiments can be performed at the QCLAM spectrometer using the chicane beamline and a separation magnet inside the scattering chamber [156]. The last major experimental setup, the Lintott spectrometer, was used in this work and will be discussed in detail in chapter 8.2. It is a magnetic spectrometer with a dispersion matching beam line, which is able to achieve a much better energy resolution than the QCLAM spectrometer (which does not have a dispersion matching beam line). However, the solid angle coverage ($\Delta\Omega \approx 6$ msr) is much smaller at the Lintott spectrometer.

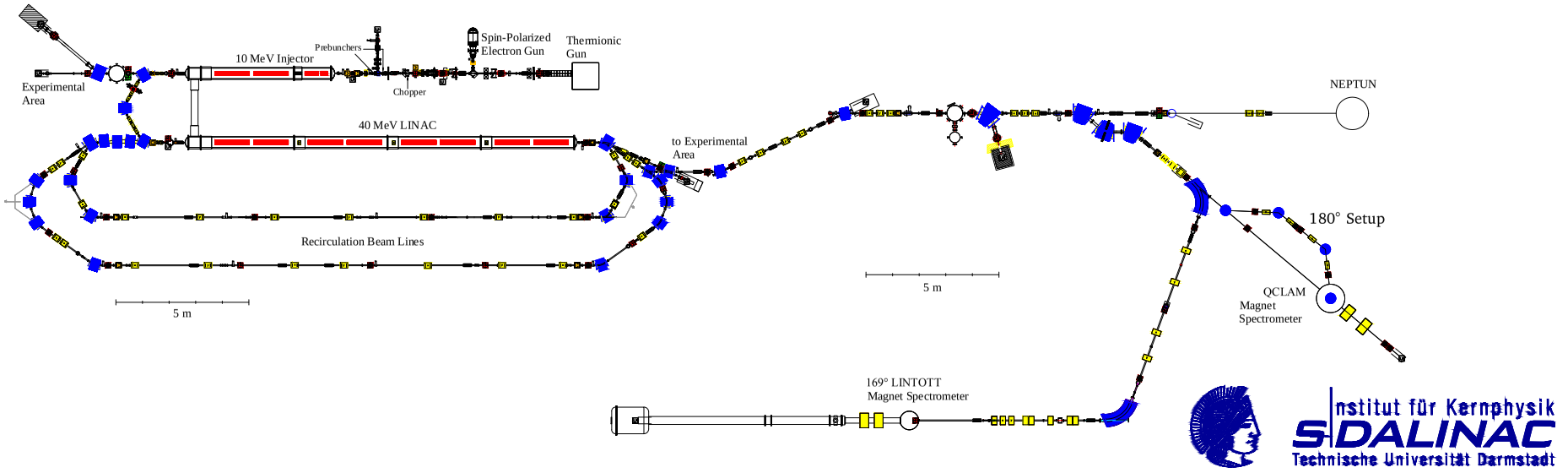

Figure 8.1.: Superconducting-Darmstadt-Linear-Accelerator and experimental facilities at the Institut für Kernphysik at the TU Darmstadt. Accelerating structures are shown in red, dipole magnets in blue and quadrupole magnets in yellow. The S-DALINAC can provide electron beams of up to 130 MeV energy at a current of 20 μA (design values) and a relative energy resolution $\Delta E/E \approx 1.2 \cdot 10^{-4}$. The experiment in this work was performed using the Lintott spectrometer. Figure taken and slightly modified from Refs. [157, 158].

8.2 High resolution electron scattering at the Lintott spectrometer

The electron beam of the S-DALINAC can be used to study structural properties of atomic nuclei. In order to obtain the desired information one observes electrons scattered from a target enriched in the isotope of interest. Magnetic spectrometers are used to make the energy of the electrons after the interaction accessible. The scattered electrons are bent in the magnetic field B of a dipole magnet. The bending radius r depends on the momentum p of the electrons, the field of the magnet B and the charge of the electron q:

$$r = \frac{p}{qB} \qquad \text{for } \vec{p} \perp \vec{B} \tag{8.1}$$

The electrons are then detected in a position sensitive detector system. Together with the information of the primary beam energy E_0 the energy lost by the scattered electrons due to the interaction with the target can be determined, since for highly relativistic electrons $E^2 \approx p^2 c^2$. High precision electron scattering experiments pose additional problems to the experimentalist. The target thickness is limited by energy straggling which leads to low count rates. Additionally, the energy spread of the incoming electron beam must be sufficiently small. A small energy spread can be imposed on the electron beam by momentum analyzing slits, but the intensity drops if parts of the beam are blocked. Finally, the detector system has to have a sufficient resolution and its efficiency should be as high as possible in order to minimize the required beam time per measurement. The Lintott spectrometer (Figure 8.2(a)) has been designed with these requirements in mind and is used to perform high resolution (e, e')-experiments with relative energy resolution $\Delta E/E$ of the order 10^{-4}.

8.2.1 Magic angle spectrometer

The first pillar to achieve a good resolution is the design of the beam optics of the spectrometer. The Lintott spectrometer is a double focusing (radial and axial) magic-angle spectrometer. The principles were developed by Ikegami [160] and later utilized in the construction of the Lintott spectrometer [161]. The deflection angle of the spectrometer τ is chosen to be $\tau = \pi\sqrt{7}/3 \approx 169.7°$. This so called "“magic angle"” allows for proper focusing irrespective of the object distance to the magnet. Additionally, it shifts the focal plane away from the dipole magnet, which makes it easier to construct suitable position sensitive detectors. Furthermore, the focal plane is tilted 35° against the plane of the reference particle in order to compensate second-order aberrations.

8.2.2 Focal plane detector system

The second pillar of a high resolution spectrometer is the detector system. At the Lintott (see Figure 8.2) it is placed directly at the focal plane and uses silicon strip detectors. Four individual detector segments with 96 strips each are used to cover the focal plane, because a single crystal of the required length could not be manufactured. Between the four modules insensitive areas of 10.5 strips ($\approx$ 7 mm) exist caused by the necessary use of guard rings. The silicon detectors have a thickness of 500 μm leading to an effective energy of $250 - 270$ keV deposited in the material at typical electron energies of $20 - 100$ MeV [159]. In order to reach the best possible

(a) Photo of the Lintott spectrometer. The beam enters from the left hand side (1) and hits the target inside the scattering chamber (2). A fraction of the scattered electrons enter the spectrometer. The dipole magnet (3) bends the electrons onto different trajectories corresponding to their momentum. The position sensitive silicon strip detector setup (4) is used to detect the electrons.

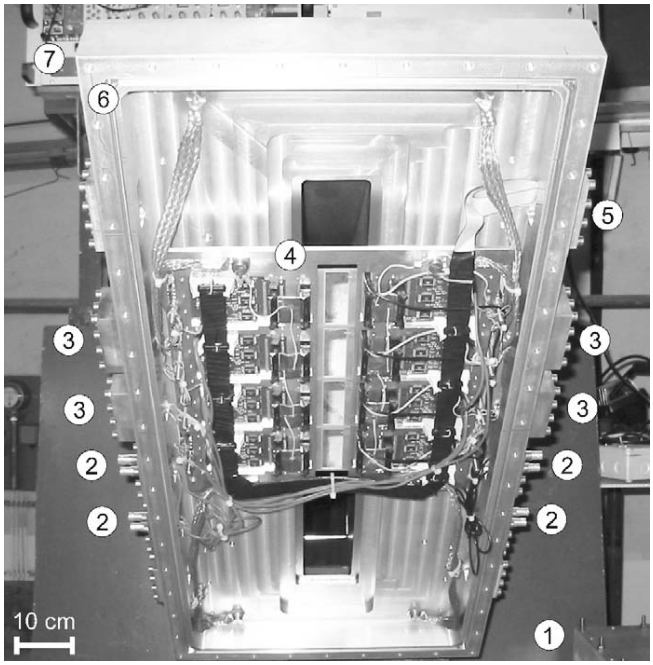

(b) Focal plane detector system of the spectrometer. The components shown are iron yoke of the dipole magnet (1), vacuum connections of bias signals to preamplifiers (2), vacuum connections of the analog signal of the preamplifiers (3), silicon strip detector unit (4), vacuum connections of preamplifiers supply voltage and control signals (5), detector case (6), and read-out electronics and high voltage adaptor (7). Figure taken from Lenhardt et al. [159].

Figure 8.2.: The Lintott spectrometer (left) with its focal plane detector system (right).

resolution the detectors are mounted inside the spectrometer vacuum chamber. Behind the silicon detectors is an exit window covered with 50 μm Mylar foil which allows the installation of trigger detectors outside the spectrometer vacuum chamber. During the ^{96}Zr(e,e') measurement a plastic scintillator was used as a trigger detector, which helps suppressing background events. In addition, it is possible to use a Cherenkov counter in coincidence with the other detectors. The entire system can be operated at count rates up to 30 kHz with an efficiency close to 100 %. It allows measurements with a relative energy resolution of $\Delta E/E \approx 1 \cdot 10^{-4}$. Additional information about the detector system can be found in Lenhardt et al. [159].

8.2.3 Energy loss mode

In conventional operation of the S-DALINAC the beam is focused on the target (see left-hand side of Figure 8.3). Electrons with the same momentum p are then focused at the same point of the focal plane irrespective of their entrance angle into the spectrometer magnet. However, the initial momentum spread of the beam is a major problem in this mode of operation. If

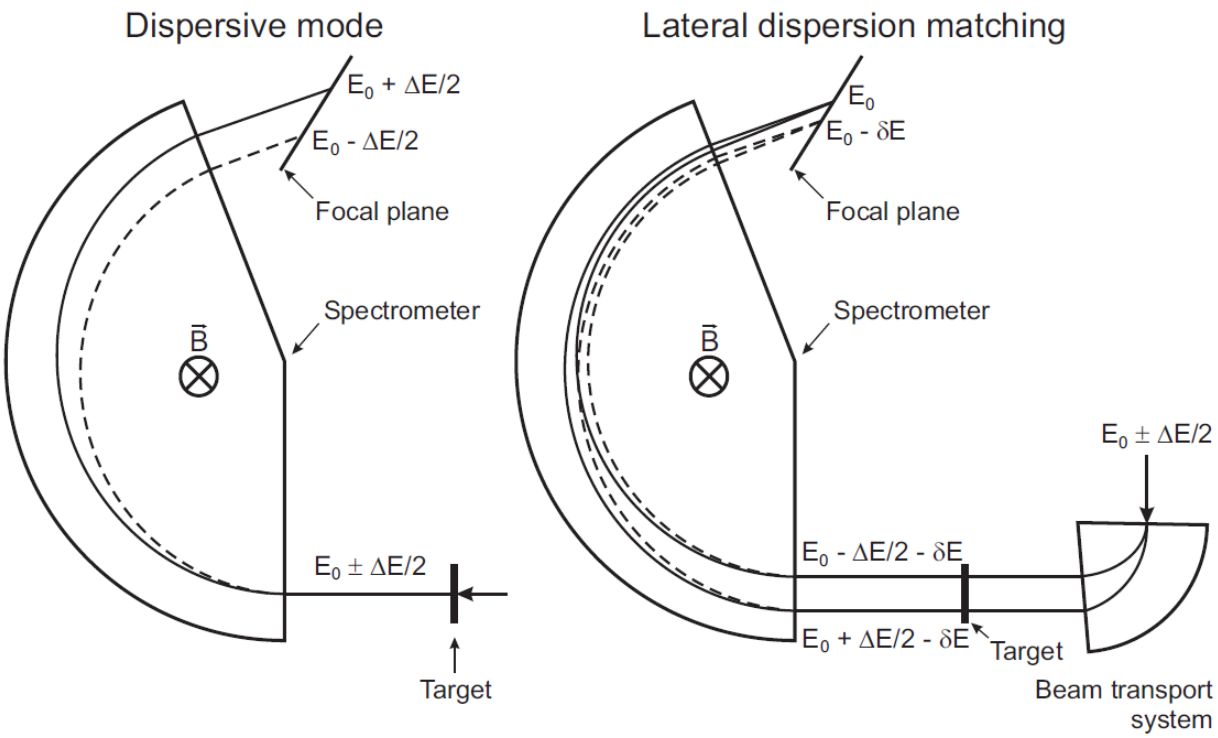

Figure 8.3.: Dispersive mode (left) and energy loss mode (right) of the Lintott spectrometer. In conventional operation the initial energy spread of the beam ΔE influences the position of the electrons at the focal plane. This imposes a lower limit on the resolution. In energy loss mode this dependence is removed by matching the dispersion of the beam transport system to the dispersion of the spectrometer. Figure taken from Burda [162].

the resolution of the electron beam is worse than the achievable resolution of the spectrometer it will act as an lower bound for the experimental resolution (typically $^{\Delta E}/_{E} \approx 1 \cdot 10^{-4}$). This dependence on the energy resolution of the beam can be removed using the dispersion matching technique also called "energy loss" mode [161]. The basic principle is to artificially introduce dispersion into the beam transport system, which matches the dispersion of the spectrometer (see right-hand side of Figure 8.3). This makes the position on the focal plane only dependent on the energy loss in the target. The system as a whole is non-dispersive with regard to the initial beam spread. In energy loss mode an energy resolution of $^{\Delta E}/_{E} \approx 1 \cdot 10^{-4}$ is possible. Operation in this way will increase the beam spot size on the target. This imposes a new limit on the maximum tolerable energy spread ΔE of the beam. If the energy spread of the beam crosses a certain threshold it is no longer possible to fit the entire beam spot on the target. This causes the intensity to decline and makes absolute cross section measurements, which are based on collected charge in the Faraday cup, impossible. The limit imposed on the energy spread of the beam depends on the dispersion on the spectrometer ($3.76\,^{\mathrm{cm}}/_{\%}$), the diameter of the target, and on the beam energy. For an initial beam energy of 70 MeV and a target diameter of 2 cm this results in the constraint $\Delta E \leq 370$ keV. This condition should always be satisfied during operation.

Table 8.1.: Isotopic composition of the zirconium target used for the electron scattering experiment.

Target thickness $10\ ^{mg}/_{cm^2}$	
Isotope	Enrichment
^{90}Zr	9.2 %
^{91}Zr	2.0 %
^{92}Zr	27.2 %
^{94}Zr	4.3 %
^{96}Zr	57.36 %

8.3 Experimental details

The electron scattering experiment on ^{96}Zr was conducted during different experimental beam times in December 2014, March 2015, and June 2015 at the Lintott spectrometer using the electron beam provided by the S-DALINAC. Data were taken at 81°, 93°, 117°, and 141°. The measurement at 117° was conducted with beam energy of 69 MeV while the other measurements were performed at 43 MeV beam energy. Intensities of the beam ranged from 500 nA to 2.5 μA and were limited by the dead time of the data acquisition. The target used was a 2×3 cm^2 self-supporting zirconium foil of thickness 10 $^{mg}/_{cm^2}$. It was enriched in ^{96}Zr to 57.36 %. The target composition is displayed in Table 8.1. The presence of contaminants in the target means that energy resolution is of crucial importance for this experiment. Especially the presence of ^{90}Zr is detrimental for this experiment, because the 2_1^+ state at 2.186 MeV is very close to the 2_2^+ state of ^{96}Zr at 2.226 MeV. The different recoil energies of the two isotopes intensify this problem. For 69 MeV an energy resolution of 21.3 keV full width half maximum (FWHM) was achieved while it ranged from 12.3 keV FWHM (93°) to 17.5 keV FWHM (141°) for the measurements at 43 MeV. The collected experimental data can be seen in Figure 8.4. Several measurements of ^{208}Pb(e,e'), ^{12}C(e,e'), and ^{196}Pt(e,e') at sufficiently high excitation energies (about 20−35 MeV) to be above the giant dipole resonance of the respective nucleus were taken to calibrate the relative efficiency of the detectors. Unfortunately, no efficiency calibration could be conducted at 69 MeV due to technical difficulties at the accelerator.

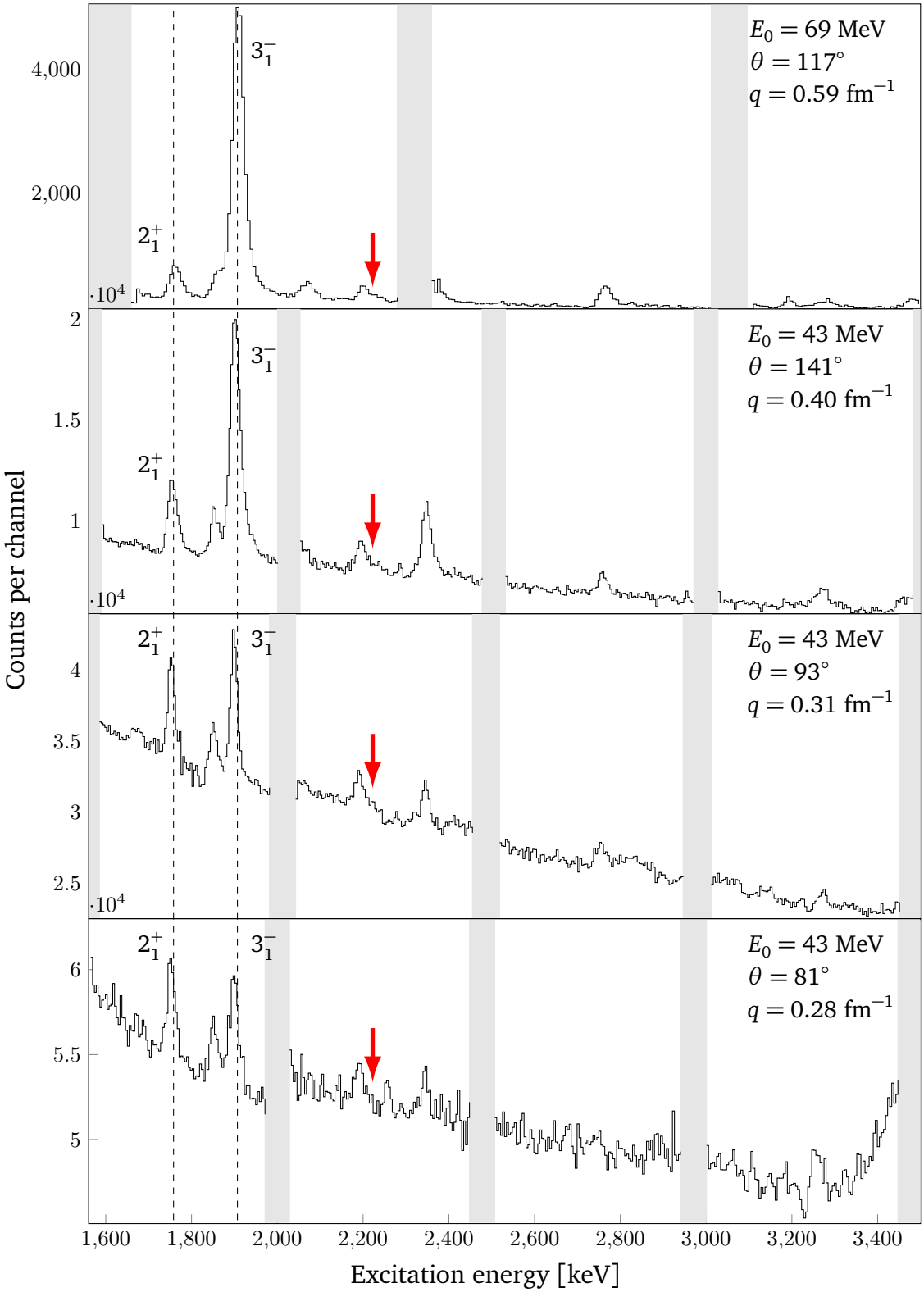

Figure 8.4.: All collected experimental data up to 3.5 MeV. The different experimental conditions are indicated in the figures. These spectra are already energy calibrated (see section 9.1.2), and efficiency corrected (see section 9.1.3). The position of the 2_2^+ state of ^{96}Zr is indicated by the red arrow. The positions of the prominent 2_1^+ and 3_1^- states of ^{96}Zr are indicated by dashed lines. Other transitions visible stem from other zirconium isotopes (see e.g. Figure 9.2). Regions in the spectra that correspond to insensitive areas of the detector system are shown in light gray.

9 Data analysis and results

In this chapter the data analysis and the results of the ^{96}Zr(e,e') experiment are discussed. First, the theoretical basis for the extraction of experimental cross sections from measured spectra will be discussed (sections 9.1.1 and 9.1.2). In section 9.1.3 selected experimental data will serve as an example of the application of these techniques and the estimation and propagation of uncertainties is explained. Then, radiative correction factors to the extracted cross sections are discussed (section 9.1.4). Finally, the extracted peak areas for the 2_1^+ and 2_2^+ states are presented, transition strengths of the different decay modes of the 2_2^+ state are computed, and its lifetime is determined (section 9.2).

9.1 Determination of experimental cross sections

9.1.1 Line shape

The line shape of a single peak in an electron scattering experiment is described using the piecewise defined function

$$y(x) = y_0 \cdot \begin{cases} \exp\left[-\ln 2 \cdot {}^{(x-x_0)^2}/_{\sigma_1^2}\right], & x < x_0 \\ \exp\left[-\ln 2 \cdot {}^{(x-x_0)^2}/_{\sigma_2^2}\right], & x_0 \leq x \leq x_0 + \eta\,\sigma_2 \\ A/(B + x - x_0)^\gamma, & x > x_0 + \eta\,\sigma_2 \end{cases} \tag{9.1}$$

where y_0 is the maximum height and x_0 is the energy at the maximum [163]. The first part of the function ($x < x_0$) is a gaussian with FWHM equal to $2\,\sigma_1$. For $x_0 \leq x \leq x_0 + \eta\,\sigma_2$ the function is a gaussian with FWHM equal to $2\,\sigma_2$. The parameter η defines the starting point of the radiative tail (in units of σ_2) which is described by a hyperbolic function with exponent γ. The parameters A and B are chosen such that the function is continuous and differentiable at $x = x_0 + \eta\,\sigma_2$. For any given spectrum the parameters η, σ_1, σ_2, and γ are fixed by the fit to the most prominent transition in the spectrum whereas the parameters x_0 and y_0 are varied for each peak and are determined by a simultaneous fit including all peaks. For each peak the experimental area content A_{exp}, which is equal to the number of registered counts corresponding to this peak, is then found by integration of Eq. (9.1) up to a certain cutoff energy ΔE above the peak position x_0:

$$A_{exp} = \int_{-\infty}^{x_0+\Delta E} y(x)\,dx. \tag{9.2}$$

The choice of ΔE is arbitrary, as long as it is chosen big enough such that recoil effects and the resolution of the experimental apparatus are smaller than ΔE. Thus, it is convenient to choose ΔE as a multiple of the half width at half maximum $\Delta E = k \cdot \Delta x_1$. In this work $k = 5$ is chosen.

9.1.2 Energy calibration

The raw experimental data consists of the counts registered in each silicon strip (channel) of the detector system. The channels are numbered from 1 to 416 increasing from the low-energy part of the spectrum to the high-energy part. As long as the spectrometer's magnetic field is homogeneous, the energy E' of the scattered electrons can be expressed as a linear function $f(N)$ of the channel number N. Alternatively, E' can be calculated in terms of initial beam energy E_i, excitation energy E_x, target mass M, scattering angle θ, and average energy loss in the target material ΔE

$$f(N) = E'(E_i, E_x, \Delta E, M, \theta) = \frac{(E_i - \Delta E) - E_x \cdot \left(1 + \frac{E_x}{2\,M\,c^2}\right)}{1 + \frac{2\,(E_i - \Delta E)}{M\,c^2}\,\sin^2\frac{\theta}{2}} - \Delta E. \tag{9.3}$$

The average energy loss in the target is roughly given by $\Delta E \approx {}^1/_2 \cdot 1.4 \cdot t_{\text{eff}}$ where t_{eff}, is the effective target thickness in ${}^{\text{mg}}/_{\text{cm}^2}$. This effective thickness depends on the average path length travelled by scattered electrons inside the target. For the transition geometry used in this work it is given by $t_{\text{eff}} = t \cdot \cos^{-1}\left({}^{\theta}/_2\right)$ with the target thickness t in ${}^{\text{mg}}/_{\text{cm}^2}$. Using Eq. (9.3) together with known transitions in the spectra allows the conversion of channel numbers into excitation energies. The transitions used to calibrate the measured data originate from different zirconium isotopes. For an exact energy calibration it is important to take the different nuclear recoils into account which stem from the difference in target mass M. Table 9.1 shows the transitions used to calibrate the measured spectra.

Table 9.1.: Prominent transitions used for the energy calibration of measured spectra. Energies taken from Ref. [97].

Nucleus	Transition	Energy [keV]
^{96}Zr	$2^+_1 \rightarrow 0^+_1$	1750.497(15)
^{92}Zr	$2^+_2 \rightarrow 0^+_1$	1847.27(4)
^{96}Zr	$3^-_1 \rightarrow 0^+_1$	1897.158(16)
^{94}Zr	$3^-_1 \rightarrow 0^+_1$	2057.63(10)
^{92}Zr	$3^-_1 \rightarrow 0^+_1$	2339.66(4)
^{90}Zr	$3^-_1 \rightarrow 0^+_1$	2747.876(16)

9.1.3 Propagation of uncertainties and sample analysis

In this subsection the experimental data for $E_0 = 43$ MeV and $\theta = 141^\circ$ are analyzed in order to document the necessary steps from experimental raw data to the extraction of counts contained in an inelastic peak. Furthermore, the handling of uncertainties during the analysis will be described in detail. Before starting the data analysis the bin contents N_i of each detector channel i can be described with good accuracy by a Poisson distribution with mean value N_i. The statistical uncertainty is then given as the standard deviation of this distribution, which is $\sqrt{N_i}$.

At the beginning of the data analysis it is important to correct the raw data for different relative efficiencies of the silicon strip detectors. This is done by measuring a so-called white

spectrum, which is used as a basis for the correction. In order to obtain such a white spectrum, which is a spectrum with no distortions due to transitions and their radiative tails, one has to measure at excitation energies above the giant dipole resonance of the target nucleus used. If all detectors have the same efficiency the spectrum is expected to be a horizontal line under these conditions. Figure 9.1 shows the spectrum obtained from such a measurement using a ^{208}Pb target. The excitation energy range covered is about 21 MeV to 23 MeV which is well above the giant dipole resonance at around 13.5 MeV [164,165]. The registered counts - and thus the relative detector efficiency - decrease with increasing channel number. Before and after each insensitive area of the detector the number of counts peaks sharply. This is due to the fact that the sensitive areas of the last and first individual silicon strip of each module are larger than those of other strips. In addition to electrons hitting the front of the strips the electrons can also hit the side. This is only possible, because there is no adjacent silicon strip, but an insensitive area without detector material.

The variances in relative detector efficiency are corrected by multiplying the counts N_i in each channel i of the raw data with correction factors c_i such that

$$\tilde{N}_i = N_i \cdot c_i = N_i \cdot \frac{V}{k\, n_i} \,. \tag{9.4}$$

Here n_i is the number of counts in channel i of the efficiency measurement, k is the number of sensitive detector channels, $V = \sum_i n_i$, and $\tilde{N}_i$ is the efficiency corrected number of counts in channel i. The efficiency measurement is subject to the same statistical uncertainty $\sqrt{n_i}$ for

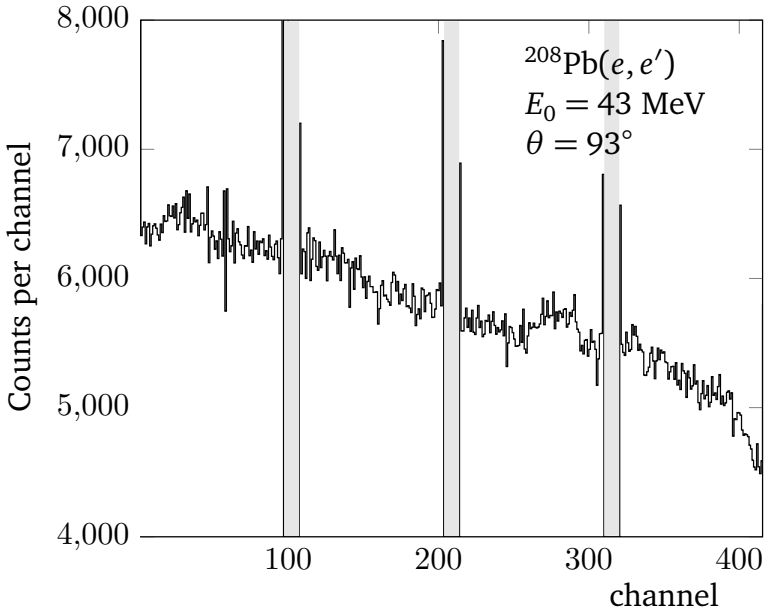

Figure 9.1.: Measurement of the relative detector efficiency for $E_0 = 43$ MeV and $\theta = 93°$. The reaction ^{208}Pb(e,e') at an excitation energy range of about 21 MeV to 23 MeV is used. The relative detector efficiency decreases with increasing channel number i. Silicon strips at the beginning and at the end of each individual detector segment are much more efficient than the remainder of the detector system due to geometrical considerations. Insensitive areas of the detector system are shown in gray.

each channel i as the experimental raw data. The uncertainty for the efficiency corrected data is:

$$\Delta\tilde{N}_i = \sqrt{(N_i \cdot \Delta c_i)^2 + (c_i \cdot \Delta N_i)^2} = N_i\, c_i \cdot \sqrt{\frac{N_i + n_i}{N_i \cdot n_i}}\,. \tag{9.5}$$

After efficiency correction the next step of the analysis is the energy calibration of the data as discussed in section 9.1.2. For this purpose the peaks in the spectrum have to be identified. This can be uniquely done using the known energies and transition strengths [97] of low-lying transitions in the relevant zirconium isotopes. The transitions thus identified are indicated in Fig. 9.2 (see also Table 9.1). For the energy calibration only the transitions that can be clearly separated from neighbouring transitions are used. The energy calibration introduces uncertainties in the energies corresponding to each channel i. For the extraction of peak areas this uncertainty is disregarded, because the position of the peaks is taken as a parameter in the fits of Eq. (9.1) to the data. In order to analyze excited states it is beneficiary to eliminate the effects of the radiative tail of the elastic scattering. Using Eq. (9.1) the radiative tail can be fitted to reproduce the parts of the spectrum that do not contain inelastic transitions. Subtracting this fit F_i from the experimental data results in a spectrum (see lower part in Fig. 9.2) which stems solely from inelastic contributions. A 1σ error band for the fit of the radiative tail of the elastic line is determined and gives an additional error component ΔF_i for each channel i. After subtracting the fit F_i the counts N_i^* in each channel i and the corresponding uncertainties ΔN_i^* are

$$N_i^* = \tilde{N}_i - F_i \text{ , and} \tag{9.6}$$

$$\Delta N_i^* = \sqrt{\left(\Delta\tilde{N}_i\right)^2 + (\Delta F_i)^2}\,. \tag{9.7}$$

Now the inelastic transitions can be analyzed. Their line shape is determined by a fit of Eq. (9.1) to the $2_1^+ \to 0_1^+$ transition of ^{96}Zr. This transition is chosen, because it is isolated in the spectrum and it is strong, which is important for the minimization of statistical uncertainties. From a statistical point of view it would be preferable to use a fit to the elastic peak instead, but the elastically scattered electrons could not be measured simultaneously with the energy region of interests in this work. Apart from amplitude and centroid the line shape is assumed to be the same for all transitions in the same measurement. The widths σ_1 and σ_2 of the Gaussian distributions stem mainly from the experimental setup. The contribution of the internal line width is much smaller than the experimental contributions (detector and spectrometer resolution, beam quality), which are constant for all transitions. The parameters A, B, and γ include the radiative effects, which do depend on the target mass M and the excitation energy E_x. For the narrow range of target masses, ranging from $\mathrm{M}\left(^{90}\mathrm{Zr}\right)$ to $\mathrm{M}\left(^{96}\mathrm{Zr}\right)$, and the narrow ranges of excitation energies from 1.5 MeV to 3.5 MeV this dependence is negligible and the parameters can be taken as constant. Figure 9.3 shows a fit of Eq. (9.1) to the $2_1^+ \to 0_1^+$ transition of ^{96}Zr. An additional linear offset is allowed, because the subtraction of the background from elastic scattering does not work sufficiently well throughout the whole spectrum. A 1σ uncertainty band has been determined using a χ^2 parameter estimation and is shown as dashed lines. Integrating this fit according to Eq. (9.2) results in an experimental area $A(2_1^+) = \left(102.4^{+2.7}_{-2.5}\right) \cdot 10^3$ counts of the peak. Using the determined line shape the 2_2^+ state of ^{96}Zr can be analyzed. The transition $2_2^+ \to 0_1^+$ is located at 2226(1) keV close to the much stronger $2_1^+ \to 0_1^+$ transition of ^{90}Zr at

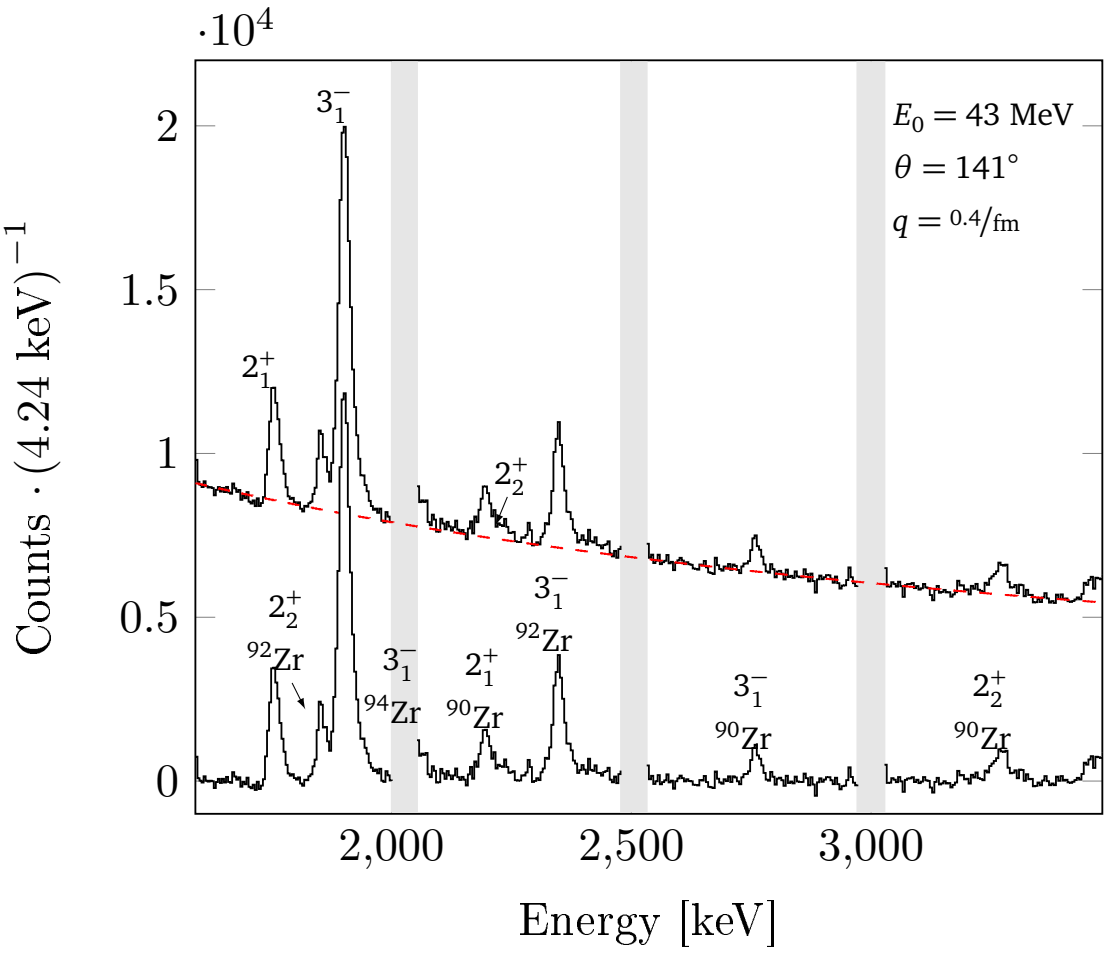

Figure 9.2.: Summed and efficiency corrected experimental data for $\theta = 141°$ and $E_0 = 43$ MeV. The upper histogram shows the data including contributions from the elastic line. The lower histogram shows the same data with the radiative tail of the elastic line (red, dashed) subtracted. Many transitions from different zirconium isotopes can be clearly identified. If a transition does not stem from ^{96}Zr its origin has been stated. For reasons of clarity errors to the data points are not shown, but are discussed in the text. Grey areas correspond to inactive segments of the detector system.

2186(1) keV. In order to extract the area content it is necessary to fit both transitions simultaneously. To determine the best solution as well as an uncertainty to this solution a χ^2 analysis is used

$$\chi^2 = \sum_i \frac{\left(N_i^* - f(i, x_{01}, x_{02}, y_{01}, y_{02})\right)^2}{\Delta N_i^*}, \tag{9.8}$$

where $x_{01,02}$ and $y_{01,02}$ correspond to the energy and amplitude of the 2_1^+ state of ^{90}Zr and the 2_2^+ state of ^{96}Zr, respectively. Furthermore, the function f is given by

$$f(i, x_{01}, x_{02}, y_{01}, y_{02}) = y(x, x_0 = x_{01}, y_0 = y_{01}) + y(x, x_0 = x_{02}, y_0 = y_{02}), \tag{9.9}$$

where $y(x)$ is the line shape as defined in Eq. (9.1). The amplitudes y_{01}, y_{02} and the positions x_{01}, x_{02} of the two transitions are then varied and the corresponding χ^2 values are calculated.

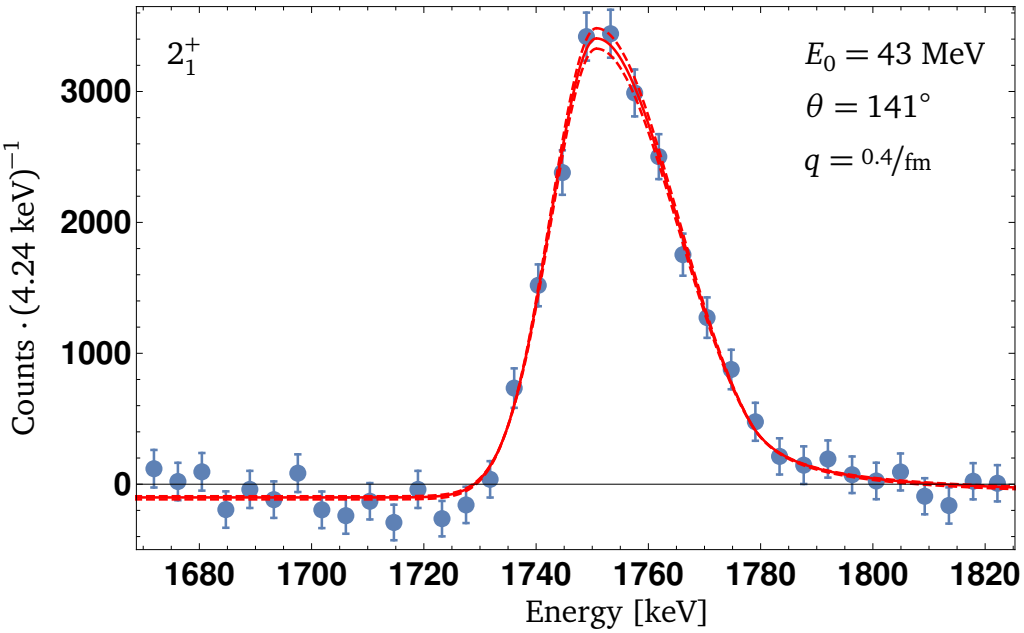

Figure 9.3.: Fit of the electron scattering line shape to the 2_1^+ state of ^{96}Zr. It is clearly separated from other peaks in the spectrum and has sufficient statistics to fit its line shape with high precision using Eq. (9.1). The dotted lines represent a 1σ uncertainty band for the fit. Extracted parameters are used to fit the other inelastic transitions in the spectrum.

The best fit to the experimental data corresponds to the minimum value of χ^2. Figure 9.4(a) shows the results for $\Delta\chi^2 = \chi^2 - \chi^2_{min}$ projected to the $y_{01} - y_{02}$ plane. The best fit ($\Delta\chi^2 = 0$) defines the values for the amplitudes $y_{01} = 1574$ counts per channel and $y_{02} = 426$ counts per channel. For the extraction of area content $A(2_2^+)$ of the 2_2^+ state of ^{96}Zr only the uncertainty of y_{02} is of interest. In order to get a 1σ confidence interval for the amplitude y_{02} the $\chi^2 = \chi^2_{min} + 1$ contour is projected onto the corresponding axis. This yields in $y_{02} = \left(426^{+63}_{-60}\right)$ counts per channel. The resulting fit is shown as a solid line in Figure 9.4(b) while the dashed lines represent the fit corresponding to the 1σ uncertainty interval of y_{02}. Integration of the best fit and subtracting the counts corresponding to the 2_1^+ of ^{90}Zr yields $A(2_2^+) = \left(12.5^{+1.8}_{-1.8}\right) \cdot 10^3$ counts. The propagation of uncertainties through the different analysis steps is summarized in Table 9.2.

Table 9.2.: Propagation of uncertainty from raw data to area extraction. Details are given in the text.

Analysis step	Counts per channel	Uncertainty
raw data	N_i	$\sqrt{N_i}$
efficiency corrected	$\tilde{N}_i = N_i \cdot c_i$	$\sqrt{(N_i \cdot \Delta c_i)^2 + (c_i \cdot \Delta N_i)^2}$
after subtraction of elastic line	$N_i^* = \tilde{N}_i - F_i$	$\sqrt{\Delta\tilde{N}_i^2 + \Delta F_i^2}$
area extraction	-	given by χ^2 analysis

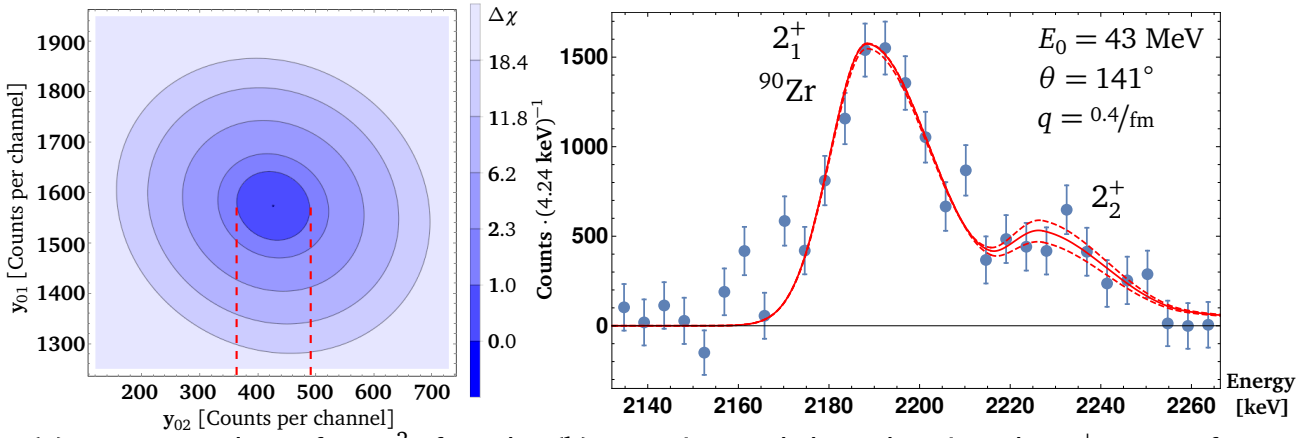

(a) Contour plot of $\Delta\chi^2$ for the fit to the experimental data. The best solution corresponds to $\Delta\chi^2 = 0$. The 1σ uncertainty for y_{02} is given by a projection of the $\Delta\chi^2 = 1$ contour onto the corresponding axis as indicated by the dashed lines. See text for further explanations.

(b) Experimental data showing the 2^+_1 state of ^{90}Zr and the 2^+_2 state of ^{96}Zr for the measurement at $\theta = 141°$ and $E_0 = 43$ MeV. The best fit to the data is shown (solid line) with the 1σ error band with respect to y_{02} dashed.

Figure 9.4.: Simultaneous fit of the 2^+_1 state of ^{90}Zr and the 2^+_2 state of ^{96}Zr (right) and corresponding χ^2 plot projected onto the $y_{01} - y_{02}$ plane (left).

9.1.4 Correction factors

In an electron scattering experiment the incoming electron beam interacts with the target. The elastically or inelastically scattered electrons are then detected and the energy loss due to the interaction with the target is determined. Apart from inelastic scattering there are additional interactions, the radiative effects, which cause the electrons to lose energy while passing the target. One possibility is the emission of bremsstrahlung as the electron is accelerated in the electric field of the target. Another source of energy loss is the ionization effect. It is energy loss caused by the interaction of the incident electrons with the electrons of the target. Finally one has to take into account the photon self-energy and the possibility that the incident electrons emit and reabsorb virtual photons [132]. The energy loss by the radiative effects is continuous and can cause the electron to lose up to its complete energy. This is problematic, because the extraction of the peak content A_{exp} from experimental data is done by integrating the line shape (Eq. (9.1)) of each peak up to a certain threshold energy ΔE, as defined in Eq. (9.2). All electrons that lost more energy than ΔE will be missed in the integration. This leads to an error in the extracted peak area A_{exp} that can be corrected by multiplying it with correction factors in order to arrive at the corrected peak content A_{cor}:

$$A_{cor} = A_{exp} \cdot e^{\delta_S + \delta_B + \delta_I}. \tag{9.10}$$

The different exponents correspond to the Schwinger correction δ_S, which includes the correction for the photon self-energy and the emission and reabsorption of virtual photons, correction

of bremsstrahlung effects δ_B, and the ionization correction δ_I. The most important correction factor for (e,e') experiments with thin targets is the Schwinger correction. The exponent δ_S is given by [166]

$$\delta_S = \frac{2\,\alpha}{\pi}\left(\left[\frac{1}{2}\ln\left(\frac{E_0}{\eta^2\,\Delta E}\right)+\frac{1}{2}\ln\left(\frac{E_f}{\Delta E}\right)-\frac{13}{12}\right]\cdot\left[2\ln\left(\frac{E_R}{m_0\,\mathrm{c}^2}\right)-1\right]+\frac{17}{36}\right) \tag{9.11}$$

where α is the fine structure constant, E_0 is the incident electron energy, E_f is the energy of the outgoing electron, m_0 is the electron rest mass, $\eta = 1 + \frac{2\,E_0}{m_0\,\mathrm{c}^2}\cdot\sin^2(\theta/2)$ is the recoil parameter, and

$$E_R = \frac{(q\cdot\hbar\,\mathrm{c})^2}{2\,(M\,\mathrm{c}^2+E_x)} \tag{9.12}$$

is the recoil energy with the target mass M and the excitation energy E_x. The bremsstrahlung correction is proportional to the effective target thickness t_{eff} and can be written as:

$$\delta_B = \frac{t_{\mathrm{eff}}}{X_0\,\ln 2}\left[\frac{1}{2}\ln\left(\frac{E_0}{\eta^2\,\Delta E}\right)+\frac{1}{2}\ln\left(\frac{E'}{\eta\,\Delta E}\right)\right] \tag{9.13}$$

with the radiation length X_0 [167]. The radiation length measures the path length over which electrons passing the target degrade in energy to E_0/e. It can be approximated by

$$X_0 = \frac{716.4A}{Z\,(Z+1)\,\ln(287\,Z^{-1/2})}\left[\frac{\mathrm{g}}{\mathrm{cm}^2}\right], \tag{9.14}$$

where A is the mass number of the target nucleus and Z is the atomic number. Finally, the ionization correction also depends on A, Z, and the target thickness. Furthermore, it depends on the target density and on the energy of the incident electrons [168]. All these factors are identical for the 2_2^+ and the 2_1^+ states of ^{96}Zr, thus the ionization correction cancels exactly in a relative analysis. This is not true for the Schwinger and bremsstrahlung corrections, which must be taken into account explicitly even in a relative analysis. However, for the states in question and the different experimental conditions even the bremsstrahlung and Schwinger corrections cancel to better than 1 %. Additional information about radiative corrections can be found in, e.g., Mo and Tsai [169]. Details about the ionization correction in particular are given in Refs. [170–172].

9.2 Results

The results of the ^{96}Zr(e,e') experiment are summarized in Tab. 9.3. For the 2_1^+ state it was possible to extract area contents for all kinematics measured. The estimated uncertainties in the peak areas range from 2.7 % (141°) to 11.0 % (81°). The main contributions to the uncertainty are the subtraction of the elastic background and statistical uncertainties. Extraction of peak areas from the experimental data is more difficult for the 2_2^+ state, because of the overlapping 2_1^+ state of ^{90}Zr. The estimated uncertainties range from 14.4 % (141°) to 141.5 % (81°). The measurement at $\theta = 81°$ suffered from additional background originating from the direction of the scattering chamber. These problems cause large uncertainties and make this data point almost irrelevant for further analysis. A later experiment showed a significant reduction in

Table 9.3.: Extracted experimental peak areas A_{exp} for the 2_1^+ and 2_2^+ states of ^{96}Zr.

q $\left[\text{fm}^{-1}\right]$	E_0 [MeV]	θ [°]	$A(2_1^+)$ $\left[10^3 \cdot \text{counts}\right]$	$A(2_2^+)$ $\left[10^3 \cdot \text{counts}\right]$	$R_F\sqrt{\frac{A(2_2^+)}{A(2_1^+)}}$
0.59	69	117	$18.8^{+0.5}_{-0.5}$	$2.3^{+0.5}_{-0.5}$	0.35 ± 0.05
0.40	43	141	$102.4^{+2.7}_{-2.5}$	$12.5^{+1.8}_{-1.8}$	0.35 ± 0.03
0.31	43	93	$139.1^{+5.9}_{-5.9}$	$14.2^{+4.6}_{-4.8}$	0.32 ± 0.05
0.28	43	81	$147.4^{+15.6}_{-16.1}$	$10.6^{+15.0}_{-15.0}$	0.27 ± 0.19

background at $\theta = 81°$ by using additional lead shielding between the scattering chamber and the spectrometer [73]. In order to extract a $B(\text{E2}; 2_2^+ \to 0_1^+)$ value from the experimental data according to section 7.2 a plot of $R_F\sqrt{A(2_2^+)/A(2_1^+)}$, where R_F is a ratio of kinematical factors defined in Eq. (7.32), over q_0^2 is used (Figure 9.5). The experimental data is shown in blue and is included in Tab. 9.3. The black data show the lower limit given by the $B(\text{E2}; 2_2^+ \to 0_1^+)$ limit from literature [97]. The experimental uncertainties are calculated as

$$\Delta\left(R_F\sqrt{\frac{A(2_2^+)}{A(2_1^+)}}\right) = \frac{1}{2}\cdot R_F\sqrt{\frac{A(2_2^+)}{A(2_1^+)}}\cdot\sqrt{\left(\frac{\Delta A(2_2^+)}{A(2_2^+)}\right)^2+\left(\frac{\Delta A(2_1^+)}{A(2_1^+)}\right)^2}. \tag{9.15}$$

This is possible, because the uncertainties of the extracted peak areas are approximately Gaussian distributed (see, e.g., Fig. 9.4(a)). A χ^2 minimization of Eq. (7.31) with respect to the square root of the $B(\text{E2})$ ratio and the difference in transition radii ΔR yields

$$\sqrt{\frac{B(\text{E2}; 2_2^+ \to 0_1^+)}{B(\text{E2}; 2_1^+ \to 0_1^+)}} = 0.335^{+0.050}_{-0.040}\text{, and} \tag{9.16}$$

$$\Delta R = \left(-0.22^{+0.87}_{-0.92}\right)\text{ fm}. \tag{9.17}$$

The transition radius $R_{tr,1}$ used is 5.38 fm, as suggested by a QRPA calculation [140]. The uncertainties have been extracted by projecting the $\Delta\chi^2 = 1$ contour onto the different axis as described for the extraction of peak areas in Sec. 9.1.3. The best fit is represented by a solid red line in Fig. 9.5 whereas the dashed lines represent the solutions that define the 1σ uncertainty for $\sqrt{B(\text{E2};2_2^+\to0_1^+)/B(\text{E2};2_1^+\to0_1^+)}$. It is evident that this experiment is unable to determine the value for ΔR with high precision. The extracted value is consistent with zero. The situation for transitions strengths is different. Combining Eq. (9.16) with the literature value $B(\text{E2}; 2_1^+ \to 0_1^+) = 2.3 \pm 0.3$ W.u. [97] yields $B(\text{E2}; 2_2^+ \to 0_1^+) = 0.26^{+0.09}_{-0.07}$ W.u.. This value is in good agreement with the value of $0.05-0.23$ W.u. obtained by Hofer et al. [121] in proton and deuteron scattering experiments. The error propagation of the non-Gaussian uncertainties was done using a maximum likelihood approach. The 1σ error interval is defined by $\Delta \log L = -0.5$ with the likelihood function L [174].

It should be noted that even though theoretical (QRPA) input has been used to fix the value of $R_{tr,1}$ to 5.38 fm, the analysis is independent of this input. It has been repeated for several values of $R_{tr,1}$ covering a range from 4.38 fm to 6.38 fm. The result of this investigation is

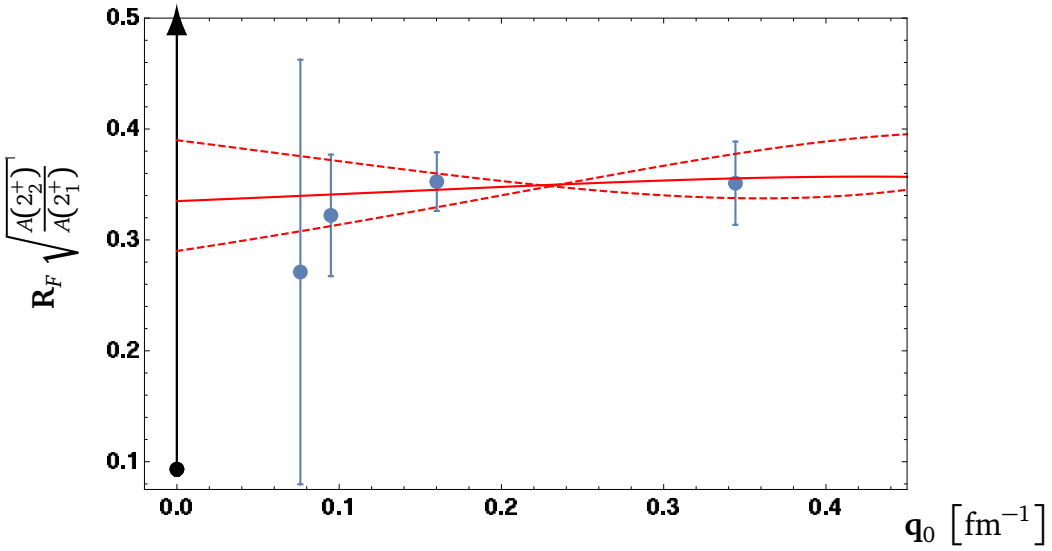

Figure 9.5.: Value of $R_F \sqrt{A(2_2^+)/A(2_1^+)}$ as a function of elastic momentum transfer q_0. The solid red line shows the best fit of Eq. (7.31) to the experimental data (blue). The dashed lines represent the 1σ uncertainties with respect to $\sqrt{B(\mathrm{E2};2_2^+ \to 0_1^+)/B(\mathrm{E2};2_1^+ \to 0_1^+)}$. The previously known experimental lower limit [173] is shown in black.

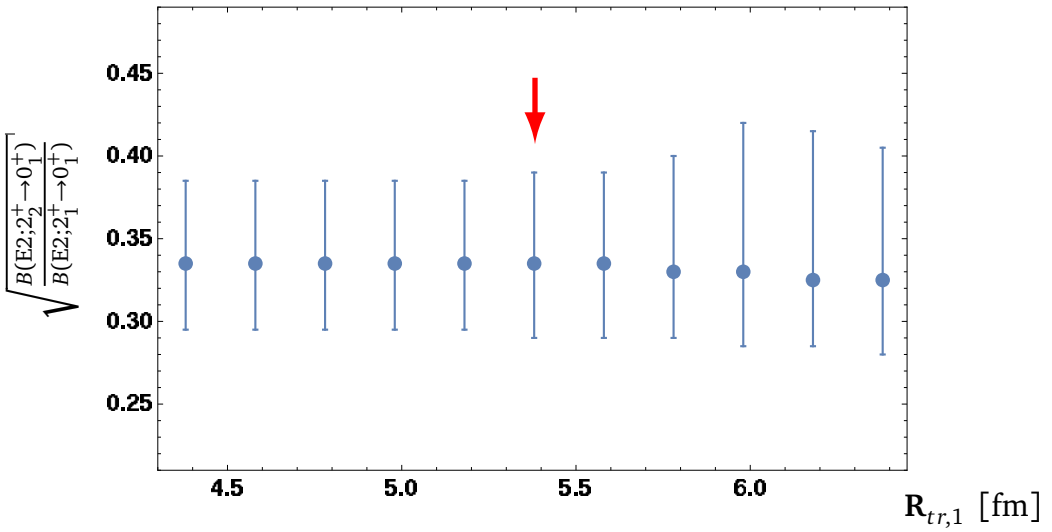

Figure 9.6.: Dependence of the extracted $\sqrt{B(\mathrm{E2};2_2^+ \to 0_1^+)/B(\mathrm{E2};2_1^+ \to 0_1^+)}$ value on the input parameter $R_{tr,1}$. The data point used for the analysis is $R_{tr,1} = 5.38$ fm suggested by QRPA calculations and indicated by a red arrow. Changes in $R_{tr,1}$ up to $\pm$ 1.0 fm do not change the extracted $B(\mathrm{E2})$ ratio within 3%. For large values of $R_{tr,1}$ the uncertainty increases.

Table 9.4.: Transition strengths for decays of the 2_2^+ state of ^{96}Zr obtained from experimental data. The $B(\mathrm{M2}; 2_2^+ \rightarrow 3_1^+)$ value is consistent with zero. All data except transition strengths are taken from Ref. [97].

J_f^π	E_γ [keV]	I_γ	Multipolarity	δ	Transition strength
3_1^-	328.75(3)	14(1)	E1+M2	−0.02(5)	$B(\mathrm{E1}) = \left(27.6^{+9.9}_{-7.8}\right) \cdot 10^{-3}$ W.u.
2_1^+	475.33(1)	57(1)	M1+E2	$-0.09^{+0.01}_{-0.02}$	$B(\mathrm{M1}) = \left(0.14^{+0.05}_{-0.04}\right)\ \mu_N^2$
					$B(\mathrm{E2}) = \left(2.7^{+1.3}_{-1.2}\right)$ W.u.
0_2^+	644.18(6)	28(1)	E2		$B(\mathrm{E2}) = \left(35.6^{+12.5}_{-9.8}\right)$ W.u.
0_1^+	2225.93(5)	100(5)	E2		$B(\mathrm{E2}) = \left(0.26^{+0.09}_{-0.07}\right)$ W.u.

shown in Fig. 9.6. The extracted value of $\sqrt{B(\mathrm{E2}; 2_2^+ \rightarrow 0_1^+)/B(\mathrm{E2}; 2_1^+ \rightarrow 0_1^+)}$ stays constant within 3%. The uncertainty remains stable for $R_{tr,1}$ values lower than the QRPA suggestion, but increases considerably if $R_{tr,1}$ is chosen higher. This increase in uncertainty is brought about by solutions that include ΔR values above 1.5 fm, which cannot be excluded by the experimental data but seem physically unjustified. If the change in transition radii between the 2_1^+ and 2_2^+ states is artificially limited, e.g. to ±1 fm, then this increase in uncertainty is not seen.

Using the known gamma intensities I_γ and multipole mixing ratios δ as well as the obtained $B(\mathrm{E2}; 2_2^+ \rightarrow 0_1^+)$ the determination of transition strengths for other decay channels of the 2_2^+ state and the calculation of its lifetime is possible. The relation of lifetime τ_i or decay constant λ_i to the transition strength for any initial state i is given by

$$\lambda_i = \frac{1}{\tau_i} = \frac{1}{\hbar} \cdot \sum_f \frac{8\,\pi\,(\lambda+1)}{\lambda\,[(2\,\lambda+1)!!]^2} \left(\frac{E_\gamma}{\hbar\,c}\right)^{2\,\lambda+1} B\left(X\,\lambda : J_i \rightarrow J_f\right) \cdot \left(1+\alpha_f\right). \tag{9.18}$$

Here $E_\gamma = E_i - E_f$ is the energy of the transition, $E_{i,f}$ and $J_{i,f}$ are the energies and spins of initial i and final states f, $X \in \{\mathrm{E}, \mathrm{M}\}$, λ is the multipolarity of the transition, and α_f denotes the internal conversion coefficient of the final state. In order to obtain the transition strengths of other decay channels from the already determined $B(\mathrm{E2}; 2_2^+ \rightarrow 0_1^+)$ value it is important to note that the ratio of gamma intensities I_γ is equal to the ratio of partial decay constants if the contribution from conversion electrons can be neglected. The extracted transition strengths are summarized in Tab. 9.4. From Eq. (9.18) a lifetime of $\tau = \left(0.34^{+0.9}_{-0.7}\right)$ ps or equivalently a half-life of $T_{1/2} = \left(0.24^{+0.6}_{-0.5}\right)$ ps for the 2_2^+ state of ^{96}Zr is obtained. The internal conversion coefficients α_f are taken from literature [97]. The determined half-life is two orders of magnitude shorter than the previous limit of $T_{1/2} < 10$ ps which was established by measuring the β^- decay of ^{96}Y using the centroid shift method [173].

10 Interpretation

The new experimental data acquired in this work, especially the measurement of the small $B(\mathrm{E2}; 2_2^+ \rightarrow 0_1^+)$ value and the evaluation of the large $B(\mathrm{E2}; 2_2^+ \rightarrow 0_2^+)$ value, are important to understand the low-lying nuclear structure in ^{96}Zr.

The measured $B(\mathrm{E2}; 2_2^+ \rightarrow 0_1^+)$ value and the deduced $B(\mathrm{M1}; 2_2^+ \rightarrow 2_1^+)$ value are both too small for a mixed symmetry assignment. This eliminates the 2_2^+ as a possible mixed-symmetric excitation. In addition, the energetically next 2^+ state at 2.67 MeV is also not a suitable candidate for an MSS assignment. While its $B(\mathrm{E2}; 2_3^+ \rightarrow 0_1^+)$ has not been measured yet, its $B(\mathrm{M1}; 2_3^+ \rightarrow 2_1^+) = 0.16\,\mu_N^2$, which has been determined by a combination of Doppler-shift [175], $(n, n'\gamma)$, and $(p, p'\gamma)$ experiments [176], is too small for a mixed-symmetric state. As there is no more suitable candidate at lower energies, this means that the one quadrupole MSS state of ^{96}Zr is located above 3 MeV. A higher excitation energy for the MSS state, compared to neighbouring nuclei, is consistent with the double subshell closure of ^{96}Zr.

The strong E2 transition between the 2_2^+ and 0_2^+ states suggests that the 2_2^+ state is a collective excitation build on top of the 0_2^+ state. The weak transitions between the states of the ground-state band and the 0_2^+ and 2_2^+ state further suggest, that the structure of the 0_2^+ state and the band build on top of it is significantly different (deformed) from the structure of the spherical ground state. The mixing model outlined in Sec. 6.1 can be used to study this situation quantitatively. The experimentally observed states can be written as an admixture of spherical (s) and deformed (d) underlying structures

$$
\begin{aligned}
|\,0_1^+\rangle &= \alpha\,|\,0_\mathrm{s}^+\rangle + \beta\,|\,0_\mathrm{d}^+,\rangle && (10.1)\\
|\,0_2^+\rangle &= -\beta\,|\,0_\mathrm{s}^+\rangle + \alpha\,|\,0_\mathrm{d}^+,\rangle && (10.2)\\
|\,2_1^+\rangle &= \gamma\,|\,2_\mathrm{s}^+\rangle + \delta\,|\,2_\mathrm{d}^+,\rangle && (10.3)\\
|\,2_2^+\rangle &= -\delta\,|\,2_\mathrm{s}^+\rangle + \gamma\,|\,2_\mathrm{d}^+,\rangle && (10.4)
\end{aligned}
$$

where α, β, γ, and δ are amplitudes with $\alpha^2 + \beta^2 = \delta^2 + \gamma^2 = 1$. Assuming that the spherical and deformed configurations do not decay into one another (see Fig. 10.1(b)), the decays of the experimental states can be attributed to mixing of the spherical and deformed structures. Further, it is assumed that the 0^+ states and 2^+ states mix with the same mixing matrix element V_mix. Using Eqs. (10.1) to (10.4), Eq. (7.21), and the set of Eqs. given by (6.1) together with the experimental energies $\mathrm{E}(0_1^+)$, $\mathrm{E}(0_2^+)$, $\mathrm{E}(2_1^+)$, $\mathrm{E}(2_2^+)$, and transition strengths $B(\mathrm{E2}; 2_1^+ \rightarrow 0_1^+)$, and $B(\mathrm{E2}; 2_2^+ \rightarrow 0_2^+)$ the amplitudes α, β, γ, δ, the mixing matrix element V_mix, and the energies of the unperturbed states can be determined. The results of this calculation are shown in Fig. 10.1. The amplitudes

$$
\alpha^2 = 0.998, \quad \beta^2 = 0.002 \quad \text{and} \quad \gamma^2 = 0.975, \quad \delta^2 = 0.025, \tag{10.5}
$$

and the small mixing matrix element $V_\mathrm{mix} = 76$ keV show that the mixing is very weak. The experimentally observed states are almost pure with regards to the different underlying structures. This can also be seen by inspecting the energies and transition strengths of the underlying structures, which are shown in Fig. 10.1(b). The energies of the unmixed states do not deviate significantly from the energies of the mixed states. The spacing between the 0^+ states and

their corresponding 2^+ excitation is slightly reduced for the unmixed state, as expected from Eq. (6.1). The transition strengths between the unmixed configurations are larger than for the mixed configurations. This indicates different signs for the matrix elements $M_s = \langle 0_s^+ \mid \hat{T}^{\mathrm{E2}} \mid 2_s^+ \rangle$ and $M_d = \langle 0_d^+ \mid \hat{T}^{\mathrm{E2}} \mid 2_d^+ \rangle$. For the unmixed configurations the transition strengths are proportional to the square of the matrix element, whereas for the mixed states the different signs of the matrix elements cause a partial cancellation

$$B(\mathrm{E2}; 2_x^+ \to 0_x^+) = \frac{1}{5} \mid M_x \mid^2 \text{ with } x \in \{s, d\}, \tag{10.6}$$

$$B(\mathrm{E2}; 2_1^+ \to 0_1^+) = \frac{1}{5} \mid \alpha\,\gamma\,M_s + \beta\,\delta\,M_d \mid^2, \tag{10.7}$$

$$B(\mathrm{E2}; 2_2^+ \to 0_2^+) = \frac{1}{5} \mid \delta\,\beta\,M_s + \gamma\,\alpha\,M_d \mid^2 . \tag{10.8}$$

The absolute signs of M_s and M_d could not be deduced within this model.

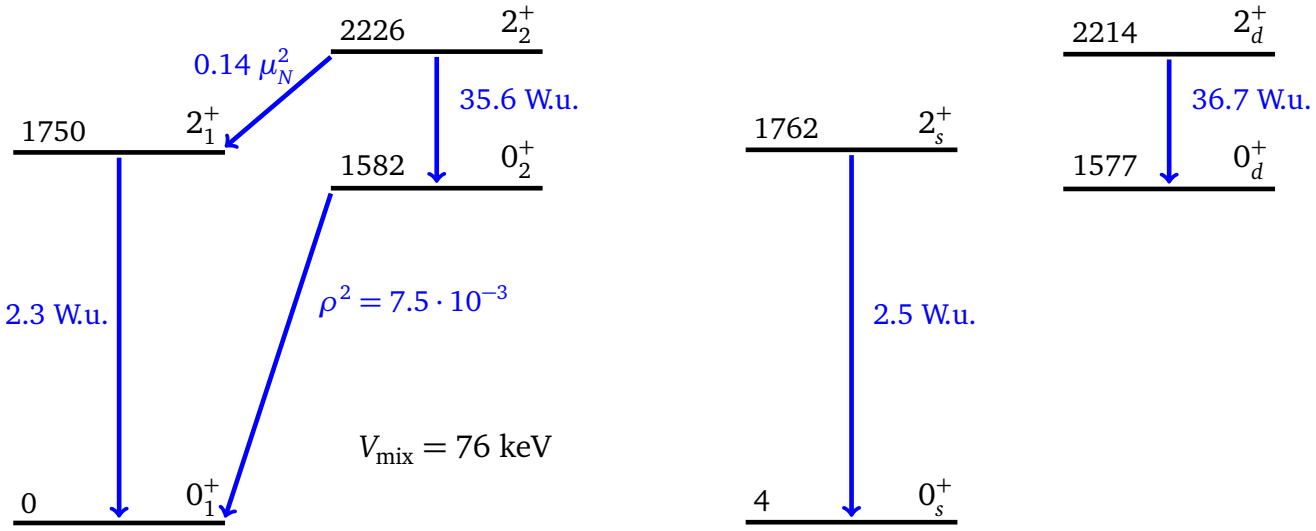

(a) Experimentally observed (mixed) states.

(b) Underlying unmixed configurations.

Figure 10.1.: Low-lying states of ^{96}Zr (left) and assumed underlying structure (right). Energies are given in keV. Note that neither $B(\mathrm{M1}; 2_2^+ \to 2_1^+)$ nor $B(\mathrm{E0}; 0_2^+ \to 0_1^+)$ has been used in the mixing calculation.

Assuming a quadrupole-deformed shape for the unmixed deformed states 0_d^+ and 2_d^+, the quadrupole deformation parameter $\beta_{2,d}$ of the deformed band is estimated to be

$$\beta_{2,d} = \frac{4\,\pi}{3\,Z\,R_0^2} \cdot \left(\frac{B(\mathrm{E2};\, 0_d^+ \to 2_d^+)}{e^2} \right)^{\frac{1}{2}} \approx 0.24, \tag{10.9}$$

where $R_0 = 1.2\ \mathrm{fm} \cdot A^{1/3}$ has been used. This deformation is similar to the value ($\beta_2 \approx 0.2$) deduced by Mach et al. [120].

The calculated mixing matrix element ($V_{\mathrm{mix}} = 76$ keV) is strikingly different from the matrix element $V'_{\mathrm{mix}} \approx 0.8$ MeV suggested by Heyde [177], which was calculated within the shell model

by considering the pairing interaction $V_{\pi\pi}$ of the dominant proton configurations for the ground state ($2p^2_{1/2}$) and the first excited 0^+ state ($1g^2_{9/2}$). Even though these matrix elements cannot be directly compared, as the corresponding unperturbed Hamiltonians are different, a difference of this magnitude is a clear indication that the 0^+_2 state of ^{96}Zr is only poorly approximated by a proton $1g^2_{9/2}\,2p^{-2}_{1/2}$ two-particle-two-hole (2p-2h) excitation, which was assumed to be the dominant part of this state by Heyde [177].

In light of the experimental data obtained in this work a new shell model calculation for ^{96}Zr has been performed by Otsuka [178]. The model space consists of $1f_{5/2}$, $2p_{3/2}$, $2p_{1/2}$ (all pf shell), and the full sdg shell for protons and the full sdg shell, $1h_{11/2}$, $3p_{3/2}$, and $2f_{7/2}$ for neutrons. A schematic illustration of the model space is shown in Fig. 10.2.

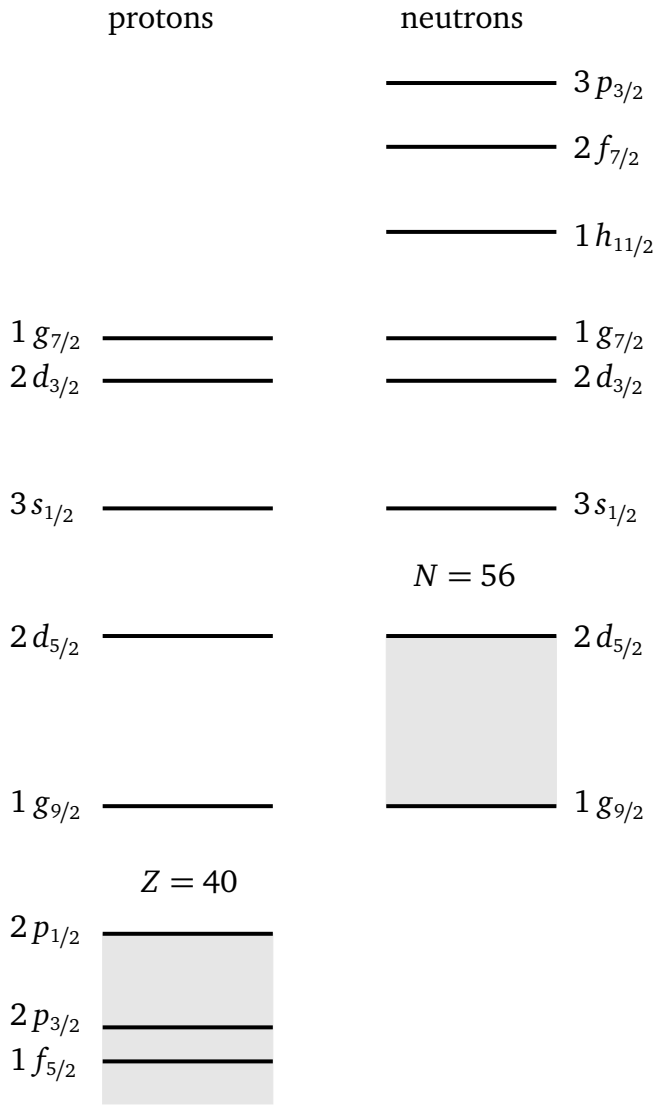

Figure 10.2.: Schematic illustration of the model space used in the shell-model calculation. Protons exhibit a subshell closure at $Z = 40$ and neutrons show a subshell closure at $N = 56$. The gray shading indicates the orbitals occupied in the ground state of ^{96}Zr.

The effective interaction used in the Hamiltonian is based on a combination of existing interactions. For the orbitals $1f_{5/2}$, $2p_{3/2}$, $2p_{1/2}$, and $1g_{9/2}$ the JUN45 interaction [179] is used. For the

$T = 1$ interactions of the $1g_{7/2}$, $2d_{5/2}$, $2d_{3/2}$, $3s_{1/2}$, and $1h_{11/2}$ orbitals the snbg3 interaction [180] is used. The V_{MU} [181] interaction is used in all other cases. The sngb3 and V_{MU} interactions are tuned to reproduce the energies of the 2_1^+ states of the Zr isotopic chain. The resulting Hamiltonian produces energies of the 2_1^+ states in close correspondence with the experimental values (see Fig. E.1 in appendix E). The results obtained with this effective interaction for the lowest lying states of ^{96}Zr are summarized in Tab. 10.1.

Table 10.1.: Comparison of energies and transition strengths for the low-lying states of ^{96}Zr with the shell-model calculations. The effective charges used are $e_p = 1.5\,e$ and $e_n = 0.5\,e$.

	experiment	shell model
$E(0_1^+)$ [MeV]	0.00	0.00
$E(0_2^+)$ [MeV]	1.58	2.30
$E(2_1^+)$ [MeV]	1.75	1.90
$E(3_1^-)$ [MeV]	1.90	2.72
$E(2_2^+)$ [MeV]	2.23	2.69
$B(\mathrm{E2}; 2_1^+ \to 0_1^+)$ [W.u.]	2.3 ± 0.3	0.7
$B(\mathrm{E2}; 2_2^+ \to 0_2^+)$ [W.u.]	$35.6^{+12.5}_{-9.8}$	36.9
$B(\mathrm{E2}; 2_2^+ \to 0_1^+)$ [W.u.]	$0.26^{+0.09}_{-0.07}$	0.00
$B(\mathrm{M1}; 2_2^+ \to 2_1^+)$ [μ_N^2]	$0.14^{+0.05}_{-0.04}$	0.00
$B(\mathrm{E3}; 3_1^- \to 0_1^+)$ [W.u.]	57(4)	39.5

Qualitatively, the shell model is able to reproduce the experimentally observed structures. The theoretical excitation spectrum contains two sets of structurally different states. A spherical ground-state band and a deformed 0_2^+ with a collective band on top. The transition strength of deformed states are reproduced well. The interband B(E2) value of the deformed band matches the experimental value within uncertainties, whereas that of the spherical ground-state band is underestimated by a factor of three. The strong octupole collectivity of the 3_1^- state is also present in the model calculations. The absence of mixing of the sperhical and deformed bands, as exemplified by vanishing transition strengths between them, is noteworthy and contradictory to experiment, where a weak mixing has been observed. The excitation energies are not reproduced nearly as well as the transition strength. The ordering of the predicted levels is wrong and the 0_2^+ state is not reproduced as the lowest excited state in the shell model calculation. Furthermore the calculated excitation energy of the 2_2^+ state is larger than the experimental value by more than 400 keV and those of the 0_2^+ and 3_1^- are roughly 800 keV larger than the experimental value.

In addition to energies and transition strengths the occupation numbers of all orbitals of the model space have been calculated for the two energetically lowest-lying 0^+ and 2^+ states (see Fig. 10.3). For the ground state the proton orbitals up to $2p_{1/2}$ are almost completely filled, whereas the orbitals with higher ESPEs are, to good approximation, empty. This is the subshell closure at $Z = 40$. For the neutrons the situation is similar. All orbitals up to $2d_{5/2}$ are occupied, whereas occupation of energetically higher-lying orbitals is rare. This is the $N = 56$ subshell closure. The occupation numbers for the 2_1^+ state are similar to those of the ground state. The notable difference is a neutron particle-hole excitation, which mainly stems from an excitation of a neutron from $2d_{5/2}$ to $3s_{1/2}$.

The structure of the deformed states is very different from the spherical ones. The occupation numbers of 0_2^+ and 2_2^+ are basically identical highlighting the common structure of these states. In comparison with the ground state these excitations are of multiparticle-multihole character. The occupation numbers suggest the excitations to be, on average, of 5p-5h type. Two protons are excited from various orbitals of the pf shell above the $Z = 40$ subshell closure into (mainly) the $1g_{9/2}$ orbital. Three neutrons are excited from $2d_{5/2}$ above the $N = 56$ subshell closure into various orbitals, mainly $1g_{7/2}$, $2d_{3/2}$, and $1h_{11/2}$. The proton excitation coincides with the 4p-4h interpretation of Mach et al. [120] and Molnar, Yates, and Meyer [119]. The neutron part of the excitation contains, on average, more particle-hole excitations above $N = 56$ than expected for a 4p-4h excitation. In addition the occupation numbers show that the neutrons are not predominantly excited to the $1g_{7/2}$ orbital as was previously expected based on the large spatial overlap with the proton $1g_{9/2}$ orbital. The structure of the excited state can be understood in terms of a type II shell evolution (cf. Sec. 6.2). The increased number of protons in the $j_>$ orbital $1g_{9/2}$ leads, via the monopole part of the tensor force, to a reduced spin-orbit splitting for neutrons. The large spatial overlap with the proton orbital $1g_{9/2}$ makes this effect especially pronounced for the $1g_{9/2}$-$1g_{7/2}$ neutron orbitals. This increases the likelihood of neutron ph excitations from $1g_{9/2}$ above the subshell closure into the $j_<$ orbitals, which in turn causes an increased likelihood of protons occupying $1g_{9/2}$, because of the attractive nature of the $j_<$-$j_>$ monopole part of the tensor force. Thus, the tensor force leads to a self-reinforcing effect, which stabilizes the deformation. It is worth studying the situation, which is displayed in Fig. 10.4, in greater detail.

The protons being excited to the $1g_{9/2}$ orbital leave holes behind in the pf shell. The orbitals in this shell are predominantly of $j_<$ type ($1f_{5/2}$, $2p_{1/2}$) with only $2p_{3/2}$ being a $j_>$ orbital ($1f_{7/2}$ is not part of the model space). Holes in $j_<$ orbitals have the same effect, as far as the monopole tensor interaction is concerned, as the particles in $j_>$. Thus, the holes in the pf shell will strengthen the effect of the protons in $1g_{9/2}$ and reinforce deformation. However, the occupation numbers can not fully be explained by type II shell evolution alone. Consider the effects of the changed proton occupation numbers on the neutron $1h_{11/2}$ orbital. This orbital is of $j_>$ type and the net monopole tensor interaction should be repulsive pushing the orbital up to a higher ESPE (see Fig. 10.4). This should decrease the likelihood of neutrons occupying the $1h_{11/2}$ orbital, which is in conflict with the higher occupation numbers in comparison to the ground state (cf. Fig. 10.3). A possible explanation of this can be given within the Nilsson model. If the 0_2^+ state and the band build on top of it is deformed the magnetic substates within a given orbital will no longer be degenerate. The energy of a nucleon in a given orbital is different for different projections K of the angular momentum on the symmetry axis of the nucleus. In the limit of small deformation the resulting energy shift in comparison to the spherical ESPE is (see Eq. (8.8) in Casten [122])

$$\Delta E(N,l,j,K) = -\frac{2}{3}\hbar\omega_0\left(N+\frac{3}{2}\right)\delta\,\frac{\left[3K^2-j(j+1)\right]\cdot\left[\frac{3}{4}-j(j+1)\right]}{(2j-1)\,j(j+1)(2j+3)}, \tag{10.10}$$

where N denotes the principal quantum number and δ is a measure of the quadrupole deformation of the nucleus. For the $1h_{11/2}$ orbital and the next orbital below it the maximum shifts can be estimated to be

$$\Delta E\left(1h_{11/2}, K = 1/2\right) \approx -380 \text{ keV} \qquad \Delta E\left(1g_{7/2}, K = 7/2\right) \approx 520 \text{ keV}, \tag{10.11}$$

where the K projection energetically lowered the most has been chosen for $1h_{11/2}$ and the one energetically raised the most has been chosen for $1g_{7/2}$ in order to estimate the maximum relative energy shift. In the calculation the approximations $\hbar\omega_0 \approx 41 \cdot A^{-1/3}$ and $\delta \approx \beta_2 \cdot {}^3/_2 \sqrt{{}^5/_{4\pi}}$ have been used [122]. The quadrupole deformation parameter β_2 is approximated by $\beta_{2,d}$ (Eq. (10.9)). The relative shift of of 900 keV is of the order of the separation of the two orbitals in the spherical case. Thus, it is a reasonable assumption that K splitting could have a significant influence on their occupation numbers. For a quantitative study of this aspect detailed calculations within the Nilsson model are necessary.

The structure of the shell-model states, as given by the occupation numbers, can be used to check the mixing matrix element $V_{\text{mix}} = 76$ keV computed with a simple two state mixing ansatz. If this matrix element is correct one should be able to describe the experimental $B(\text{M1}; 2_2^+ \to 2_1^+)$ value ($\approx 0.14\,\mu_N^2$) by mixing properly chosen unperturbed states with this mixing strength. It was already noted that the experimentally observed mixing is not seen in the shell-model calculation, which shows no mixing between deformed and spherical states. This makes the shell-model states good candidates to approximate the unperturbed states $2_{s,d}^+$. By introducing the appropriate amount of mixing (V_{mix}) these structures should then be able to reproduce the experimental $B(\text{M1})$ value approximately. In general

$$B(\text{M1}; J_i \to J_f) = \frac{1}{2J_i + 1} \mid \langle J_f \mid \hat{T}^{\text{M1}} \mid J_i \rangle \mid^2, \tag{10.12}$$

with the initial and final states with spin J_i and J_f. Because the M1 transition operator does not connect the unmixed structures, the calculation of the matrix element $\langle 2_1^+ \mid \hat{T}^{\text{M1}} \mid 2_2^+ \rangle$ reduces to the calculation of the diagonal matrix elements $\langle 2_s^+ \mid \hat{T}^{\text{M1}} \mid 2_s^+ \rangle$ and $\langle 2_d^+ \mid \hat{T}^{\text{M1}} \mid 2_d^+ \rangle$ (see appendix F for details). Assuming the dominant configuration of 2_s^+ to be $\left(\nu - 2d_{5/2}^{-1}\, \nu - 3s_{1/2}^1\right)$, as suggested by the occupation numbers (Fig. 10.3), and using the collective model g factor ($\approx {}^Z/_A$) to calculate the matrix element of 2_d^+, one obtains

$$\begin{aligned}
B(\text{M1}; 2_2^+ \to 2_1^+) &= \frac{1}{5} \mid \langle 2_1^+ \mid \hat{T}^{\text{M1}} \mid 2_2^+ \rangle \mid^2 && (10.13)\\
&= \frac{3}{2}\alpha^2\beta^2 \mid \langle 2_d^+ \mid \hat{T}^{\text{M1}} \mid 2_d^+ \rangle + \langle 2_s^+ \mid \hat{T}^{\text{M1}} \mid 2_s^+ \rangle \mid^2 && (10.14)\\
&\approx \frac{3}{2}\alpha^2\beta^2 \mid \frac{5}{6}\mu_N + 0.62\,\mu_N \mid^2 && (10.15)\\
&\approx 0.08\,\mu_N^2, && (10.16)
\end{aligned}$$

where α and β are the mixing amplitudes given by Eq. (10.5). This estimation of the $B(\text{M1}; 2_2^+ \to 2_1^+)$ value is close to the experimentally observed $B(\text{M1}; 2_2^+ \to 2_1^+) = \left(0.14^{+0.05}_{-0.04}\right)\,\mu_N^2$ value, which suggests that the mixing matrix element of $V_{\text{mix}} = 76$ keV is a reasonable description of the mixing of spherical and deformed structures in ^{96}Zr.

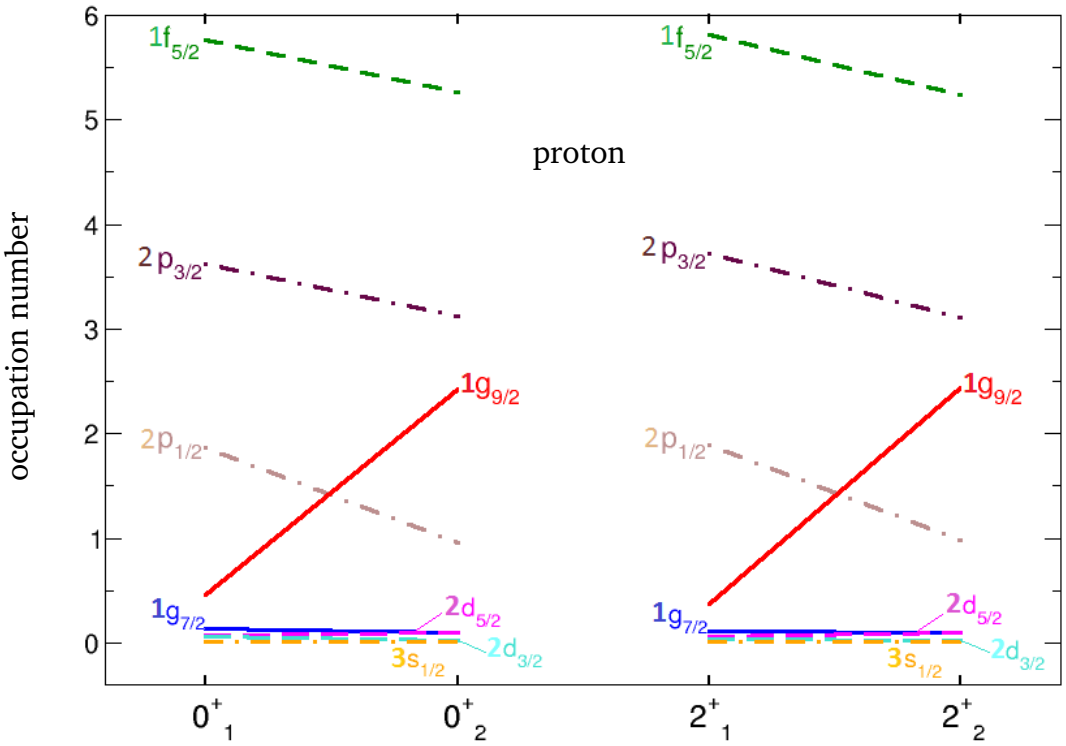

(a) Proton occupation numbers.

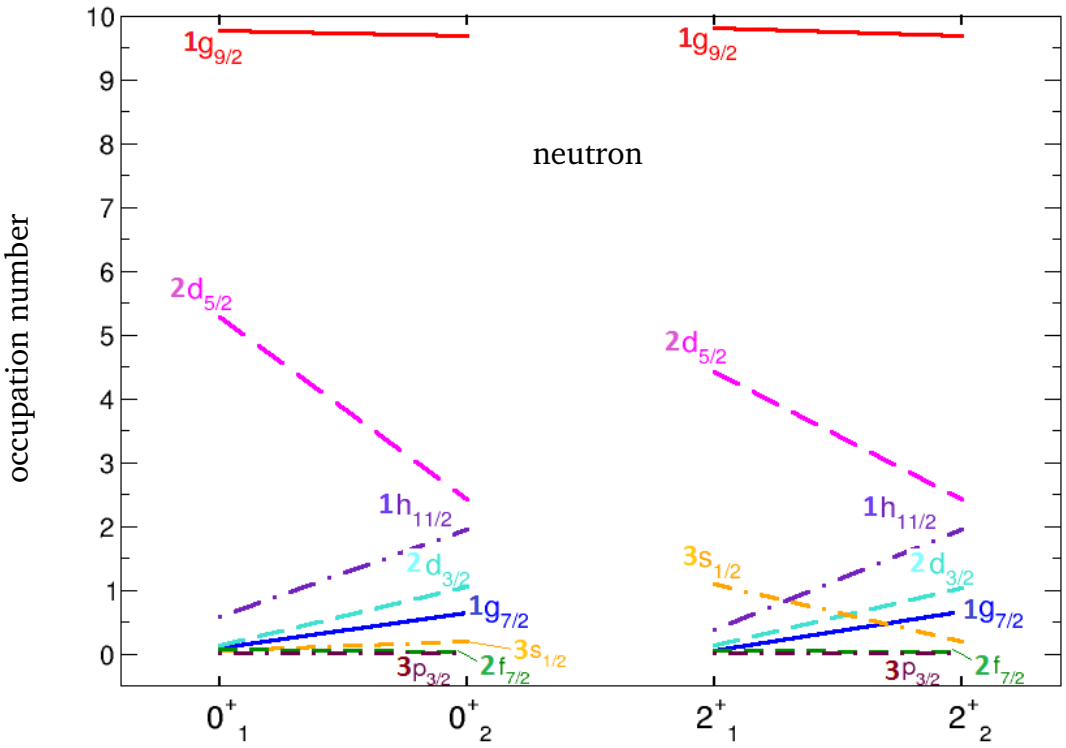

(b) Neutron occupation numbers.

Figure 10.3.: Occupation numbers for the full model space of the shell model calculation for ^{96}Zr. Figures adopted from Otsuka [178].

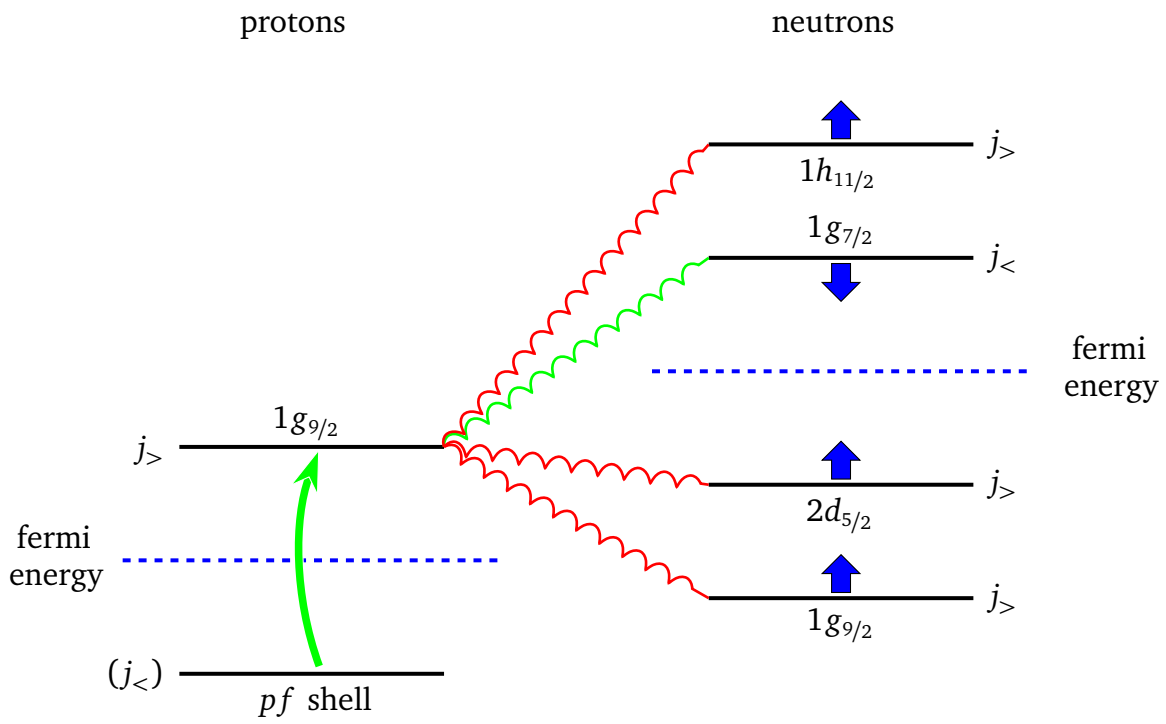

Figure 10.4.: Schematic illustration of type II shell evolution in ^{96}Zr. The bend green arrow represent the particle-hole excitation for the 0_2^+ state. The blue arrows represent the shift in the neutron ESPEs caused by the change in proton occupation numbers. Curled lines represent repulsive (red) or attractive (green) monopole tensor force interactions. Blue dashed lines represent the fermi energy.

11 Summary and outlook

In this work inelastic electron scattering off ^{96}Zr is studied. The experiment has been performed at the high-resolution Linttot spectrometer at the S-DALINAC. Data were taken at scattering angles of 81°, 93°, 117°, and 141°. The measurement at 117° was conducted with a beam energy of 69 MeV while the other measurements were performed at 43 MeV. The covered momentum transfer (q) values are $q = 0.59\,\mathrm{fm}^{-1}$, $q = 0.40\,\mathrm{fm}^{-1}$, $q = 0.31\,\mathrm{fm}^{-1}$, and $q = 0.28\,\mathrm{fm}^{-1}$.

With the obtained experimental data the determination of $B(\mathrm{E2}; 2_2^+ \rightarrow 0_1^+) = \left(0.26^{+0.09}_{-0.07}\right)$ W.u. was possible in a relative PWBA analysis. This method reduces the model dependence compared to the standard DWBA analysis and is well suited to achieve high precision. The experimental uncertainty is mainly caused by the narrow momentum transfer range covered in the experiment. A single additional measurement at higher q, which could be conducted within a future experimental campaign at the Lintott spectrometer, would significantly reduce the uncertainty. By using the extracted $B(\mathrm{E2}; 2_2^+ \rightarrow 0_1^+)$ value with known multipole mixing ratios and branching ratios all decay strengths of the 2_2^+ state are determined. The large $B(\mathrm{E2}; 2_2^+ \rightarrow 0_2^+) = \left(35.6^{+12.5}_{-9.8}\right)$ W.u. value shows the 2_2^+ state to be a collective excitation build on top of the 0_2^+ state.

This transition strength, in addition to the low transition strengths of the 0_2^+ and 2_2^+ states to the ground-state band, suggest different underlying structures. The ground-state band possesses a spherical structure whereas the 0_2^+ state is the head of a collective deformed band. The determined $B(\mathrm{E2}; 2_2^+ \rightarrow 0_2^+)$ value is taken as input for a mixing calculation along with the previously known $B(\mathrm{E2}; 2_1^+ \rightarrow 0_1^+)$ value and energies of the 0_1^+, 0_2^+, 2_1^+, and 2_2^+ state. The results of this mixing calculation show that there is little mixing between the two bands ($V_{\mathrm{mix}} = 76$ keV). The 0^+ states are particularly pure manifestations of the underlying structures (99.8 %) with only a small admixture (0.2 %). The 2^+ states show slightly stronger mixing containing 97.5 % of the dominant structure and an admixture of 2.5 %.

This situation is qualitatively reproduced by a shell-model calculation. The occupation numbers give a clear indication that the underlying structures are stabilized via type II shell evolution. For the ground state there are, to good approximation, no excitations above the $Z = 40$ and $N = 56$ subshell closures. The structure of the 0_2^+, which is deformed in the shell-model calculations, is significantly different from that of the ground state. The occupation numbers reveal on average five particles excited above the subshell closures at $Z = 40$ and $N = 56$. Two protons are excited from the pf shell into the $1g_{9/2}$ orbital. This reduces the spin-orbit splitting for the neutrons, via the monopole part of the tensor force, and leads to neutron excitations above the subshell gap. These excitations in turn favor protons in $1g_{9/2}$ and, thus, lead to a self-reinforcing stabilization of the deformed 0_2^+ state.

Shell-model calculations for this nucleus are still ongoing and should give further insight into the structure of ^{96}Zr and the development of deformation towards the neutron richer Zr isotopes. Of particular interest are the ESPEs of the involved orbitals for both the 0_1^+ and 0_2^+ state. Calculation of the ESPEs will allow a quantification of the tensor force effect on the single particle energies. Furthermore, calculations within the Nilsson model could prove to be helpful in explaining the increased occupation probability of the neutron $1h_{11/2}$ orbital in the deformed states.

The study of ^{96}Zr in this work is the first example of type II shell evolution in the $A \approx 100$ mass region. Thus, it can only be seen as a starting point to study the importance of the shell evolution for the onset and stabilization of deformation in the Zr isotopes, in particular, and the whole $A \approx 100$ mass region, in general.

In addition, the obtained quantitative data on transition strengths and the qualitative information about the structure of ^{96}Zr provides additional quantities which can be used to test models of nuclear structure. This data is especially useful, because ^{96}Zr shows large octupole collectivity, which was already difficult to describe for many models. The experimental confirmation of the intruder band as another low-energy collective structure of ^{96}Zr establishes this nucleus as an important and very sensitive testing ground for the validity of any model aiming to describe collectivity in the $A \approx 100$ mass region.

A Details of the IBM calculation with ArbModel

A.1 σ fluctuations

In order to calculate the σ fluctuations (Eq. (3.6)) with ArbModel [94] several things have to be taken into account. ArbModel takes the Hamiltonian as an input and computes energies and wave functions from it. The Hamiltonian has to be given in terms of elementary boson operators coupled to $L = 0$. Thus, the ECQF Hamiltonian defined in Eq. (2.18) has to be rewritten in terms of boson operators only. Using the definition of the scalar product for tensors (Eq. (2.17)) yields the appropriate input format for the calculation

$$\begin{aligned}\hat{H}_{ECQF} = \sqrt{5}\,\omega(1-\xi)\left[\hat{d}^\dagger \times \tilde{d}\right]_0^{(0)} - \sqrt{5}\,\frac{\xi\,\omega}{4N}\cdot\Bigg(&\left[\left[\hat{s}^\dagger \times \tilde{d}\right]^{(2)} \times \left[\hat{s}^\dagger \times \tilde{d}\right]^{(2)}\right]_0^{(0)} \\ &+ \left[\left[\hat{s}^\dagger \times \tilde{d}\right]^{(2)} \times \left[\hat{d}^\dagger \times \tilde{s}\right]^{(2)}\right]_0^{(0)} + \left[\left[\hat{d}^\dagger \times \tilde{s}\right]^{(2)} \times \left[\hat{s}^\dagger \times \tilde{d}\right]^{(2)}\right]_0^{(0)} \\ &+ \left[\left[\hat{d}^\dagger \times \tilde{s}\right]^{(2)} \times \left[\hat{d}^\dagger \times \tilde{s}\right]^{(2)}\right]_0^{(0)} + \chi\left[\left[\hat{d}^\dagger \times \tilde{d}\right]^{(2)} \times \left[\hat{s}^\dagger \times \tilde{d}\right]^{(2)}\right]_0^{(0)} \\ &+ \chi\left[\left[\hat{d}^\dagger \times \tilde{d}\right]^{(2)} \times \left[\hat{d}^\dagger \times \tilde{s}\right]^{(2)}\right]_0^{(0)} + \chi\left[\left[\hat{s}^\dagger \times \tilde{d}\right]^{(2)} \times \left[\hat{d}^\dagger \times \tilde{d}\right]^{(2)}\right]_0^{(0)} \\ &+ \chi\left[\left[\hat{d}^\dagger \times \tilde{s}\right]^{(2)} \times \left[\hat{d}^\dagger \times \tilde{d}\right]^{(2)}\right]_0^{(0)} + \chi^2\left[\left[\hat{d}^\dagger \times \tilde{d}\right]^{(2)} \times \left[\hat{d}^\dagger \times \tilde{d}\right]^{(2)}\right]_0^{(0)}\Bigg)\end{aligned} \tag{A.1}$$

where $\tilde{s} = \hat{s}$ has been used. From this Hamiltonian the wave functions can be calculated. ArbModel provides the resulting wave functions in $U(5)$ basis decomposition. In order to calculate $\Delta\sigma$ these results have to be transformed to the $O(6)$ DS limit basis. Thus, one needs to compute the $U(5)$ basis representation of the $O(6)$ basis states. The easiest way to do this is to just use $\hat{H}_{ECQF}(\xi = 1, \chi = 0)$ as input for ArbModel. The ECQF Hamiltonian is exactly $O(6)$ symmetric for $\xi = 1$ and $\chi = 0$ and the resulting wave functions are $O(6)$ basis states. Using the analytical expression for the excitation energies in the $O(6)$ DS, as defined in Eq. (2.27), the quantum numbers for all the $O(6)$ basis states can be identified. With this information $\Delta\sigma$ can be calculated according to Eq. (3.6).

A.2 Overlap of ground-state wave functions

To calculate overlaps of the 0_1^+ wave functions of $\hat{H}_{ECQF}$ and $\hat{H}_M$, as defined in Eq. (3.7), the Hamiltonians have to be written in terms of boson operators. For $\hat{H}_{ECQF}$ this was already done in Eq. (A.1). Doing the same for $\hat{H}_M$ yields

$$\begin{aligned}
\hat{H}_M = -\sqrt{5}\Big(&\Big[\Big[\hat{s}^\dagger \times \tilde{d}\Big]^{(2)} \times \Big[\hat{s}^\dagger \times \tilde{d}\Big]^{(2)}\Big]_0^{(0)} + \Big[\Big[\hat{s}^\dagger \times \tilde{d}\Big]^{(2)} \times \Big[\hat{d}^\dagger \times \tilde{s}\Big]^{(2)}\Big]_0^{(0)} \\
&+ \Big[\Big[\hat{d}^\dagger \times \tilde{s}\Big]^{(2)} \times \Big[\hat{s}^\dagger \times \tilde{d}\Big]^{(2)}\Big]_0^{(0)} + \Big[\Big[\hat{d}^\dagger \times \tilde{s}\Big]^{(2)} \times \Big[\hat{d}^\dagger \times \tilde{s}\Big]^{(2)}\Big]_0^{(0)}\Big) \\
&+ 2\sqrt{3}\Big[\Big[\hat{d}^\dagger \times \tilde{d}\Big]^{(1)} \times \Big[\hat{d}^\dagger \times \tilde{d}\Big]^{(1)}\Big]_0^{(0)} + 2\sqrt{7}\Big[\Big[\hat{d}^\dagger \times \tilde{d}\Big]^{(3)} \times \Big[\hat{d}^\dagger \times \tilde{d}\Big]^{(3)}\Big]_0^{(0)} \\
&+ 4\Big[\hat{s}^\dagger \times \tilde{s}\Big]_0^{(0)} + 4\sqrt{5}\Big[\hat{d}^\dagger \times \tilde{d}\Big]_0^{(0)} + \Big[\Big[\hat{s}^\dagger \times \tilde{s}\Big]^{(0)} \times \Big[\hat{s}^\dagger \times \tilde{s}\Big]^{(0)}\Big]_0^{(0)} \\
&+ 5\Big[\Big[\hat{d}^\dagger \times \tilde{d}\Big]^{(0)} \times \Big[\hat{d}^\dagger \times \tilde{d}\Big]^{(0)}\Big]_0^{(0)} + 4\alpha\sqrt{3}\Big[\Big[\hat{d}^\dagger \times \tilde{d}\Big]^{(1)} \times \Big[\hat{d}^\dagger \times \tilde{d}\Big]^{(1)}\Big]_0^{(0)} \\
&- 4\alpha\sqrt{7}\Big[\Big[\hat{d}^\dagger \times \tilde{d}\Big]^{(3)} \times \Big[\hat{d}^\dagger \times \tilde{d}\Big]^{(3)}\Big]_0^{(0)} - 4\alpha\sqrt{5}\Big[\hat{d}^\dagger \times \tilde{d}\Big]_0^{(0)} \\
&+ 2\alpha\sqrt{5}\Big[\Big[\hat{d}^\dagger \times \tilde{d}\Big]^{(0)} \times \Big[\hat{s}^\dagger \times \tilde{s}\Big]^{(0)}\Big]_0^{(0)} + 10\alpha\Big[\Big[\hat{d}^\dagger \times \tilde{d}\Big]^{(0)} \times \Big[\hat{d}^\dagger \times \tilde{d}\Big]^{(0)}\Big]_0^{(0)} \\
&+ \alpha\sqrt{70}\Big(\Big[\Big[\hat{d}^\dagger \times \tilde{s}\Big]^{(2)} \times \Big[\hat{d}^\dagger \times \tilde{d}\Big]^{(2)}\Big]_0^{(0)} + \Big[\Big[\hat{s}^\dagger \times \tilde{d}\Big]^{(2)} \times \Big[\hat{d}^\dagger \times \tilde{d}\Big]^{(2)}\Big]_0^{(0)}\Big) \\
&+ 10\alpha\sqrt{3}\Big[\Big[\hat{d}^\dagger \times \tilde{d}\Big]^{(1)} \times \Big[\hat{d}^\dagger \times \tilde{d}\Big]^{(1)}\Big]_0^{(0)}. \qquad \text{(A.2)}
\end{aligned}$$

This Hamiltonian can now be used as an input for ArbModel and the overlap of the ground-state wave function with the ground-state wave function of $\hat{H}_{ECQF}$ can be calculated according to Eq. (3.8). Note again, that ArbModel returns wave functions in $U(5)$ basis. This means in order to calculate the overlap one has to sum over all possible $U(5)$ basis states.

B Fluctuations of σ for $L = 0,\ 2,\ 4,$ and 6 yrast states

This section shows numerically calculated σ fluctuations (according to Eq. (3.6)) for members of the ground-state band with $L > 0$ for $N = 8$ valence bosons. The whole parameter space of the ECQF Hamiltonian (Eq. (2.18)) is covered. Calculations have been performed using ArbModel [94].

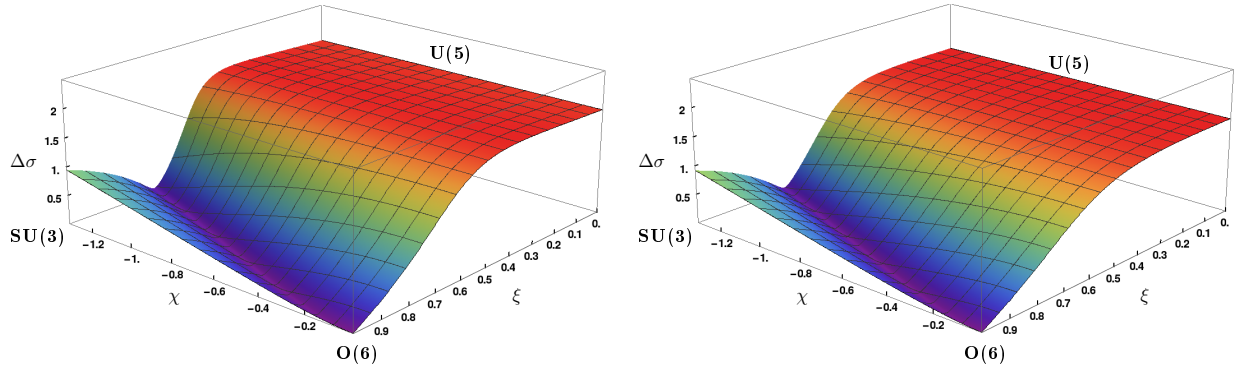

(a) 0_1^+ (b) 2_1^+

(c) 4_1^+ (d) 6_1^+

Figure B.1.: Fluctuations of σ for $L = 0,\ 2,\ 4,$ and 6 yrast states of $\hat{H}_{ECQF}$. With increasing spin L the magnitude of $\Delta\sigma$ decreases in the whole triangle, because the possible $O(6)$ basis states that can be part of a given state decreases with increasing L. For a detailed discussion see chapter 3.1.

C ECQF energy surface

The calculation of the most general IBM Hamiltonian $\hat{H}_{NO}$ with up to two-body interactions in normal ordered form has been solved by Macek and Leviatan [85] and the result is given in Eq. (2.39). This reduces the calculation for any subsequent IBM Hamiltonian to normal ordering it and then comparing coefficients to relate the parameters to those of the normal ordered Hamiltonian given by

$$\begin{aligned}\hat{H}_{NO} = \epsilon_s\, \hat{s}^\dagger \tilde{s} + \epsilon_d\, \hat{d}^\dagger \cdot \tilde{d} + u_0 \left(\hat{s}^\dagger\right)^2 \tilde{s}^2 + u_2\, \hat{s}^\dagger\, \hat{d}^\dagger \cdot \tilde{d}\, \tilde{s} + v_0 \left[\left(s^\dagger\right)^2 \tilde{d} \cdot \tilde{d} + d^\dagger \cdot d^\dagger\, (s)^2\right] \\ + v_2 \left[s^\dagger\, d^\dagger \cdot \left(\tilde{d}\, \tilde{d}\right)^{(2)} + \left(d^\dagger\, d^\dagger\right)^{(2)} \cdot \hat{s}\, \tilde{d}\right] + \sum_{L=0,2,4} c_L \left(d^\dagger\, d^\dagger\right)^{(L)} \cdot \left(\tilde{d}\, \tilde{d}\right)^{(L)}, \quad \text{(C.1)}\end{aligned}$$

where $\left(d^\dagger\, d^\dagger\right)^{(L)}$ is an equivalent notation for $\left[d^\dagger \times d^\dagger\right]^{(L)}$. The parameters a, b, and c of Eq. (2.39) are related to those of $\hat{H}_{NO}$ in the large N limit [85]:

$$a = u_2 + 2\, v_0 - 2\, u_0 + \frac{\epsilon_d - \epsilon_s}{N}, \quad \text{(C.2)}$$

$$b = 2\, v_2 \sqrt{\frac{2}{7}}, \quad \text{(C.3)}$$

$$c = \frac{1}{5} c_0 + \frac{2}{7} c_2 + \frac{18}{35} c_4 + \frac{\epsilon_d - \epsilon_s}{N}. \quad \text{(C.4)}$$

The Hamiltonian of the ECQF contains two terms, where

$$\hat{n}_d = \hat{d}^\dagger \cdot \tilde{d} \quad \text{(C.5)}$$

is already given in normal order. For the second term one finds

$$\begin{aligned}\hat{Q}^\chi \cdot \hat{Q}^\chi = \\ \left(\left[\hat{s}^\dagger \times \tilde{d} + \hat{d}^\dagger \times \hat{s}\right]^{(2)} + \chi \cdot \left[\hat{d}^\dagger \times \tilde{d}\right]^{(2)}\right) \cdot \left(\left[\hat{s}^\dagger \times \tilde{d} + \hat{d}^\dagger \times \hat{s}\right]^{(2)} + \chi \cdot \left[\hat{d}^\dagger \times \tilde{d}\right]^{(2)}\right). \quad \text{(C.6)}\end{aligned}$$

In order to rewrite this in normal ordered form one uses the scalar product (Eq. (2.17)), the angular momentum coupling (Eq. (2.7)), the commutation relations defined in Eqs. (2.2) to (2.6), and the relation $\tilde{d}_\mu = (-1)^\mu\, \hat{d}_{-\mu}$ [37]. With this the first part of $\hat{Q}^\chi$ can be rewritten:

$$\left[\hat{s}^\dagger \times \tilde{d} + \hat{d}^\dagger \times \hat{s}\right]^{(2)} = \left[s^\dagger \times \tilde{d}\right]^{(2)} + \left[\hat{d}^\dagger \times \hat{s}\right]^{(2)} \quad \text{(C.7)}$$

$$= s^\dagger\, \tilde{d} + \hat{d}^\dagger\, \hat{s}. \quad \text{(C.8)}$$

Now the terms of $\hat{Q}^\chi \cdot \hat{Q}^\chi$ can be brought into normal ordered form. For the terms containing two s- and two d-bosons this yields

$$\begin{aligned}
\hat{s}^\dagger \tilde{d} \cdot \hat{d}^\dagger \tilde{s} &= \sum_\mu (-1)^\mu \hat{s}^\dagger \tilde{d}_\mu \hat{d}^\dagger_{-\mu} \hat{s} && \text{(C.9)}\\
&= \sum_\mu (-1)^\mu \hat{s}^\dagger (-1)^\mu \hat{d}_{-\mu} \hat{d}^\dagger_{-\mu} \hat{s} && \text{(C.10)}\\
&= \sum_\mu (-1)^\mu \hat{s}^\dagger (-1)^\mu (1 + \hat{d}^\dagger_{-\mu} \hat{d}_{-\mu}) \hat{s} && \text{(C.11)}\\
&= \hat{s}^\dagger \hat{s} + \hat{s}^\dagger \hat{d}^\dagger \cdot \tilde{d}\, \hat{s}, && \text{(C.12)}\\
\hat{s}^\dagger \tilde{d} \cdot \hat{s}^\dagger \tilde{d} &= \left(\hat{s}^\dagger\right)^2 \tilde{d} \cdot \tilde{d}, && \text{(C.13)}\\
\hat{d}^\dagger \hat{s} \cdot \hat{s} \tilde{d} &= \hat{d}^\dagger \cdot \tilde{d} + \hat{d}^\dagger \hat{s}^\dagger \cdot \tilde{d}\, \hat{s}, && \text{(C.14)}\\
\hat{d}^\dagger \hat{s} \cdot \hat{d}^\dagger \hat{s} &= \hat{d}^\dagger \cdot \hat{d}^\dagger \, (\hat{s})^2, && \text{(C.15)}
\end{aligned}$$

where the calculations of the last three terms are similar to the one of the first. The next step are the terms containing three d-bosons and one s-boson:

$$\begin{aligned}
\hat{d}^\dagger \hat{s} \cdot \left[\hat{d}^\dagger \times \tilde{d}\right]^{(2)} &= \sum_\mu (-1)^\mu \hat{d}^\dagger_\mu \hat{s} \left[\hat{d}^\dagger \times \tilde{d}\right]^{(2)}_{-\mu} && \text{(C.16)}\\
&= \sum_\mu (-1)^\mu \hat{d}^\dagger_\mu \hat{s} \sum_{a,\,b} C^{2,-\mu}_{2,a,2,b} \hat{d}^\dagger_a \tilde{d}_b && \text{(C.17)}\\
&= \sum_{\mu,\,a,\,b} (-1)^{-\mu-a} C^{2,-b}_{2,a,2,\mu} \hat{d}^\dagger_\mu \hat{d}^\dagger_a \hat{s}\, \tilde{d}_b && \text{(C.18)}\\
&= \sum_b (-1)^b \left[\hat{d}^\dagger \times \hat{d}^\dagger\right]^{(2)}_{-b} \hat{s}\, \tilde{d}_b && \text{(C.19)}\\
&= \sum_b (-1)^b \left[\hat{d}^\dagger \times \hat{d}^\dagger\right]^{(2)}_{b} \hat{s}\, \tilde{d}_{-b} && \text{(C.20)}\\
&= \left(\hat{d}^\dagger \hat{d}^\dagger\right)^{(2)} \cdot \hat{s}\, \tilde{d}, && \text{(C.21)}\\
\hat{s}^\dagger \tilde{d} \cdot \left[\hat{d}^\dagger \times \tilde{d}\right]^{(2)} &= \hat{s}^\dagger \hat{d}^\dagger \cdot \left(\tilde{d}\, \tilde{d}\right)^{(2)}, && \text{(C.22)}\\
\left[\hat{d}^\dagger \times \tilde{d}\right]^{(2)} \cdot \hat{s}^\dagger \tilde{d} &= \hat{s}^\dagger \hat{d}^\dagger \cdot \left(\tilde{d}\, \tilde{d}\right)^{(2)}, && \text{(C.23)}\\
\left[\hat{d}^\dagger \times \tilde{d}\right]^{(2)} \cdot \hat{d}^\dagger \hat{s} &= \left(\hat{d}^\dagger \hat{d}^\dagger\right)^{(2)} \cdot \hat{s}\, \tilde{d}, && \text{(C.24)}
\end{aligned}$$

where the symmetry properties of the Clebsch-Gordan coefficients [182] have been used. The calculations for the last three terms are similar to the calculation of the first. Finally, the term with four d-bosons has to be considered. A two particle state with two particles of angular momentum j_1, j_2 and magnetic substates m_1 and m_2 will be denoted as $|j_1\, m_1\, j_2\, m_2\rangle$. A two particle state, where the particles are coupled to total angular momentum J and M will be denoted as $|j_1\, j_2\, J\, M\rangle = |J\, M\rangle$. The Clebsch-Gordan coefficients can then be written as

$$C^{J,M}_{j_1,m_1,j_2,m_2} = \langle j_1\, m_1\, j_2\, m_2 \,|\, J\, M\rangle. \qquad \text{(C.25)}$$

With these notations the four d-boson term can be normal ordered:

$$\left[\hat{d}^\dagger \times \tilde{d}\right]^{(2)} \cdot \left[\hat{d}^\dagger \times \tilde{d}\right]^{(2)} \tag{C.26}$$

$$= \sum_M (-1)^M \left[\hat{d}^\dagger \times \tilde{d}\right]^2_M \left[\hat{d}^\dagger \times \tilde{d}\right]^2_{-M} \tag{C.27}$$

$$= \sum_{M,a,b,c,d} (-1)^M \langle 2\,a\,2\,b \mid 2\,M\rangle \langle 2\,c\,2\,d \mid 2\,(-M)\rangle \hat{d}^\dagger_a \tilde{d}_b \hat{d}^\dagger_c \tilde{d}_d \tag{C.28}$$

$$= \sum_{M,a,b,c,d} (-1)^M \langle 2\,a\,2\,b \mid 2\,M\rangle \langle 2\,c\,2\,d \mid 2\,(-M)\rangle \hat{d}^\dagger_a \left(\delta_{b,c} + \hat{d}^\dagger_c \tilde{d}_b\right) \tilde{d}_d \tag{C.29}$$

$$= \sum_{M,a,b,c,d} (-1)^M \langle 2\,a\,2\,b \mid 2\,M\rangle \langle 2\,c\,2\,d \mid 2\,(-M)\rangle \hat{d}^\dagger_a \hat{d}^\dagger_c \tilde{d}_b \tilde{d}_d \tag{C.30}$$

$$= \sum_{M,a,b,c,d} \sum_{J_1,J_2,M_1,M_2} (-1)^M \langle 2\,a\,2\,b \mid 2\,M\rangle \langle 2\,c\,2\,d \mid 2\,(-M)\rangle \langle 2\,a\,2\,c \mid J_1\,M_1\rangle \langle 2\,b\,2\,d \mid J_2\,M_2\rangle \left[\hat{d}^\dagger \times \hat{d}^\dagger\right]^{(J_1)}_{M_1} \left[\tilde{d} \times \tilde{d}\right]^{(J_2)}_{M_2} \tag{C.31}$$

$$= \sum_{M,a,b,c,d} \sum_{J_1,J_2,M_1,M_2} (-1)^M \langle 2\,a\,2\,b \mid 2\,a\,2\,c\rangle \langle 2\,c\,2\,d \mid 2\,b\,2\,d\rangle \langle J_1\,M_1 \mid 2\,M\rangle \langle J_2\,M_2 \mid 2\,(-M)\rangle \left[\hat{d}^\dagger \times \hat{d}^\dagger\right]^{(J_1)}_{M_1} \left[\tilde{d} \times \tilde{d}\right]^{(J_2)}_{M_2} \tag{C.32}$$

$$= \sum_{M,a,b,c,d} (-1)^M \langle 2\,a\,2\,b \mid 2\,a\,2\,c\rangle \langle 2\,c\,2\,d \mid 2\,b\,2\,d\rangle \left[\hat{d}^\dagger \times \hat{d}^\dagger\right]^{(2)}_M \left[\tilde{d} \times \tilde{d}\right]^{(2)}_{-M} \tag{C.33}$$

$$= \sum_{M,a,b,d} (-1)^M \langle 2\,a\,2\,b \mid 2\,a\,2\,b\rangle \langle 2\,b\,2\,d \mid 2\,b\,2\,d\rangle \left[\hat{d}^\dagger \times \hat{d}^\dagger\right]^{(2)}_M \left[\tilde{d} \times \tilde{d}\right]^{(2)}_{-M} \tag{C.34}$$

$$= \sum_M (-1)^M \left[\hat{d}^\dagger \times \hat{d}^\dagger\right]^{(2)}_M \left[\tilde{d} \times \tilde{d}\right]^{(2)}_{-M} \tag{C.35}$$

$$= \left[\hat{d}^\dagger \times \hat{d}^\dagger\right]^{(2)} \cdot \left[\tilde{d} \times \tilde{d}\right]^{(2)}. \tag{C.36}$$

Here, the relation

$$U^{(j_1)}_{m_1} V^{(j_2)}_{m_2} = \sum_{j_3,m_3} \langle j_2\,m_1\,j_2\,m_2 \mid j_3\,m_3\rangle \left[U^{(j_1)} \times V^{(j_2)}\right]^{(j_3)}_{m_3} \tag{C.37}$$

was used. It can be derived from angular momentum coupling (Eq. (2.7)) in conjunction with the orthogonality relations of the Clebsch-Gordan coefficients [182]. Combining all these results one can write $\hat{H}_{ECQF}$ in normal order

$$\begin{aligned}\hat{H}_{ECQF} = &-\frac{\omega\,\xi}{4N}\hat{s}^\dagger\tilde{s} + \left(\omega\,(1-\xi) - \frac{\omega\,\xi}{4N}\right)\hat{d}^\dagger\cdot\tilde{d} - \frac{\omega\,\xi}{2N}\hat{s}^\dagger\hat{d}^\dagger\cdot\tilde{d}\,\tilde{s} \\ &- \frac{\omega\,\xi}{4N}\left[\left(\hat{s}^\dagger\right)^2\tilde{d}\cdot\tilde{d} + \hat{d}^\dagger\cdot\hat{d}^\dagger\,(\hat{s})^2\right] - \frac{\omega\,\xi\,\chi}{2N}\left[\hat{s}^\dagger\hat{d}^\dagger\cdot\left(\tilde{d}\,\tilde{d}\right)^{(2)} + \left(\hat{d}^\dagger\,\hat{d}^\dagger\right)^{(2)}\cdot\hat{s}\,\tilde{d}\right] \\ &- \frac{\omega\,\xi\,\chi^2}{4N}\left(\hat{d}^\dagger\,\hat{d}^\dagger\right)^{(2)}\cdot\left(\tilde{d}\,\tilde{d}\right)^{(2)}.\end{aligned} \tag{C.38}$$

Comparing coefficients with Eq. (C.1) yields the parameters of $\hat{H}_{NO}$ expressed in terms of the parameters of $\hat{H}_{ECQF}$:

$$\epsilon_s = -\frac{\omega\xi}{4N}, \tag{C.39}$$

$$\epsilon_d = \omega(1-\xi) - \frac{\omega\xi}{4N}, \tag{C.40}$$

$$u_0 = 0, \tag{C.41}$$

$$u_2 = -\frac{\omega\xi}{2N}, \tag{C.42}$$

$$v_0 = -\frac{\omega\xi}{4N}, \tag{C.43}$$

$$v_2 = -\frac{\omega\xi\chi}{2N}, \tag{C.44}$$

$$c_0 = c_4 = 0, \tag{C.45}$$

$$c_2 = -\frac{\omega\xi\chi^2}{4N}. \tag{C.46}$$

Now the desired relations of the ECQF parameters to a, b, and c can be derived as

$$a = \frac{\omega}{N}(1-2\xi), \tag{C.47}$$

$$b = -\frac{\omega\xi\chi}{N}\sqrt{\frac{2}{7}}, \text{ and} \tag{C.48}$$

$$c = \frac{\omega}{N}\left(1-\xi-\frac{\xi\chi^2}{14}\right). \tag{C.49}$$

With these relations the ECQF energy surface (Eq. (2.39)) can be explicitly calculated for any values of ω, χ, and ξ.

D Matrix elements of $\hat{s}^\dagger$ and $\tilde{s}$ in the $O(6)$ DS limit basis

For the comparison of the IBM prediction with experimental data it is necessary to evaluate matrix elements of $\hat{s}^\dagger$ and $\tilde{s}$ between states of the $O(6)$ DS limit basis with $\sigma = \sigma_{\max}$. The calculation is simplified by expanding the $O(6)$ basis states according to Eq. (2.24) using the transformation brackets given in Eq. (2.25). This reduces the problem to matrix elements between $U(5)$ basis states, which are separated into a s-boson wave function and a d-boson wave function (Eq. (3.24)). Only matrix elements of $\hat{s}^\dagger$ will be stated. Those of $\tilde{s}$ can be obtained by noting, that

$$\langle N+1, \sigma = N+1, \tau \,|\, \hat{s}^\dagger \,|\, N, \sigma = N, \tau \rangle = \langle N, \sigma = N, \tau \,|\, \tilde{s} \,|\, N+1, \sigma = N+1, \tau \rangle. \tag{D.1}$$

The selection rules (Eq. (3.17)) apply and only the allowed matrix elements will be stated. For $\tau = 0$ to $\tau = 0$ transitions the matrix elements can be given analytically:

$$\langle N+1, \sigma = N+1, \tau = 0 \,|\, \hat{s}^\dagger \,|\, N, \sigma = N, \tau = 0 \rangle = \sqrt{\frac{(N+1)(N+4)}{2(N+2)}}. \tag{D.2}$$

For $\tau \neq 0$ no such analytical expression exists. The matrix elements calculated in this work are explicitly given in Tab. D.1.

Table D.1.: Matrix elements of $\hat{s}^\dagger$ in the $O(6)$ DS limit basis for states with $\sigma = \sigma_{\max}$. The $O(6)$ basis states are labeled $|\, \sigma, \tau \rangle$. Matrix elements of $\tilde{s}$ can be obtained via Eq. (D.1).

N	$\langle N+1, \tau = 3 \,\|\, \hat{s}^\dagger \,\|\, N, \tau = 3 \rangle$	$\langle N+1, \tau = 6 \,\|\, \hat{s}^\dagger \,\|\, N, \tau = 6 \rangle$
11	$\sqrt{\frac{82}{13}}$	$\sqrt{\frac{63}{13}}$
12	$\sqrt{\frac{95}{14}}$	$\sqrt{\frac{77}{14}}$
13	$\sqrt{\frac{110}{15}}$	$\sqrt{\frac{92}{15}}$
14	$\sqrt{\frac{126}{16}}$	$\sqrt{\frac{108}{16}}$
15	$\sqrt{\frac{143}{17}}$	$\sqrt{\frac{125}{17}}$

The regularity of these matrix elements implies a generalization of Eq. (D.2) to the $\tau \neq 0$ cases as

$$\langle N+1, \sigma = N+1, \tau \,|\, \hat{s}^\dagger \,|\, N, \sigma = N, \tau \rangle = \sqrt{\frac{(N-\tau+1)(N+\tau+4)}{2(N+2)}}. \tag{D.3}$$

This formular (emperically) reproduces the matrix elements of Tab. D.1 and reduces to Eq. (D.2) in the $\tau = 0$ case. It can be derived using the appropriate isoscalar factors for $U(6) \supset O(6)$ and for $O(6) \supset O(5)$ [183].

E Shell model calculation

The effective interaction of the shell model calculation (see Ch. 10 for a discussion) has been tuned to reproduce the energies of the 2_1^+ state of the Zr isotopic chain. The results of this optimization are shown in Fig. E.1.

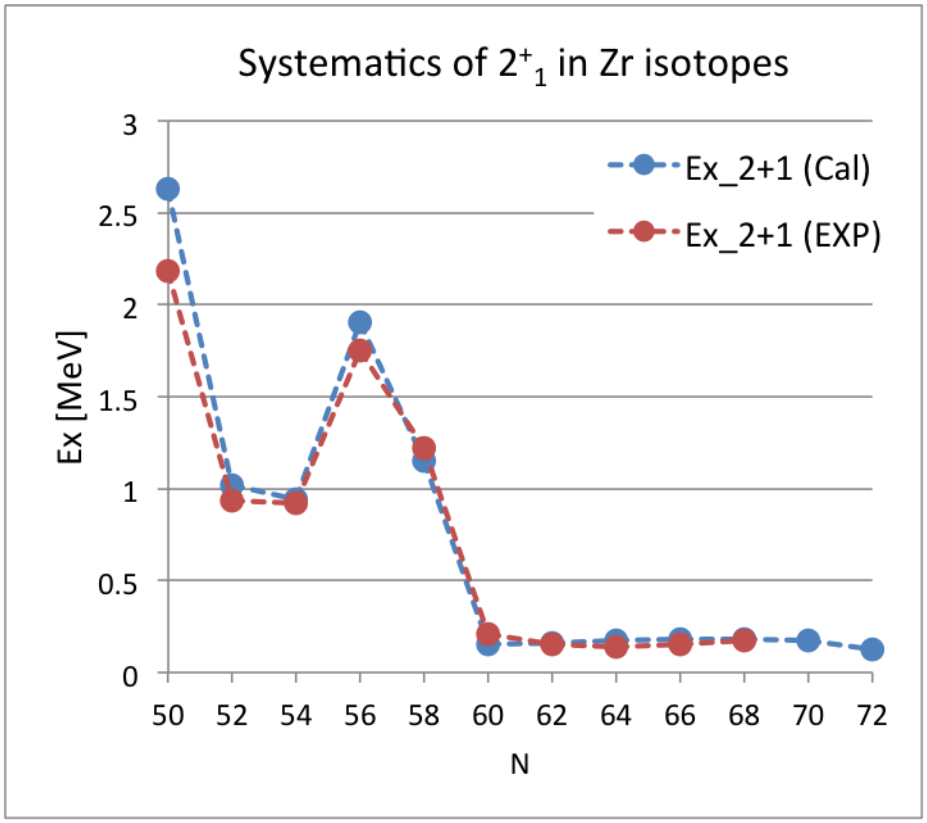

Figure E.1.: Comparison of shell model $E(2_1^+)$ to experimental values for the Zr isotopic chain. Figure adopted from Otsuka [178].

F $B(\mathbf{M}1; 2_2^+ \to 2_1^+)$ estimate

The $B(\mathrm{M1}; J_i \to J_f)$ value is connected to the reduced matrix element by

$$B(\mathrm{M1}; J_i \to J_f) = \frac{1}{2J_i + 1} \mid \langle J_f \mid \hat{T}^{\mathrm{M1}} \mid J_i \rangle \mid^2 . \tag{F.1}$$

Using the Wigner-Eckart theorem (Eq. (15.3.18) of Shankar [184]) the reduced matrix element can be calculated via an angle dependent matrix element:

$$\langle J_f \mid \hat{T}^{\mathrm{M1}} \mid J_i \rangle = \sqrt{2J_f + 1} \left(C^{J_f, m_f}_{J_i, m_i, \lambda, \mu} \right)^{-1} \langle J_f, m_f \mid \hat{T}^{\mathrm{M1}}_{\mu} \mid J_i, m_i \rangle, \tag{F.2}$$

where $m_{i,f}$ denote the initial and final magnetic substates, $C^{J_f, m_f}_{J_i, m_i, \lambda, \mu}$ is a Clebsch-Gordan coefficient (cf. Eq. (C.25)), and the angle independence of the reduced matrix element is implicit. For the transition of the 2_2^+ state to the 2_1^+ state via an M1 transition it is $J_f = J_i = 2$ and $\lambda = 1$. The right-hand side of the equation can be evaluated for any combination of magnetic substates μ, $m_{i,f}$. By choosing $\mu = 0$, which does not connect different magnetic substates $m_{i,f}$, the equation simplifies. Let then be $m_i = m_f = 2$. In this case Eq. (F.2) is given by

$$\langle 2_1^+ \mid \hat{T}^{\mathrm{M1}} \mid 2_2^+ \rangle = \sqrt{5} \sqrt{\frac{3}{2}} \langle 2_1^+, 2 \mid \hat{T}^{\mathrm{M1}}_0 \mid 2_2^+, 2 \rangle \tag{F.3}$$

where the Clebsch-Gordan coefficient $C^{2,2}_{2,2,1,0} = \sqrt{2/3}$ has been used. Explicitly writing the 2^+ states as mixtures of deformed and spherical components yields

$$\langle 2_1^+ \mid \hat{T}^{\mathrm{M1}} \mid 2_2^+ \rangle = \sqrt{5} \sqrt{\frac{3}{2}} \alpha\beta \left(\langle 2^+_{\mathrm{d}}, m_f \mid \hat{T}^{\mathrm{M1}}_0 \mid 2^+_{\mathrm{d}}, m_i \rangle - \langle 2^+_{\mathrm{sph}}, m_f \mid \hat{T}^{\mathrm{M1}}_0 \mid 2^+_{\mathrm{sph}}, m_i \rangle \right), \tag{F.4}$$

where the amplitudes α and β have been calculated before (see Eq. (10.5)) and the M1 transition operator does not allow transitions from the spherical to the deformed structure and vice versa.

The 0-component of the M1 transition operator is

$$\hat{T}^{\mathrm{M1}}_0 = \sqrt{\frac{3}{4\pi}} \left[\left(g_l^{\pi} \cdot \hat{l}_z + g_s^{\pi} \cdot \hat{s}_z \right) \left(\frac{1}{2} - \hat{t}_z \right) + \left(g_l^{\nu} \cdot \hat{l}_z + g_s^{\nu} \cdot \hat{s}_z \right) \left(\frac{1}{2} + \hat{t}_z \right) \right] \mu_N, \tag{F.5}$$

where $\hat{t}_z$ is the z-component of the isospin operator $\hat{t}$ and $\left(0.5 \pm \hat{t}_z\right)$ are neutron and proton projection operators, respectively. The angular momentum g factors g_l^{π} (g_l^{ν}) and the spin g factors g_s^{π} (g_l^{ν}) for protons (neutrons) are given in Tab. F.1.

For the deformed structure the rotational model estimate of the g factor ($\approx Z/A$) can be used to calculate the matrix element:

$$\langle 2^+_{\mathrm{d}}, 2 \mid \hat{T}^{\mathrm{M1}}_0 \mid 2^+_{\mathrm{d}}, 2 \rangle = \frac{2Z}{A} \mu_N = \frac{5}{6} \mu_N. \tag{F.6}$$

Table F.1.: Free proton and neutron g factors. Values adopted from Ref. [185].

	g_l	g_s
proton	1	5.585
neutron	0	-3.82

For the spherical 2^+ state the shell-model calculation (cf. Fig. 10.3) identifies the main component to be

$$|\, 2^+_{\text{sph}},\, m\rangle = |\left(\nu - 2d^{-1}_{5/2},\ \nu - 3s^{1}_{1/2}\right) 2,\, m\rangle. \tag{F.7}$$

The notation on the right-hand side means a coupling of the neutron single hole and single particle states to total spin J and magnetic substate m. There are, to good approximation, no excitations above the proton subshell closure at $Z = 40$. Thus, only neutron particle-hole excitations are taken into consideration from here on. The index ν is dropped for brevity. In this case the transition operator of Eq. (F.5) can be rewritten to only include the parts relevant for neutron excitations:

$$\hat{T}^{\text{M1}}_0 = \sqrt{\frac{3}{4\,\pi}}\ \left(g_s^{\nu} \cdot \hat{s}_z\right) \mu_N, \tag{F.8}$$

where the isospin-projection operator has been dropped for brevity and $g_l^{\nu} = 0$ has been used. Thus, the calculation of the matrix element of $\hat{T}^{\text{M1}}$ simplifies to the evaluation of the expectation value $\hat{s}_z$. For the calculation of this matrix element it is advantageous to transform the coupled particle-hole state of Eq. (F.7) back into the uncoupled two-particle basis. First, the total angular momentum $J = 2$ has to be decoupled into total spin S and total angular momentum L:

$$\begin{aligned}
|\, 2^+_{\text{sph}},\, m\rangle &= |\left(\nu - 2d^{-1}_{5/2},\ \nu - 3s^{1}_{1/2}\right) 2,\, m\rangle && \text{(F.9)}\\
&= |\,[(l_1, l_2)\, L\, m_L\ (s_1, s_2)\, S\, m_S\,]\, J\, M\,\rangle && \text{(F.10)}\\
&= |\left[(2,0)\, 2\, m_L\ \left(\frac{1}{2}, \frac{1}{2}\right) S\, m_S\right] 2\, 2\rangle && \text{(F.11)}\\
&= \sum_{m_L, S, m_S} C^{2,2}_{2, m_L, S, m_S}\ |\,(2,0)\ 2\, m_L\,\rangle\ |\left(\frac{1}{2}, \frac{1}{2}\right) S\, m_S\,\rangle && \text{(F.12)}\\
&= \sqrt{\frac{2}{3}}\ |\,(2,0)\ 2\, 2\rangle\ |\left(\frac{1}{2}, \frac{1}{2}\right) 1\, 0\rangle + |\,(2,0)\ 2\, 2\rangle\ |\left(\frac{1}{2}, \frac{1}{2}\right) 0\, 0\rangle \\
&\quad - \frac{1}{\sqrt{3}}\ |\,(2,0)\ 2\, 1\rangle\ |\left(\frac{1}{2}, \frac{1}{2}\right) 1\, 1\rangle. && \text{(F.13)}
\end{aligned}$$

The sum runs over all possible values for m_L, S, and m_S. In the last step the Clebsch-Gordan coefficients have been explicitly evaluated. In order to evaluate the matrix element of $\hat{s}_z$ the spin

part of the above particle-hole wave functions have to be decoupled into single-particle wave functions. This procedure is similar to the uncoupling of L and S and yields

$$|\left(\frac{1}{2},\frac{1}{2}\right)1\,0\rangle = \frac{1}{\sqrt{2}}\,|\,\frac{1}{2}\,\frac{1}{2}\rangle\,|\,\frac{1}{2}\,-\frac{1}{2}\rangle + \frac{1}{\sqrt{2}}\,|\,\frac{1}{2}\,-\frac{1}{2}\rangle\,|\,\frac{1}{2}\,\frac{1}{2}\rangle, \tag{F.14}$$

$$|\left(\frac{1}{2},\frac{1}{2}\right)0\,0\rangle = \frac{1}{\sqrt{2}}\,|\,\frac{1}{2}\,\frac{1}{2}\rangle\,|\,\frac{1}{2}\,-\frac{1}{2}\rangle - \frac{1}{\sqrt{2}}\,|\,\frac{1}{2}\,-\frac{1}{2}\rangle\,|\,\frac{1}{2}\,\frac{1}{2}\rangle, \tag{F.15}$$

$$|\left(\frac{1}{2},\frac{1}{2}\right)1\,1\rangle = |\,\frac{1}{2}\,\frac{1}{2}\rangle\,|\,\frac{1}{2}\,-\frac{1}{2}\rangle. \tag{F.16}$$

For a system of i particles it is

$$\hat{s}_z = \sum_i \hat{s}_z^{(i)}, \tag{F.17}$$

where $\hat{s}_z^{(i)}$ denotes the third component of the spin operator acting on particle i. Acting with $\hat{s}_z$ on the spin states of Eqs. (F.14) to (F.16) yields

$$\hat{s}_z\,|\left(\frac{1}{2},\frac{1}{2}\right)1\,0\rangle = 0, \tag{F.18}$$

$$\hat{s}_z\,|\left(\frac{1}{2},\frac{1}{2}\right)0\,0\rangle = 0, \tag{F.19}$$

$$\hat{s}_z\,|\left(\frac{1}{2},\frac{1}{2}\right)1\,1\rangle = |\left(\frac{1}{2},\frac{1}{2}\right)1\,1\rangle. \tag{F.20}$$

Combining these results with Eq. (F.8) and Eq. (F.13) gives

$$\langle 2^+_{\text{sph}}\,|\,\hat{T}^{\text{M1}}_0\,|\,2^+_{\text{sph}}\rangle = \frac{1}{3}\sqrt{\frac{3}{4\,\pi}}\,g_s^{\,\nu}\,\mu_N \approx -0.62\,\mu_N. \tag{F.21}$$

Finally, the B(M1) value can be estimated by combining this result with Eqs. (F.1), (F.4), and (F.6):

$$B(\text{M1}; 2^+_2 \to 2^+_1) = \frac{1}{5}\,|\,\langle 2^+_2\,|\,\hat{T}^{\text{M1}}\,|\,2^+_1\rangle\,|^2 \tag{F.22}$$

$$= \frac{1}{5}\,\alpha^2\,\beta^2\,\frac{15}{2}\left(\langle 2^+_{\text{d}}, 2\,|\,\hat{T}^{\text{M1}}_0\,|\,2^+_{\text{d}}, 2\rangle - \langle 2^+_{\text{sph}}, 2\,|\,\hat{T}^{\text{M1}}_0\,|\,2^+_{\text{sph}}, 2\rangle\right)^2 \tag{F.23}$$

$$= \frac{3}{2}\,\alpha^2\,\beta^2\left(\frac{5}{6} + 0.62\right)^2\,\mu_N^2 \tag{F.24}$$

$$\approx 0.08\,\mu_N^2. \tag{F.25}$$

Bibliography

[1] A. Bravais, *Abhandlung über die Systeme von regelmäßig auf einer Ebene oder im Raum vertheilten Punkten*. Ostwalds Klassiker der exakten Wissenschaften, Engelmann, 1897. originally published in french in J. Ecole Polytechn. 19 (1850) 1.

[2] S. Lie, *Theorie der Transforationsgruppen I*. Teubner, 1888.

[3] S. Lie, *Theorie der Transforationsgruppen II*. Teubner, 1890.

[4] S. Lie, *Theorie der Transforationsgruppen III*. Teubner, 1893.

[5] E. Noether, "Invariante Variationsprobleme.," *Nachr. Ges. Wiss. Göttingen, Math.-Phys. Kl.*, vol. 1918, pp. 235–257, 1918.

[6] I. W. Griffiths, "J. J. Thomson — the Centenary of His Discovery of the Electron and of His Invention of Mass Spectrometry," *Rapid communications in mass spectrometry*, vol. 11, no. 1, pp. 2–16, 1997.

[7] D. H. Geiger and E. Marsden, "LXI. The laws of deflexion of a particles through large angles," *Philosophical Magazine Series 6*, vol. 25, no. 148, pp. 604–623, 1913.

[8] R. A. Millikan, "The Isolation of an Ion, a Precision Measurement of its Charge, and the Correction of Stokes's Law," *Phys. Rev. (Series I)*, vol. 32, pp. 349–397, Apr 1911.

[9] R. A. Millikan., "On the Elementary Electrical Charge and the Avogadro Constant," *Phys. Rev.*, vol. 2, pp. 109–143, Aug 1913.

[10] J. Chadwick, "Possible Existence of a Neutron," *Nature*, vol. 129, pp. 312–312, Feb 1932.

[11] C. M. G. Lattes et al., "Processes Involving Charged Mesons," *Nature*, vol. 159, pp. 694–697, May 1947.

[12] L. W. Alvarez et al., "Neutral Cascade Hyperon Event," *Phys. Rev. Lett.*, vol. 2, pp. 215–219, Mar 1959.

[13] H. Georgi, *Lie Algebras in Particle Physics*, vol. 54 of *Frontiers in Physics*. Addison-Wesley, 1982.

[14] M. Gell-Mann, "A schematic model of baryons and mesons," *Physics Letters*, vol. 8, no. 3, pp. 214–215, 1964.

[15] S. Eidelman et al., "Review of Particle Physics," *Physics Letters B*, vol. 592, no. 1–4, pp. 1 – 5, 2004. Review of Particle Physics.

[16] K. Olive and P. D. Group, "Review of Particle Physics," *Chinese Physics C*, vol. 38, no. 9, p. 090001, 2014.

[17] M. Gell-Mann, *The eightfold way: a theory of strong interaction symmetry*. California Institute of Technology, Mar 1961.

[18] S. Okubo, "Note on unitary symmetry in strong interactions," *Progress of Theoretical Physics*, vol. 27, no. 5, pp. 949–966, 1962.

[19] S. Okubo, "Note on unitary symmetry in strong interaction. ii: Excited states of baryons," *Progress of Theoretical Physics*, vol. 28, no. 1, pp. 24–32, 1962.

[20] V. E. Barnes et al., "Observation of a Hyperon with Strangeness Minus Three," *Phys. Rev. Lett.*, vol. 12, pp. 204–206, Feb 1964.

[21] E. D. Bloom et al., "High-Energy Inelastic $e-p$ Scattering at 6° and 10°," *Phys. Rev. Lett.*, vol. 23, pp. 930–934, Oct 1969.

[22] M. Breidenbach et al., "Observed Behavior of Highly Inelastic Electron-Proton Scattering," *Phys. Rev. Lett.*, vol. 23, pp. 935–939, Oct 1969.

[23] E. Epelbaum, H.-W. Hammer, and U.-G. Meißner, "Modern theory of nuclear forces," *Rev. Mod. Phys.*, vol. 81, pp. 1773–1825, Dec 2009.

[24] N. Ishii, S. Aoki, and T. Hatsuda, "Nuclear Force from Lattice QCD," *Phys. Rev. Lett.*, vol. 99, p. 022001, Jul 2007.

[25] D. R. Entem and R. Machleidt, "Accurate charge-dependent nucleon-nucleon potential at fourth order of chiral perturbation theory," *Phys. Rev. C*, vol. 68, p. 041001, Oct 2003.

[26] V. G. J. Stoks, R. A. M. Klomp, C. P. F. Terheggen, and J. J. de Swart, "Construction of high-quality *NN* potential models," *Phys. Rev. C*, vol. 49, pp. 2950–2962, Jun 1994.

[27] R. B. Wiringa, V. G. J. Stoks, and R. Schiavilla, "Accurate nucleon-nucleon potential with charge-independence breaking," *Phys. Rev. C*, vol. 51, pp. 38–51, Jan 1995.

[28] R. Machleidt, "High-precision, charge-dependent Bonn nucleon-nucleon potential," *Phys. Rev. C*, vol. 63, p. 024001, Jan 2001.

[29] S. C. Pieper, K. Varga, and R. B. Wiringa, "Quantum monte carlo calculations of $a = 9, 10$ nuclei," *Phys. Rev. C*, vol. 66, p. 044310, Oct 2002.

[30] B. R. Barrett, P. Navrátil, and J. P. Vary, "Ab initio no core shell model," *Progress in Particle and Nuclear Physics*, vol. 69, pp. 131 – 181, 2013.

[31] R. Roth and P. Navrátil, "*Ab Initio* Study of ^{40}Ca with an Importance-Truncated No-Core Shell Model," *Phys. Rev. Lett.*, vol. 99, p. 092501, Aug 2007.

[32] K. Kowalski, D. J. Dean, M. Hjorth-Jensen, T. Papenbrock, and P. Piecuch, "Coupled Cluster Calculations of Ground and Excited States of Nuclei," *Phys. Rev. Lett.*, vol. 92, p. 132501, Apr 2004.

[33] S. D. Głazek and K. G. Wilson, "Renormalization of Hamiltonians," *Phys. Rev. D*, vol. 48, pp. 5863–5872, Dec 1993.

[34] F. Wegner, "Flow-equations for Hamiltonians," *Annalen der Physik*, vol. 506, no. 2, pp. 77–91, 1994.

[35] C. Bertulani and V. Ponomarev, "Microscopic studies on two-phonon giant resonances," *Physics Reports*, vol. 321, no. 4–5, pp. 139 – 251, 1999.

[36] A. E. L. Dieperink, O. Scholten, and F. Iachello, "Classical Limit of the Interacting-Boson Model," *Phys. Rev. Lett.*, vol. 44, pp. 1747–1750, Jun 1980.

[37] F. Iachello and A. Arima, *The Interacting Boson Model*. Oxford Library of the Physical Sciences, Oxford University Press, 1962.

[38] A. Arima and F. Iachello, "Collective Nuclear States as Representations of a SU(6) Group," *Phys. Rev. Lett.*, vol. 35, pp. 1069–1072, Oct 1975.

[39] Y. Blumenfeld, T. Nilsson, and P. V. Duppen, "Facilities and methods for radioactive ion beam production," *Physica Scripta*, vol. 2013, no. T152, p. 014023, 2013.

[40] C. Romig et al., "Direct determination of ground-state transition widths of low-lying dipole states in 140ce with the self-absorption technique," *Physics Letters B*, vol. 744, pp. 369 – 374, 2015.

[41] C. Walz et al., "Observation of the competitive double-gamma decay," *Nature*, vol. 526, pp. 406–409, October 2015.

[42] K. Sieja et al., "Shell model description of zirconium isotopes," *Phys. Rev. C*, vol. 79, p. 064310, Jun 2009.

[43] M. Böyükata, P. Van Isacker, and I. Uluer, "Description of nuclei in the A $\approx$ 100 mass region with the interacting boson model," *Journal of Physics G: Nuclear and Particle Physics*, vol. 37, no. 10, p. 105102, 2010.

[44] Y. Tsunoda et al., "Novel shape evolution in exotic Ni isotopes and configuration-dependent shell structure," *Phys. Rev. C*, vol. 89, p. 031301, Mar 2014.

[45] C. Kremer, *Systematische Untersuchung quadrupolkollektiver Kerne im Rahmen des Modells wechselwirkender Valenzbosonen*. BSc thesis, Technische Universität Darmstadt, 2010.

[46] R. Trippel, *Bereich unerwarteter $O(6)$-Symmetrie des Grundzustands im Parameterraum des Interacting Boson Models*. BSc thesis, Technische Universität Darmstadt, 2010.

[47] C. Kremer et al., "Linking partial and quasi dynamical symmetries in rotational nuclei," *Phys. Rev. C*, vol. 89, p. 041302, Apr 2014.

[48] C. Kremer et al., "Erratum: Linking partial and quasi dynamical symmetries in rotational nuclei [phys. rev. c **89** , 041302(r) (2014)]," *Phys. Rev. C*, vol. 92, p. 039902, Sep 2015.

[49] P. W. Anderson, "More is different - Broken symmetry and the nature of the hierarchical structure of science," *Science*, vol. 177, pp. 393–396, 1973.

[50] E. A. McCutchan, N. V. Zamfir, and R. F. Casten, "Mapping the interacting boson approximation symmetry triangle: New trajectories of structural evolution of rare-earth nuclei," *Phys. Rev. C*, vol. 69, p. 064306, Jun 2004.

[51] D. D. Warner and R. F. Casten, "Predictions of the interacting boson approximation in a consistent *q* framework," *Phys. Rev. C*, vol. 28, pp. 1798–1806, Oct 1983.

[52] P. Lipas, P. Toivonen, and D. Warner, "Iba consistent-Q formalism extended to the vibrational region," *Physics Letters B*, vol. 155, no. 5, pp. 295 – 298, 1985.

[53] Y. Alhassid and N. Whelan, "Chaotic properties of the interacting-boson model: A discovery of a new regular region," *Phys. Rev. Lett.*, vol. 67, pp. 816–819, Aug 1991.

[54] J. Jolie et al., "Experimental Confirmation of the Alhassid-Whelan Arc of Regularity," *Phys. Rev. Lett.*, vol. 93, p. 132501, Sep 2004.

[55] Y. Alhassid and A. Leviatan, "Partial dynamical symmetry," *Journal of Physics A: Mathematical and General*, vol. 25, no. 23, p. L1265, 1992.

[56] D. J. Rowe, "Quasidynamical Symmetry in an Interacting Boson Model Phase Transition," *Phys. Rev. Lett.*, vol. 93, p. 122502, Sep 2004.

[57] D. Bonatsos, E. A. McCutchan, and R. F. Casten, "SU(3) Quasidynamical Symmetry Underlying the Alhassid-Whelan Arc of Regularity," *Phys. Rev. Lett.*, vol. 104, p. 022502, Jan 2010.

[58] F. J. Dyson and M. L. Mehta, "Statistical Theory of the Energy Levels of Complex Systems. IV," *Journal of Mathematical Physics*, vol. 4, no. 5, pp. 701–712, 1963.

[59] T. A. Brody et al., "Random-matrix physics: spectrum and strength fluctuations," *Rev. Mod. Phys.*, vol. 53, pp. 385–479, Jul 1981.

[60] Y. Alhassid and R. D. Levine, "Transition-Strength Fluctuations and the Onset of Chaotic Motion," *Phys. Rev. Lett.*, vol. 57, pp. 2879–2882, Dec 1986.

[61] M. G. Mayer, "On Closed Shells in Nuclei. II," *Phys. Rev.*, vol. 75, pp. 1969–1970, Jun 1949.

[62] O. Haxel, J. H. D. Jensen, and H. E. Suess, "On the "Magic Numbers" in Nuclear Structure," *Phys. Rev.*, vol. 75, pp. 1766–1766, Jun 1949.

[63] K. L. Heyde, "The nuclear shell model," in *The Nuclear Shell Model*, pp. 58–154, Springer Berlin Heidelberg, 1994.

[64] J. Rainwater, "Nuclear Energy Level Argument for a Spheroidal Nuclear Model," *Phys. Rev.*, vol. 79, pp. 432–434, Aug 1950.

[65] A. Bohr, "On the Quantization of Angular Momenta in Heavy Nuclei," *Phys. Rev.*, vol. 81, pp. 134–138, Jan 1951.

[66] A. Arima and F. Iachello, "The Interacting Boson Model," *Annual Review of Nuclear and Particle Science*, vol. 31, no. 1, pp. 75–105, 1981.

[67] T. Otsuka, A. Arima, F. Iachello, and I. Talmi, "Shell model description of interacting bosons," *Physics Letters B*, vol. 76, no. 2, pp. 139 – 143, 1978.

[68] J. N. Ginocchio and M. W. Kirson, "Relationship between the Bohr Collective Hamiltonian and the Interacting-Boson Model," *Phys. Rev. Lett.*, vol. 44, pp. 1744–1747, Jun 1980.

[69] V. Werner, N. Pietralla, P. von Brentano, R. F. Casten, and R. V. Jolos, "Quadrupole shape invariants in the interacting boson model," *Phys. Rev. C*, vol. 61, p. 021301, Jan 2000.

[70] J. E. Humphreys, *Introduction to Lie algebras and representation theory*, vol. 9. Springer Science & Business Media, 1972.

[71] R. Casten, "Status of Experimental Tests of the IBA," in *Interacting Bose-Fermi Systems in Nuclei* (F. Iachello, ed.), vol. 10 of *Ettore Majorana International Science Series*, pp. 3–20, Springer US, 1981.

[72] J. Jolie, R. F. Casten, P. von Brentano, and V. Werner, "Quantum phase transition for γ-soft nuclei," *Phys. Rev. Lett.*, vol. 87, p. 162501, Oct 2001.

[73] S. Aslanidou, *Investigation of the O(6) character of ^{196}Pt and developement and construction of a cryogenic gastarget for (e, e'p) and (e, e'pp) experiments on ^{3}He*. Dissertation, Technische Universität Darmstadt, in preperation.

[74] J. Jolie et al., "Test of the SO(6) selection rule in ^{196}Pt using cold-neutron capture," *Nuclear Physics A*, vol. 934, pp. 1 – 7, 2015.

[75] G. Rainovski et al., "How close to the $O(6)$ symmetry is the nucleus ^{124}Xe?," *Physics Letters B*, vol. 683, no. 1, pp. 11 – 16, 2010.

[76] A. Leviatan, "Partial dynamical symmetries," *Progress in Particle and Nuclear Physics*, vol. 66, no. 1, pp. 93 – 143, 2011.

[77] A. Leviatan and I. Sinai, "Partial dynamical SU(3) symmetry and the nature of the lowest $K=0$ collective excitation in deformed nuclei," *Phys. Rev. C*, vol. 60, p. 061301, Oct 1999.

[78] R. F. Casten, R. B. Cakirli, K. Blaum, and A. Couture, "Evidence for Partial Dynamical Symmetries in Atomic Nuclei," *Phys. Rev. Lett.*, vol. 113, p. 112501, Sep 2014.

[79] A. Couture, R. F. Casten, and R. B. Cakirli, "Extended tests of an SU(3) partial dynamical symmetry," *Phys. Rev. C*, vol. 91, p. 014312, Jan 2015.

[80] A. Leviatan, A. Novoselsky, and I. Talmi, "O(5) symmetry in IBA-1 — the O(6)—U(5) transition region," *Physics Letters B*, vol. 172, no. 2, pp. 144 – 148, 1986.

[81] A. Leviatan and P. V. Isacker, "Generalized Partial Dynamical Symmetry in Nuclei," *Phys. Rev. Lett.*, vol. 89, p. 222501, Nov 2002.

[82] P. Rochford and D. Rowe, "The survival of rotor and SU(3) bands under strong spin-orbit symmetry mixing," *Physics Letters B*, vol. 210, no. 1, pp. 5 – 9, 1988.

[83] D. J. Rowe, P. Rochford, and J. Repka, "Dynamic structure and embedded representation in physics: The group theory of the adiabatic approximation," *Journal of Mathematical Physics*, vol. 29, no. 3, pp. 572–577, 1988.

[84] J. Ginocchio and M. Kirson, "An intrinsic state for the interacting boson model and its relationship to the Bohr-Mottelson model," *Nuclear Physics A*, vol. 350, no. 1–2, pp. 31 – 60, 1980.

[85] M. Macek and A. Leviatan, "First-order quantum phase transitions: Test ground for emergent chaoticity, regularity and persisting symmetries," *Annals of Physics*, vol. 351, pp. 302 – 362, 2014.

[86] A. Arima and F. Iachello, "Two-nucleon transfer reactions in the SU(6) boson model," *Phys. Rev. C*, vol. 16, pp. 2085–2089, Nov 1977.

[87] J. A. Cizewski et al., "Two-particle transfer in O(6) nuclei," *Physics Letters B*, vol. 88, no. 3, pp. 207 – 211, 1979.

[88] J. A. Cizewski et al., "Evidence for a New Symmetry in Nuclei: The Structure of ^{196}Pt and the O(6) Limit," *Phys. Rev. Lett.*, vol. 40, pp. 167–170, Jan 1978.

[89] P. Cejnar and J. Jolie, "Wave-function entropy and dynamical symmetry breaking in the interacting boson model," *Phys. Rev. E*, vol. 58, pp. 387–399, Jul 1998.

[90] P. Cejnar and J. Jolie, "Quantum phase transitions studied within the interacting boson model," *Phys. Rev. E*, vol. 61, pp. 6237–6247, Jun 2000.

[91] S. Heinze, P. Cejnar, J. Jolie, and M. Macek, "Evolution of spectral properties along the O(6)-U(5) transition in the interacting boson model. I. Level dynamics," *Phys. Rev. C*, vol. 73, p. 014306, Jan 2006.

[92] J. Proskurins, A. Andrejevs, T. Krasta, and J. Tambergs, "Studies of phase transitions and quantum chaos relationships in extended casten triangle of IBM-1," *Physics of Atomic Nuclei*, vol. 69, no. 7, pp. 1248–1253, 2006.

[93] P. Cejnar and J. Jolie, "Dynamical-symmetry content of transitional IBM-1 hamiltonians," *Physics Letters B*, vol. 420, no. 3–4, pp. 241 – 247, 1998.

[94] S. Heinze, *Eine Methode zur Lösung beliebiger bosonischer und fermionischer Vielteilchensysteme*. Dissertation, Universität zu Köln, 2008. Online available at `http://kups.ub.uni-koeln.de/2357/` (date of access: 16. April 2015).

[95] A. Leviatan, "Intrinsic and collective structure in the interacting boson model," *Annals of Physics*, vol. 179, no. 2, pp. 201 – 271, 1987.

[96] P. V. Isacker, "Partial and Quasi Dynamical Symmetries in Nuclei," *Nuclear Physics News*, vol. 24, no. 3, pp. 23–27, 2014.

[97] `http://www.nndc.bnl.gov/ensdf/`, "Evaluated Nuclear Structure Data Files," 2015 (accessed August 2, 2015).

[98] J. V. Maher, J. J. Kolata, and R. W. Miller, "(p,t) Population of 0^+ States in $Dy^{158,160,162}$ and $Er^{164,166}$," *Phys. Rev. C*, vol. 6, pp. 358–365, Jul 1972.

[99] D. G. Fleming et al., "Study of the (p,t) Reaction on the Even Gadolinium Nuclei," *Phys. Rev. C*, vol. 8, pp. 806–818, Aug 1973.

[100] A. de-Shalit and I. Talmi, *Nuclear shell theory*. Academic Press, 1969.

[101] W. Frank, P. von Brentano, A. Gelberg, and H. Harter, "Test of a projection method from the interacting boson model-2 to the interacting boson model-1," *Phys. Rev. C*, vol. 38, pp. 2358–2361, Nov 1988.

[102] F. Iachello, "Algebraic methods for molecular rotation-vibration spectra," *Chemical Physics Letters*, vol. 78, no. 3, pp. 581 – 585, 1981.

[103] R. Kanungo, "Shell closures in the N and $Z = 40-60$ region for neutron and proton-rich nuclei," *Physics Letters B*, vol. 649, no. 1, pp. 31 – 34, 2007.

[104] F. Tondeur, "The subshell closure at N = 56 and the deformation of neutron-rich isotopes from Ge to Zr," *Nuclear Physics A*, vol. 359, no. 2, pp. 278 – 288, 1981.

[105] E. Cheifetz et al., "Experimental Information Concerning Deformation of Neutron Rich Nuclei in the $A \sim 100$ Region," *Phys. Rev. Lett.*, vol. 25, pp. 38–43, Jul 1970.

[106] J. Stachel, P. Van Isacker, and K. Heyde, "Interpretation of the $A \approx 100$ transitional region in the framework of the interacting boson model," *Phys. Rev. C*, vol. 25, pp. 650–657, Jan 1982.

[107] H. Mach et al., "Deformation and shape coexistence of 0^+ states in ^{98}Sr and ^{100}Zr," *Physics Letters B*, vol. 230, no. 1–2, pp. 21 – 26, 1989.

[108] K. Heyde and J. Sau, "Symmetric and antisymmetric states: A general feature of two-component systems," *Phys. Rev. C*, vol. 33, pp. 1050–1061, Mar 1986.

[109] N. Pietralla, P. von Brentano, and A. Lisetskiy, "Experiments on multiphonon states with proton–neutron mixed symmetry in vibrational nuclei," *Progress in Particle and Nuclear Physics*, vol. 60, no. 1, pp. 225 – 282, 2008.

[110] C. Walz et al., "Origin of Low-Energy Quadrupole Collectivity in Vibrational Nuclei," *Phys. Rev. Lett.*, vol. 106, p. 062501, Feb 2011.

[111] W. D. Hamilton, A. Irbäck, and J. P. Elliott, "Mixed-Symmetry Interacting-Boson-Model States in the Nuclei ^{140}Ba, ^{142}Ce, and ^{144}Nd with $N = 84$," *Phys. Rev. Lett.*, vol. 53, pp. 2469–2472, Dec 1984.

[112] N. Pietralla et al., "Transition Rates between Mixed Symmetry States: First Measurement in ^{94}Mo," *Phys. Rev. Lett.*, vol. 83, pp. 1303–1306, Aug 1999.

[113] N. Pietralla et al., "Coulomb excitation of the 2^+_{ms} state of ^{96}Ru in inverse kinematics," *Phys. Rev. C*, vol. 64, p. 031301, Aug 2001.

[114] S. R. Lesher et al., "Low-spin structure of ^{96}Mo studied with the $(n, n'\gamma)$ reaction," *Phys. Rev. C*, vol. 75, p. 034318, Mar 2007.

[115] V. Werner et al., "Proton–neutron structure of the N=52 nucleus ^{92}Zr," *Physics Letters B*, vol. 550, no. 3–4, pp. 140 – 146, 2002.

[116] E. Elhami et al., "Anomalous behavior of the 2^+ mixed-symmetry state in ^{94}Zr," *Phys. Rev. C*, vol. 75, p. 011301, Jan 2007.

[117] H. Ohm et al., "Strong harmonic E3 vibrations in ^{96}Zr," *Physics Letters B*, vol. 241, no. 4, pp. 472 – 475, 1990.

[118] D. J. Horen et al., "Lifetime of the 3^-_1 state and octupole collectivity in ^{96}Zr," *Phys. Rev. C*, vol. 48, pp. R2131–R2134, Nov 1993.

[119] G. Molnár, S. W. Yates, and R. A. Meyer, "Evidence for a coexisting four-particle, four-hole band in doubly closed subshell ^{96}Zr," *Phys. Rev. C*, vol. 33, pp. 1843–1846, May 1986.

[120] H. Mach et al., "Intruder state collectivity at a double subshell closure from the beta decay of 0^- ^{96}Y^g to the levels of ^{96}Zr," *Phys. Rev. C*, vol. 37, pp. 254–264, Jan 1988.

[121] D. Hofer et al., "Direct and multiple excitations in ^{96}Zr from inelastic-scattering experiments," *Nuclear Physics A*, vol. 551, no. 2, pp. 173 – 209, 1993.

[122] R. F. Casten, *Nuclear Structure from a Simple Perspective*. Oxford: Oxford Science Publications, 1990. Second Edition 2005.

[123] D. Steppenbeck et al., "Evidence for a new nuclear 'magic number' from the level structure of ^{54}Ca," *Nature*, vol. 502, pp. 207–210, Oct 2013.

[124] D. Steppenbeck et al., "Low-Lying Structure of ^{50}Ar and the $N = 32$ Subshell Closure," *Phys. Rev. Lett.*, vol. 114, p. 252501, Jun 2015.

[125] D. H. Wilkinson and D. E. Alburger, "Beta Decay of Be^{11}," *Phys. Rev.*, vol. 113, pp. 563–571, Jan 1959.

[126] I. Talmi and I. Unna, "Order of Levels in the Shell Model and Spin of Be^{11}," *Phys. Rev. Lett.*, vol. 4, pp. 469–470, May 1960.

[127] T. Otsuka et al., "Magic Numbers in Exotic Nuclei and Spin-Isospin Properties of the *NN* Interaction," *Phys. Rev. Lett.*, vol. 87, p. 082502, Aug 2001.

[128] T. Otsuka et al., "Novel Features of Nuclear Forces and Shell Evolution in Exotic Nuclei," *Phys. Rev. Lett.*, vol. 104, p. 012501, Jan 2010.

[129] T. Otsuka, T. Suzuki, R. Fujimoto, H. Grawe, and Y. Akaishi, "Evolution of Nuclear Shells due to the Tensor Force," *Phys. Rev. Lett.*, vol. 95, p. 232502, Nov 2005.

[130] J. P. Schiffer et al., "Is the Nuclear Spin-Orbit Interaction Changing with Neutron Excess?," *Phys. Rev. Lett.*, vol. 92, p. 162501, Apr 2004.

[131] M. E. Peskin and D. V. Schroeder, *An introduction to quantum field theory*. Westview, 1995.

[132] H. Überall, *Electron Scattering From Complex Nuclei: Part B*. Academic Press Inc., 1972.

[133] H. Theissen, *Springer Tracts in Modern Physics*, vol. 65. Springer, 1972.

[134] W. C. Barber, "Inelastic Electron Scattering," *Annual Review of Nuclear Science*, vol. 12, no. 1, pp. 1–42, 1962.

[135] T. de Forest and J. Walecka, "Electron scattering and nuclear structure," *Advances in Physics*, vol. 15, no. 57, pp. 1–109, 1966.

[136] J. Heisenberg and H. P. Blok, "Inelastic Electron Scattering From Nuclei," *Annual Review of Nuclear and Particle Science*, vol. 33, no. 1, pp. 569–610, 1983.

[137] `http://www.nndc.bnl.gov/masses/`, "Atomic Mass Evaluation," (accessed September 2, 2015).

[138] A. Scheikh Obeid et al., "$E2$ strengths and transition radii difference of one-phonon 2^+ states of ^{92}Zr from electron scattering at low momentum transfer," *Phys. Rev. C*, vol. 87, p. 014337, Jan 2013.

[139] A. Scheikh Obeid et al., "$B(E2)$ strength ratio of one-phonon 2^+ states of ^{94}Zr from electron scattering at low momentum transfer," *Phys. Rev. C*, vol. 89, p. 037301, Mar 2014.

[140] V. Y. Ponomarev, "Private communication."

[141] A. J. F. Siegert, "Note on the Interaction Between Nuclei and Electromagnetic Radiation," *Phys. Rev.*, vol. 52, pp. 787–789, Oct 1937.

[142] A. Richter, "Operational Experience at the S-DALINAC," in *Proc. of the 5th EPAC* (S. Myers, A. Pacheco, R. Pascual, C. Petit-Jean-Genaz, and P. J., eds.), IOP Publishing, 1996.

[143] H.-D. Gräf, H. Miska, E. Spamer, O. Titze, and T. Walcher, "High resolution electron scattering facility at the Darmstadt linear accelerator (DALINAC): I. Accelerator," *Nuclear Instruments and Methods*, vol. 153, no. 1, pp. 9 – 15, 1978.

[144] Y. Poltoratska et al., "Status and recent developments at the polarized-electron injector of the superconducting Darmstadt electron linear accelerator S-DALINAC," *J. Phys.: Conf. Ser.*, vol. 298, May 2011.

[145] K. Sonnabend et al., "The Darmstadt High-Intensity Photon Setup (DHIPS) at the S-DALINAC," *Nuclear Instruments and Methods in Physics Research Section A: Accelerators, Spectrometers, Detectors and Associated Equipment*, vol. 640, no. 1, pp. 6 – 12, 2011.

[146] F. Hug, *Erhöhung der Energieschärfe des Elektronenstrahls am S-DALINAC durch nicht-isochrones Rezirkulieren*. Dissertation, Technische Universität Darmstadt, 2013. Online available at `http://tuprints.ulb.tu-darmstadt.de/3469/` (date of access: 06. August 2015).

[147] M. Arnold, "*Auslegung, Aufbau und Inbetriebnahme einer dritten Rezirkulation für den S-DALINAC*". Dissertation, Technische Universität Darmstadt, in preperation.

[148] K. Lindenberg, *Development and Construction of the Low-Energy Photon Tagger NEPTUN*. PhD thesis, Technische Universität Darmstadt, März 2008.

[149] D. Savran et al., "The low-energy photon tagger NEPTUN," *Nuclear Instruments and Methods in Physics Research Section A: Accelerators, Spectrometers, Detectors and Associated Equipment*, vol. 613, no. 2, pp. 232 – 239, 2010.

[150] M. Knirsch, *Konzeption, Aufbau und Erprobung eines hochauflösenden QCLAM-Elektronenspektrometers mit großem Raumwinkel und hoher Impulsakzeptanz am Elektronenbeschleuniger S-DALINAC*. Dissertation, Technische Universität Darmstadt, 1991.

[151] K.-D. Hummel, *Konzeption, Aufbau und Inbetriebnahme eines Vieldrahtdriftkammer-Detektorsystems für das QCLAM-Spektrometer am supraleitenden Darmstädter Elektronenbeschleuniger S-DALINAC*. Dissertation, Technische Universität Darmstadt, 1992.

[152] J. Horn, *Entwicklung und Integration eines schnellen Kontrollsystems für den S-DALINAC und Weiterentwicklung der Vieldrahtdriftkammern im QCLAM-Spektrometer*. Dissertation, Technische Universität Darmstadt, 1997.

[153] B. Reitz, *Weiterentwicklung des Detektorsystems am QCLAM-Spektrometer des S-DALINAC und Untersuchung der Reaktionen* $^{48}Ca(e,e')$ *und* $^{58}Ni(e,e')$ *unter* 180°. Dissertation, Technische Universität Darmstadt, 2000.

[154] A. Byelikov, *Neutrino-Nukleosynthese der seltenen Isotope ^{138}La und ^{180}Ta und Entwicklung eines Siliziumballs für exklusive Elektronenstreuexperimente am S-DALINAC*. Dissertation, Technische Universität Darmstadt, 2007.

[155] C. Walz, *The two-photon decay of the $^{11}/_{2}^{-}$ isomere of ^{137}Ba and the mixed-symmetry states of $^{92,94}Zr$ and ^{94}Mo*. Dissertation, Technische Universität Darmstadt, 2014.

[156] C. Lüttge, *Entwicklung und Aufbau eines Magnetsystems für Elektronenstreuung unter* 180° *und vollständige Bestimmung der magnetischen Dipol- und Quadrupolstärkeverteilung in ^{28}Si*. Dissertation, Technische Universität Darmstadt, 2000.

[157] Accelerator group, "Private communication." Institut für Kernphysik, Technische Universität Darmstadt.

[158] F. Hug et al., "Operational Findings and Upgrade Plans on the Superconducting Electron Accelerator S-DALINAC," in *Proceedings of 2011 Particle Accelerator Conference*, pp. 1999–2001, Juni 2012.

[159] A. W. Lenhardt et al., "A silicon microstrip detector in a magnetic spectrometer for high-resolution electron scattering experiments at the S-DALINAC," *Nuclear Instruments and Methods in Physics Research Section A: Accelerators, Spectrometers, Detectors and Associated Equipment*, vol. 562, no. 1, pp. 320 – 326, 2006.

[160] H. Ikegami, "Second Order Properties of Double Focusing Spectrometer with Nonuniform Magnetic Field," *Review of Scientific Instruments*, vol. 29, no. 11, pp. 943–948, 1958.

[161] T. Walcher, R. Frey, H.-D. Gräf, E. Spamer, and H. Theissen, "High resolution electron scattering facility at the Darmstadt linear accelerator (DALINAC): II. Beam transport system and spectrometer (energy-loss system)," *Nuclear Instruments and Methods*, vol. 153, no. 1, pp. 17 – 28, 1978.

[162] O. Burda, *Nature of Mixed-Symmetry 2^+ States in ^{94}Mo from High-Resolution Electron and Proton Scatterng and Line Shape of the First Excited $^{1}/_{2}^{+}$ State in ^{9}Be*. Dissertation, Technische Universität Darmstadt, 2008.

[163] S. Strauch, *Entwicklung eines interaktiven Auswerteprogramms für Elektronenstreumessungen*. Diplomarbeit, Technische Universität Darmstadt, 1993.

[164] B. L. Berman and S. C. Fultz, "Measurements of the giant dipole resonance with monoenergetic photons," *Rev. Mod. Phys.*, vol. 47, pp. 713–761, Jul 1975.

[165] I. Poltoratska et al., "Fine structure of the isovector giant dipole resonance in ^{208}Pb: Characteristic scales and level densities," *Phys. Rev. C*, vol. 89, p. 054322, May 2014.

[166] Y.-S. Tsai, "Radiative Corrections to Electron-Proton Scattering," *Phys. Rev.*, vol. 122, pp. 1898–1907, Jun 1961.

[167] H. Crannell, "Elastic and Inelastic Electron Scattering from C^{12} and O^{16}," *Phys. Rev.*, vol. 148, pp. 1107–1118, Aug 1966.

[168] H. Breuer, "Note on electron scattering and the ionization correction," *Nuclear Instruments and Methods*, vol. 33, no. 2, pp. 226 – 228, 1965.

[169] L. W. Mo and Y. S. Tsai, "Radiative Corrections to Elastic and Inelastic ep and up Scattering," *Rev. Mod. Phys.*, vol. 41, pp. 205–235, Jan 1969.

[170] R. Sternheimer, M. Berger, and S. Seltzer, "Density effect for the ionization loss of charged particles in various substances," *Atomic Data and Nuclear Data Tables*, vol. 30, no. 2, pp. 261 – 271, 1984.

[171] R. M. Sternheimer, S. M. Seltzer, and M. J. Berger, "Density effect for the ionization loss of charged particles in various substances," *Phys. Rev. B*, vol. 26, pp. 6067–6076, Dec 1982.

[172] R. M. Sternheimer, S. M. Seltzer, and M. J. Berger, "Erratum: Density effect for the ionization loss of charged particles in various substances," *Phys. Rev. B*, vol. 27, pp. 6971–6971, Jun 1983.

[173] H. Mach et al., "Strong octupole and dipole collectivity in ^{96}Zr: Indication for octupole instability in the $A = 100$ mass region," *Phys. Rev. C*, vol. 42, pp. R811–R814, Sep 1990.

[174] R. Barlow, "Asymmetric Statistical Errors." `http://arxiv.org/pdf/physics/0406120v1.pdf`. Accessed: 2015-09-15.

[175] T. Belgya et al., "Doppler-shift lifetime measurements in ^{96}Zr with the inelastic neutron scattering reaction," *Nuclear Physics A*, vol. 500, no. 1, pp. 77 – 89, 1989.

[176] G. Molnár et al., "Particle-hole and vibrational states in doubly closed subshell ^{96}Zr from in-beam inelastic neutron and proton scattering," *Nuclear Physics A*, vol. 500, no. 1, pp. 43 – 76, 1989.

[177] K. Heyde, E. D. Kirchuk, and P. Federman, "Coexistence or strong-mixing of intruder 0^+ states in even-even Zr nuclei," *Phys. Rev. C*, vol. 38, pp. 984–992, Aug 1988.

[178] T. Otsuka, "Private communication."

[179] M. Honma et al., "New effective interaction for f_5pg_9-shell nuclei," *Phys. Rev. C*, vol. 80, p. 064323, Dec 2009.

[180] M. Honma et al., "Shell model fits for Sn isotopes," in *RIKEN Accelerator Progress Report 45, 35 (2011)*, p. 35, 2011. SNBG3 is a variant of SNBG1.

[181] Y. Utsuno et al., "Shape transitions in exotic Si and S isotopes and tensor-force-driven Jahn-Teller effect," *Phys. Rev. C*, vol. 86, p. 051301, Nov 2012.

[182] D. M. Brink and G. R. Satchler, *Angular Momentum*. Cambridge Monographs on Mathematical Physics, Cambridge University Press, 1987.

[183] P. Van Isacker, "Private communication."

[184] R. Shankar, *Principles of Quantum Mechanics*. Springer, 1994. Second Edition.

[185] P. J. Mohr, D. B. Newell, and B. N. Taylor, "Codata recommended values of the fundamental physical constants: 2014," 2015 (accessed December 2, 2015).

List of Figures

List of Tables

Acknowledgments

This work would not have been possible without the help and encouragement of some outstanding people. I would like to use this opportunity to thank them.

- Zuerst möchte ich meinen Eltern, **Karl-Heinz** und **Petra Kremer**, danken. Während meines Studiums und während meiner Tätigkeit als wissenschaftlicher Mitarbeiter konnte ich mich stets auf ihre Unterstützung und ihren Rat verlassen.
- Besonderer Dank gilt auch meiner Freundin **Uta Greis**. Mit großem Verständnis hat Sie mich durch diese Zeit begleitet und meine Stimmungsschwankungen ertragen.
- I would like to thank **Prof. Dr. Dr. h.c. Norbert Pietralla** for making this work possible. His continuous support and guidance during these years were highly appreciated. He always took the time to discuss with me and answer my questions. His passion for nuclear physics is contagious and motivating.
- Another important source of new ideas was **Prof. Dr. Peter von Neumann-Cosel** and I would like to thank him for many useful discussions and his guidance.
- For their invaluable support during the preparation of the σ fluctuation publication I thank **Prof. Ami Leviatan**, **Prof. Piet van Isacker**, and **Associate Prof. Georgi Rainovski**.
- I wish to than **Prof. Dr. Takaharu Otsuka**, **Dr. Tomoaki Togashi**, and **Dr. Yusuke Tsunoda** for sharing their shell-model calculations.
- I wish to thank **Dr. Vladimir Ponomarev** and **Dr. Volker Werner** for many enlightening discussions.
- During my work I was fortunate to share my office with highly intelligent and motivated people. I would like to thank **Dr. Christopher Walz**, **Dr. Christian Stahl**, **Michael Reese**, **Robert Stegmann**, and **Gerhart Steinhilber** for many insightful discussions and the good working atmosphere.
- I would also like to thank all the people from the **spectrometer group** and the **accelerator group**. Especially I would like to thank **Dr. Andreas Krugmann** and **Simela Aslanidou** for their help during the experiment and many fruitful discussions about data analysis.
- For proofreading my thesis and providing me with regular feedback, criticism, and suggestions I thank **Simela Aslanidou**, **Andreas Köhler**, **Dr. Andreas Krugmann**, **Dr. Volker Werner**, and **Markus Zweidinger**.
- Finally I would like to thank the **German Research Foundation** (Deutsche Forschungsgemeinschaft) for their financial support of my work through CRC 634.

Christoph Kremer

Lebenslauf

Mathildenstr. 45
64287 Darmstadt
015155897110
ckremer@ikp.tu-darmstadt.de

Persönliche Daten

Geschlecht	männlich
Geburtstag	20. Mai 1987
Geburtsort	Fulda
Nationalität	Deutsch
Familienstand	ledig
Eltern	Karl-Heinz und Petra Kremer (geb. Heil)

Lebens- und Bildungsgang

07.2011 bis 01.2016 **Dissertation in Kernphysik**, *Technische Universität Darmstadt, Institut für Kernphysik*, Note: ausstehend.
Thesis: Linking partial to quasi dynamical symmetries in rotational nuclei and shell evolution in ^{96}Zr

04.2012 bis 03.2015 **MBA General Management**, *Europäische Fernhochschule Hamburg*, Note: 1,6.
Thesis: Jahresabschlussanalyse und Unternehmensbewertung der Kromi Logistik AG

10.2010 bis 07.2011 **Master of Advanced Studies in Physik**, *University of Cambridge*, Note: merit.
Thesis: Random walk on complex networks.

04.2010 bis 09.2010 **Master of Science in Physik**, *Technische Universität Darmstadt*.
Der Studiengang wurde wegen eines Universitätswechsels abgebrochen.

10.2007 bis 02.2010 **Bachelor of Science in Physik**, *Technische Universität Darmstadt*, Note: 1,4.
Thesis: Systematische Untersuchung quadrupolkollektiver Kerne im Rahmen des Modells wechselwirkender Valenzbosonen.

2006-2007 **Schwerstbehindertenbetreuung**, *Malteser Hilfsdienst gGmbH Fulda*.

09.1997 bis 07.2006 **Abitur**, *Winfriedschule Fulda*, Gymnasium, Note: 2,4.
Leistungsfächer: Physik und Mathematik

Erklärung zur Dissertation

Hiermit versichere ich, die vorliegende Dissertation ohne Hilfe Dritter nur mit den angegebenen Quellen und Hilfsmitteln angefertigt zu haben. Alle Stellen, die aus Quellen entnommen wurden, sind als solche kenntlich gemacht. Diese Arbeit hat in gleicher oder ähnlicher Form noch keiner Prüfungsbehörde vorgelegen.

Darmstadt, den 15.12.2015

(Christoph Kremer)